MESOSCALE EDDY ACTIVITY IN THE SOUTH PACIFIC SUBTROPICAL COUNTER-CURRENT: DECADAL VARIABILITY AND BIO-PHYSICAL CONNECTIONS

A DISSERTATION SUBMITTED TO THE
GRADUATE DIVISION OF THE
UNIVERSITY OF HAWAI‘I AT MĀNOA
IN PARTIAL FULFILLMENT OF THE
REQUIREMENTS FOR THE DEGREE OF

DOCTOR OF PHILOSOPHY

IN

OCEANOGRAPHY

MAY 2020

By

Seth Travis

Dissertation Committee:

Bo Qiu, Chairperson
Niklas Schneider
Margaret McManus
Brian Powell
Bruce Howe

ACKNOWLEDGMENTS

The process of completing this dissertation was challenging, and I am extremely grateful for all of that I've learned and experienced over these six years, as well as the support that I have received from so many people. I find it important to acknowledge all the support that I have received, as I would not be able to complete this process without it.

First off, I would like to thank my advisor, Bo Qiu. He has been a pleasure to work with. Bo provided me with space to explore ideas of my own, and guidance on how to realize the projects generated from those ideas. I appreciate the trust that Bo had in me as I worked to coalesce all that I was learning into a more comprehensive understanding of ocean dynamics. I am also grateful for the opportunities that he provided me with, allowing me to attend research conferences and workshops, nominating me for awards and fellowships, and generally putting me in a strong position to learn and grow as a young scientist. Bo has been kind and thoughtful advisor, and I am very grateful to have had the opportunity to work with him.

I would also like to acknowledge all of my committee members - Niklas Schneider, Margaret McManus, Brian Powell, and Bruce Howe. They have been generous with their time, prompt with their feedback, and have helped to make my work better. I thank you all for your help, your ideas, and your support.

I am thankful for the support through all the years from the oceanography department, particularly the ocean office staff. They have done nothing but make me feel welcome and supported since I first arrived in 2013. This process would not be possible without their efforts, and I am thankful for everything that they have done.

I am extremely grateful for all of the friendships and family that I have made over the years. By its nature, graduate school is a transient place, but the connections and relationships that I built were so crucial to my time here. I believe that these relationships will remain strong, even as we all move onto the next phase as we pursue our own paths in our scientific careers. My friendships with my office mates, Assaf Azouri and Sherry Chou, are very special to me. As my first office mate, I built a much appreciated friendship with Assaf when I first moved here, and he provided me with great advice as I began to navigate being a PhD student. Sherry was a source of endless conversations, distracting us from the work that we both knew we should be doing. Still, these converstations were interesting, fun, and ridiculous, and I never knew what topics would come up.

My cohort of students was also very supportive, and I feel lucky to have been able to build the friendships that I did with them. All of times going to the beach, exploring the island, or just commiserating during lunch about the struggles we faced - these were all valued. I thank Sara Coffey for her friendship, at UH and beyond. It is wonderful to have someone with her energy and enthusiasm in my life. I never expected to learn AquaZumba routines, but because of Sara, I can say that I have. I would also like to thank Astrid Leitner. From her infectious energy to her curious nature, I have enjoyed building a friendship with her, and am glad to have had her to help push me through the program. I appreciate all of our scientific discussions and exploration of ideas together, even though our work was as different as could be, as well as adventures beyond the campus. I am grateful to be her friend.

The relationship that I have built with Emma Nuss is most precious to me. Over the last six years, we have slowly built our relationship from friendship to partnership. Emma has been so many things to me. She is someone that lets me process thoughts out loud, and explore new ideas, no matter how obscure or ridiculous. She is my favorite person to while away endless hours together with, whether we are finding something new to do, being silly, or just enjoying each other's company. I have loved getting to know her, learning about her life, and now, building one with her. Her kindness, thoughtfulness, and quirkiness are wonderfully endearing. I am humbled by the love we share, and I am forever grateful to have

been able to build this relationship with her.

My friends and family back home have been so supportive, and knowing that I can rely upon them all these years has been a comfort. I have to thank Rachel for her friendship for more years than I care to count, and for being there every single time I come home, when we pick back up right where we left off. Steve, Tim, and Mike have provided me with endless questions about what I'm doing, challenging me to ensure I actually knew what I was talking about, whether they were doing this intentionally or not. I am thankful for the adventures that we've been able to share, and the constancy of their friendship. I am grateful for having the chance to be a part of my brother's family, and watching the life that Adam, Natalie, and Landon have built together grows over the years.

Lastly, I want to thank my parents, Robin and Les, for their unwavering support and love over all these years. No matter what ridiculous choice I make for myself in life, they have always been there to support me. I appreciate the times that they've been able to come visit me, and all the times that I came back home to feel like I never left. I am thankful for their guidance over my whole life, their encouragement to explore the things that interest and excitement me, and the freedom they gave me to follow my path, wherever it may go. They provided me with everything I needed to make my life what I want it to be, and I cannot understate the gratitude and the love that I feel for them.

My time in Hawai‘i has been filled with countless others, each having their own impact on my life. My PhD work may be complete, but my memories of my time here will stay with me forever. I am grateful for all that I gained and learned, and only hope that I am able to give back even a fraction of what I have been lucky enough to be a part of.

Funding and Data Sources

The author acknowledges funding support from NASA grant NNX17AH33G and NASA grant NNX13AD91G.

The author acknowledges funding support from the Denise B. Evans fellowship, the ARCS Foundation, the J. Watumull Scholarship, and the University of Hawai‘i Graduate Student

Organization.

The Argo data used in this study were collected and made freely available by the International Argo Program and the national programs that contribute to it. The Argo data was accessed via https://www.usgodae.org/argo/argo.html

The author also acknowledges the European Centre for Mid-range Weather Forecasts (ECMWF) for providing the ORAS4 and ORAS5 ocean reanalysis data.

GlobColour data (http://globcolour.info) used in this study has been developed, validated, and distributed by ACRI-ST, France.

The altimeter products were produced by Ssalto/Duacs and distributed by Aviso+, with support from Cnes (https://www.aviso.altimetry.fr/duacs/

QuikScat data are produced by Remote Sensing Systems and sponsored by the NASA Ocean Vector Winds Science Team. Data are available at www.remss.com.

The gridded, daily data product of QuikSCAT V3 wind stress is provided by Ifremer. These data were obtained from the Centre de Recherche et d'Exploitation Satellitaire (CERSAT), at IFREMER, Plouzané (France).

ABSTRACT

Mesoscale eddies are important contributors to ocean circulation, and are ubiquitous throughout the world's oceans. They are capable of transporting heat, salinity, nutrients, and phytoplankton, and are important in the transfer of energy between different scales. In the South Pacific the Subtropical Counter-current is a region of heightened eddy activity which has been little studied. The South Pacific Subtropical Counter-current (STCC) is an eastward flowing current which overlays the westward South Equatorial Current (SEC). This vertically sheared STCC-SEC system is subject to baroclinic instabilities, which gives rise to mesoscale eddies.

Decadal variability of eddy activity in the western, subtropical South Pacific is examined using the past two decades of satellite altimetry data. By using ocean reanalysis data, low-frequency variations in the state of the ocean in this region are investigated. It is found that the low-frequency changes in shear and stratification simultaneously work to modulate the strength of baroclinic instabilities. These changes in the strength of the instabilities consequently affect the observed eddy activity. Using a linearization of the baroclinic growth rate, the contribution to the variability from the changes in shearing is found to be roughly twice as large as those from changes in stratification. Additionally, changes in the temperature and salinity fields are both found to have significant impacts on the low-frequency variability of shearing and stratification, for which salinity changes are responsible for 50-75% of the variability as caused by temperature changes. However, the changes in all these parameters do not occur concurrently, and can alternately work to negate or augment each other.

By furthering the investigation of this system to look at the driving mechanisms leading to changes in the shear and stratification, larger drivers of overall eddy activity can be identified. The Estimating the Circulation and Climate of the Ocean, phase II (ECCO2) ocean state model is used to perform budget analyses to identify to most important mechanisms altering the temperature and salinity fields in the STCC, and subsequently, the shear and

stratification. These budgets can then be related back to the linearized baroclinic growth rate to look at the impact of individual drivers on eddy activity. Variability in advective flux convergence is found to be the most consequential driver, for both shear and stratification, while direct atmospheric surface forcing through net heat flux and moisture fluxes are of approximately equal importance. Atmospheric forcings are additionally found to be related to the Interdecadal Pacific Oscillation through changes in the location and strength of the South Pacific Convergence Zone.

Mesoscale eddies have been shown to have significant effects on biogeochemical cycles, as observed in local levels of near-surface chlorophyll. In the South Pacific Subtropical Counter-current, however, an inconsistent chlorophyll anomaly response and a low correlation to the presence of eddies challenges simple explanation of the mechanisms at play. Using Glob-Colour ocean color data and Aviso altimetry data, an investigation of the area found that a seasonal reversal occurs in the character of the chlorophyll anomaly within eddies (reversal from positive to negative, and vice versa). The cause of this reversal is inferred to be a seasonally-changing limiting factor within the region. Argo float profiles co-located inside and outside of eddies are used to show the coincidence of chlorophyll anomalies with seasonally changing mixed layer depths and the ability of the eddies to access deep nutrient pools. Observations of other mechanisms, such as eddy stirring or eddy-Ekman pumping, are found to be seasonally less important than the mixed layer depth change induced nutrient flux. Additionally, metrics are developed to globally identify oceanic regions in which such seasonal reversals in chlorophyll anomalies could occur.

TABLE OF CONTENTS

LIST OF TABLES

LIST OF FIGURES

CHAPTER 1
INTRODUCTION

1.1 Motivation

Mesoscale eddy activity is a major component of kinetic energy in the ocean and the energy cycle of the eddies is important to understanding ocean dynamics. With scales of 10-100s of kilometers, mesoscale eddies lie at the transition between the large and the small. At the large scale, such as ocean gyre circulation, mean ocean patterns and gradients are set-up, and provide the background state for the generation of eddies. At the smaller scale, the transition to the submesoscale finds motions in which geostrophic assumptions are increasingly questionable. As such, mesoscale eddies, which lie between these scales, are an important component in understanding energy pathways in the ocean, and an understanding of the mechanisms which impact eddy activity is crucial.

Mesoscale eddies can impact and alter the ocean in a variety of ways. Eddies are important pathways for the transport of salt and heat (Chaigneau et al. 2011; Melnichenko et al. 2017; Qiu and Chen 2005; Zhang et al. 2014). Eddies have also been shown to alter the spatial and temporal evolution patterns of mixed layers (Gaube et al. 2019). More recently, interest has grown in the impact of eddies on biological and geochemical parameters, and the cycling of these. Near-surface chlorophyll anomalies can be identified within eddies, and provide the opportunity for biological hot spots (Gaube et al. 2013; McGillicuddy 2016). Globally, the many ways in which these mechanisms manifest is just beginning to be known.

In the South Pacific, the Subtropical Counter-current (STCC) is a region of heightened eddy activity, and lies in a highly complex region of the ocean. The source of the eddy activity in this region is not associated with any sort of boundary current or other strong, horizontally sheared currents. Circulation patterns are controlled by gyre circulation and meridional density gradients to create a highly sheared upper ocean. There is also a large number of tall seamounts provide random localized flow disturbances, while the Kermadec ridge, which

stretches from New Zealand to New Caledonia, significantly alters deep circulation patterns. The eddying region of the STCC also stretches from more productive waters closer to coastal regions, and spans into the highly oligotrophic South Pacific gyre, which has some of the lowest surface chlorophyll concentrations in the world. Additionally, eddy variability in the South Pacific has been much less studied when compared to other regions in the oceans, such as the North Pacific.

The eddy kinetic energy signal, as calculated from geostrophic surface velocity anomalies, has been shown to exhibit a clear annual cycle, as well as variations on longer time scales ($>$ 1 year period oscillations). Previous work (Qiu and Chen 2004; Qiu et al. 2008) explored baroclinic instability as a possible source of the eddy activity in the region. The goal of this dissertation is to analyze this eddy activity from a number of perspectives: variations through seasonal to decadal time scales, the dynamical causes of this variation, and the implications of this eddy activity as seen in its influences on biomass. The increase in hydrographic measurements in the region over the last two decades allow us to identify the dominant factors affecting the strength of this possible instability, and to examine likely forcings on the region which could affect these factors.

1.2 Structure of Dissertation

This dissertation is broken up into a number of chapters to highlight major themes and foci of analysis. Beyond this introductory section (Chapter 1), the body of the dissertation consists of three main chapters (Chapters 2-4), as well as a concluding section (Chapter 5). Each of the three main chapters will be presented as a full study, and will present independent perspectives of different aspects of mesoscale eddy activity in the South Pacific Subtropical Counter-current (STCC), and as such, each can be read independently. Any relevant appendices or supplementary materials will be provided at the end of the dissertation. Additionally, much of the relevant background literature is common among the chapters, and a bibliography for all the material is provided at the end of the dissertation.

Chapter 2 begins the analysis of decadal variability of mesoscale eddy activity in the

STCC. A combination of observational data and ocean state reanalysis model data is used to investigate the variability. It is hypothesized that the low-frequency variability in the strength of eddy activity is connected to variations in the strength of baroclinic instabilities. By using an idealized, theoretical model formulation, variability in the strength of baroclinic instabilities is investigated in relation to two key parameters: vertical zonal velocity shear and vertical stratification. These results are then used to attribute the relative importance of each of these parameters to observed eddy variability. Lastly, changes in these parameters are connected to changes in temperature and salinity fields in the STCC region.

In Chapter 3, the framework established in Chapter 2 is expanded to look at the dynamical links to larger scale, regional ocean variability. The same theoretical model framework is used to explore the driving factors of mesoscale eddy variability in the STCC. In Chapter 3, this analysis is taken a step further, and investigates the driving forces which alter the state of the ocean, and in turn, alter the strength of baroclinic instability in the STCC. Chapter 3 applies temperature and salinity budgets to data from a dynamically and thermodynamically consistent ocean state model to understand the influence of various drivers of ocean variability, such as net heat flux, freshwater fluxes, wind-driven circulation, and advective and diffusive fluxes.

Chapter 4 steps back from looking at eddy variability directly, and will instead focus on one of the impacts of eddies. Specifically, the impact of eddies on near-surface chlorophyll will be investigated. The STCC region is in a highly oligotrophic part of the South Pacific gyre, and as such, it is expected that the observed near-surface chlorophyll anomalies associated with eddies would be consistent with such a region, in which deep mixed layers in anticyclones are able to access a deeper nutrient pool, leading to increased productivity, and positive chlorophyll anomalies. However, prior work found a weakly correlated signal, in contrast to other regions of the global oceans with similar characteristics. This work will investigate why the eddy-chlorophyll patterns differ by looking at spatial and seasonal variability across the STCC band. By using an eddy-centric approach, in which individual eddies are identified and tracked, chlorophyll anomalies associated with these eddies can be measured.

CHAPTER 2
DECADAL VARIABILITY IN THE SOUTH PACIFIC SUBTROPICAL COUNTERCURRENT AND REGIONAL MESOSCALE EDDY ACTIVITY

This work also appears as: Travis, S. and B. Qiu, 2017: Decadal Variability in the South Pacific Subtropical Countercurrent and Regional Mesoscale Eddy Activity. J. Phys. Oceanogr., 47, 499–512, https://doi.org/10.1175/JPO-D-16-0217.1

Abstract

Decadal variability of eddy activity in the western, subtropical South Pacific is examined using the past two decades of satellite altimetry data. Between 21°S-29°S, there is a band of heightened eddy activity. In this region, the eastward South Pacific Subtropical Countercurrent (STCC) overlays the westward South Equatorial Current (SEC). This vertically sheared STCC-SEC system is subject to baroclinic instabilities. By using the European Centre for Medium Weather Forecasts (ECMWF) ocean reanalysis data (ORAS4) and verified by gridded Argo float data, low-frequency variations in the state of the ocean in this region are investigated. It is found that the low-frequency changes in the shearing and stratification of the STCC-SEC region simultaneously work to modulate the strength of baroclinic instabilities, as measured through the baroclinic growth rate. These changes in the strength of the instabilities consequently affect the observed eddy activity. Using a linearization of the baroclinic growth rate, the contribution to the variability from the changes in shearing is found to be roughly twice as large as those from changes in stratification. Additionally, changes in the temperature and salinity fields are both found to have significant impacts on the low-frequency variability of shearing and stratification, for which salinity changes are responsible for 50-75% of the variability as caused by temperature changes. However, the changes in all these parameters do not occur concurrently, and can alternately work to negate or augment each other.

2.1 Introduction

The South Pacific Subtropical Countercurrent (STCC) is an eastward moving current, manifesting as a band starting to the north of New Zealand and extending into the open South Pacific. First identified as the "South Tropical Countercurrent" (Merle et al. 1969), additional studies have also attributed the flow in this region as a shallow component of the northern edge of the eastward subtropical gyre circulation (e.g., Wyrtki 1975; Tsuchiya 1982). This broadly shallow current, hereafter referred to as the STCC, manifests from a vertical spreading of isopycnals, creating a reversal of the westward shearing of the South Equatorial Current (SEC) at depth to an eastward shearing in the upper ocean (Reid 1986; De Szoeke R. A. 1987; Qu and Lindstrom 2002). While the current is relatively weak as compared to other currents in the region, such as the East Australia Current, it is nonetheless a region of heightened eddy activity, as seen in the red box in Fig. 2.1a. Previous studies have explored the source of the heightened eddy activity found in the region as being caused by baroclinic instabilities (Qiu and Chen 2004).

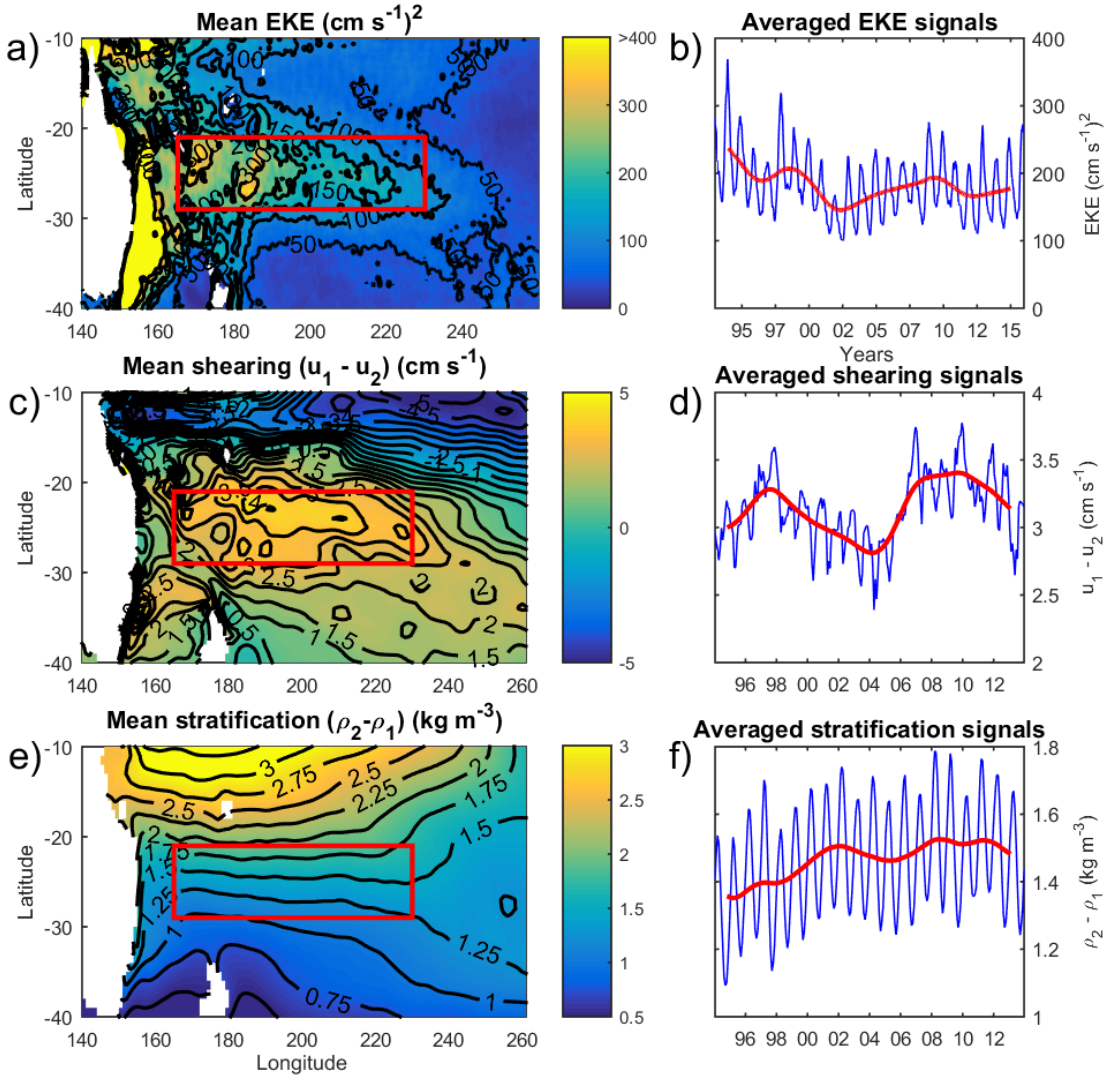

Figure 2.1: Left column: Mean state of the South Pacific. The STCC region is outlined by the red box. Right column: Area-averaged signals of the STCC region. The low-pass signal ($<$1 yr^{-1}) is given in the solid red line. Top: EKE cm^2 s^{-2}. Middle: Shearing (cm s^{-1}). Bottom: Stratification (kg m^{-3})

Qiu and Chen explored the seasonal variation of the eddy kinetic energy (EKE) in this region. They found that variations in the strength of baroclinic instabilities, as calculated through the baroclinic growth rate, were the most likely cause for the seasonality of the EKE, and emphasized the seasonal change in the zonal shearing between the STCC and the

SEC as the primary factor of the seasonal variability in baroclinic growth rates. Perhaps unsurprisingly, variations in the observed EKE patterns likely depend strongly upon the state of the STCC and the SEC. Qiu and Chen (2006) and Roemmich et al. (2007) observed a decadal spin-up of the South Pacific Subtropical Gyre, and attributed the spin-up to an increased wind stress curl over the larger ocean basin during the 1990's. More recently, Zhang and Qu (2015) found that the gyre spin-up has continued through the study period to 2013, causing an increase in SEC transport by 20%-30%. This spin-up has a number of possible consequences for the STCC-SEC region. In addition to the changes in shearing caused by increased transport, the redistribution of water characteristics could affect the stratification in the region. For example, Schneider et al. (2007) found that the spin-up of the gyre freshens and cools the eastern South Pacific, while also showing a significant warming trend in the western South Pacific. Additionally, Sasaki et al. (2008) found that the basin-scale spin-up causes changes in the eddy activity in the Tasman front, focusing on the area just to the southwest of the STCC-SEC region. These broad patterns affecting South Pacific Subtropical Gyre circulation could manifest in the STCC-SEC region, altering the state of the ocean, and leading to enhanced eddy activity.

An increasingly long record of observations in the region allows us to improve our understanding of the basic state of the STCC-SEC region and the slow, decadal variability from this mean state. This paper works to expand upon those previous findings by providing a detailed description of the basic state of the ocean which promotes eddy activity, then proceeds to describe longer term, decadal variations in the EKE signal, and within the STCC-SEC itself (see Fig. 2.1). Following the work by Qiu and Chen (2004), using an idealized model of the region as a 2 1/2-layer, baroclinic system, the strength of the instabilities can be simply parameterized. Variations in the strength of the instabilities should cause similar variations in the strength of the eddies, as measured through eddy kinetic energy (EKE). The variability of shearing and stratification in the region can be measured, and used to calculate fluctuations in the strength of baroclinic instabilities, as given through the baroclinic growth rate. Additionally, efforts are made to quantify the

amount of variation which can be attributed to the shearing and stratification parameters, and the relative influence on these of temperature versus salinity signals.

2.2 Data sets

The AVISO merged satellite, 1/4° x 1/4° gridded, daily-mean product is a source of more than 20 years of data for sea surface height (Ducet et al. 2000). Covering the time frame from 1993 to present, this data set can be used to examine a number of oceanographic features. Apart from measuring changes in the absolute sea surface height, sea surface height anomalies can also be used to calculate anomalous geostrophic velocities, and in turn quantify the EKE in the STCC region.

Depth profiles of horizontal velocities, temperature, and salinity data from the European Centre for Medium-Range Weather Forecasts (ECMWF) Ocean Reanalysis (ORAS4) are used (Balmaseda et al. 2013). The data product provides a 1° x 1° gridded, monthly mean data product, running from 1957 to present. This provides a data record which covers the entirety of the AVISO satellite altimetry data set, and our subsequent EKE calculations. For verification of the product, additional data is taken from Argo profiling floats, using the MOAA-GPV data set, as compiled by Hosoda et al. (2008). The MOAA-GPV data product provides a 1° x 1° gridded, monthly mean data product of profiles of temperature and salinity. These profiles extend down to 2000 m depth. By assuming a thermal wind balance, these profiles can be used to calculate the vertical shearing of the horizontal ocean currents. Argo floats have provided observational subsurface information since 2001. Starting in 2004, there begins to be sufficient Argo float coverage in the South Pacific for relatively good measurements of the ocean state and it's variability. This data will be used for comparison against the ECMWF ORAS4 data. It should be noted that as the ORAS4 utilizes Argo data in its reanalysis, it is not a fully independent data set, and as such, the comparison between the data sets cannot be used to fully corroborate the findings before 2004.

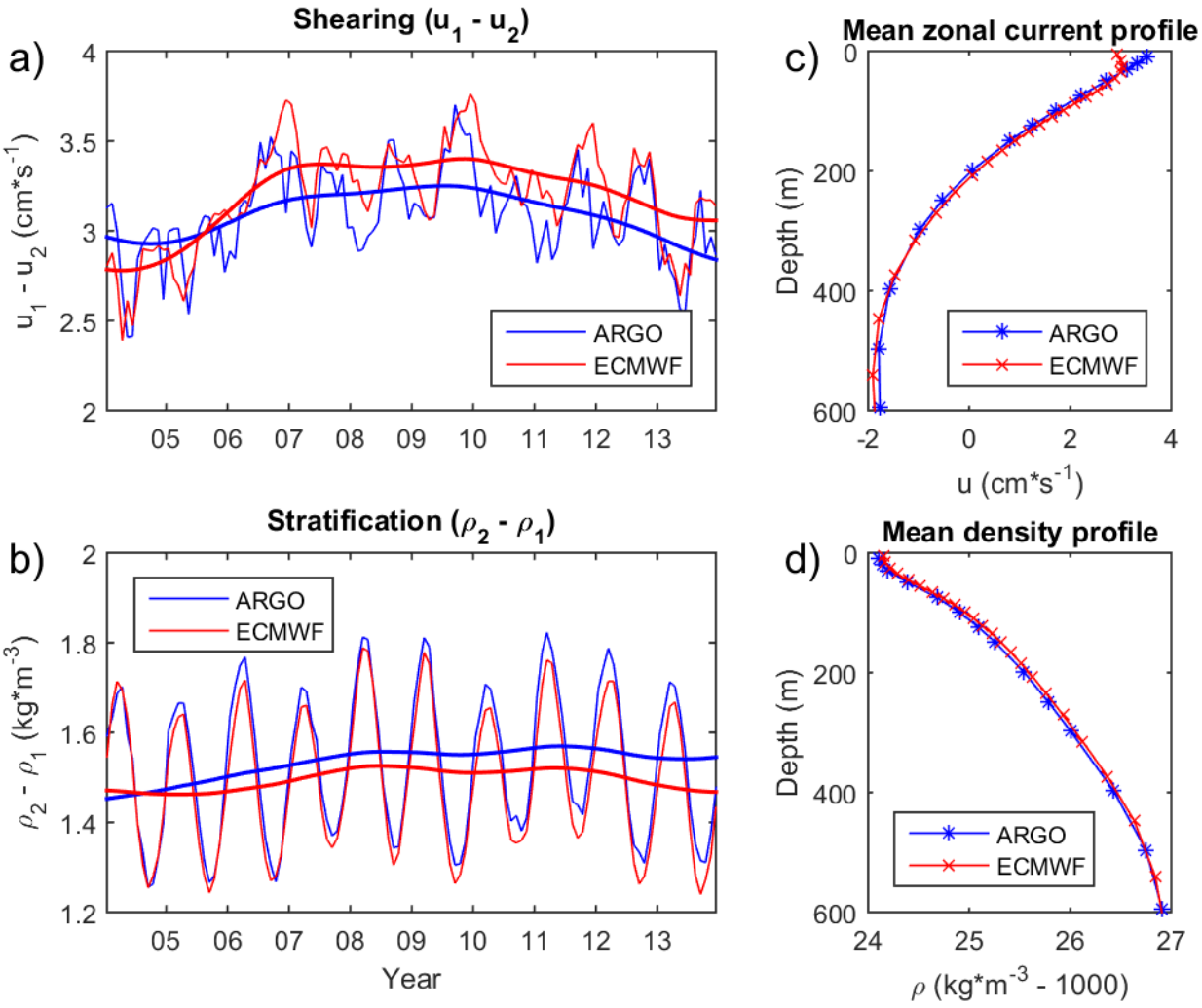

Figure 2.2: Time series of (a) the averaged shearing and (b) stratification in the Argo and ECMWF data sets. Averaged vertical profiles of (c) zonal current and (d) density.

As shown in Fig. 2.2, the averaged signal of shearing is very similar in the Argo and ECMWF data sets. This is also true of the averaged stratification signal. Here, u_1 and u_2 are defined as the depth-averaged zonal velocity of the upper 200 m of the ocean and between 200-600 m, respectively. Likewise, ρ_1 and ρ_2 are the depth-averaged density of each layer. The area-averaged time signal is able to capture the low frequency (<1 yr^{-1}) variability, as well as a large amount of the seasonal variability. Generally, the Argo data shows a slightly less sheared and a slightly more stratified system. Both of these factors would contribute to make the system less baroclinically unstable in the Argo data. In addition to the time variability signals, the vertical profiles are also very similar. The only level at which there is any discrepancy of note is at the very surface of the profile of zonal current. In these profiles, the surface zonal currents in the Argo profile continue to strengthen the eastward flow, whereas the ECMWF profile actually has a slightly more westward flow. This difference can be understood from the lack of Ekman flows in the Argo-based calculations, resulting in a slight overestimation of the near-surface zonal velocity in the Argo time series.

Figure 2.3 shows the low-pass filtered, meridionally averaged variability in the two data sets. As in the time series and vertical profiles, there is high agreement between the two data sets. In both the shearing and stratification, the Argo and ECMWF data exhibit the same patterns of highs and lows, with only minor variations in exact location and timing. The largest discrepancies between the two data sets come from the magnitude of some of the changes. Generally, data from ECMWF has larger anomalies than that of the Argo data. However, overall there is strong agreement between the data series, which gives confidence that the ECMWF data is capturing the dynamics of the region, and that this data can be used to extend the data record over the full period spanning the AVISO altimetry data record.

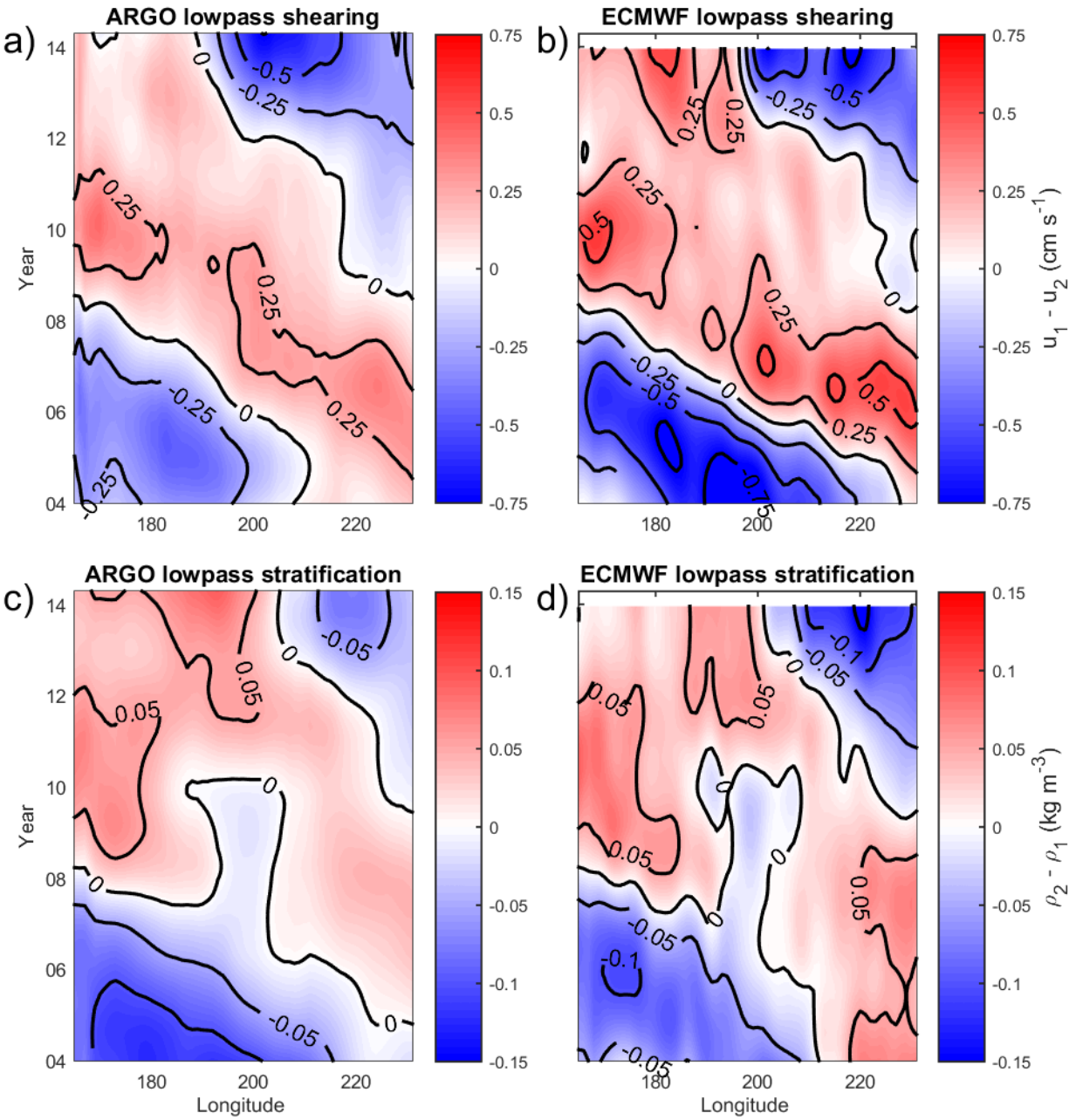

Figure 2.3: Meridionally-averaged low-pass bands of shearing and stratification in the Argo and ECMWF data sets. (a) Argo shearing. (b) ECWMF shearing. (c) Argo stratification (d) ECMWF stratification

2.3 Observations

The analyses are confined to the band of 165°E-130°W, 21°S-29°S, as indicated by the red boxes in each of the maps in Fig. 2.1. This is the band of the highest eddy activity, and is where the STCC and SEC have the strongest interactions. To explore changes in the region, satellite altimetry data will be used to look at eddy activity, while ECMWF ORAS4 data is used to examine depth profiles of velocity, density, temperature, and salinity.

2.3.1 EKE Observations

Satellite data reveals the elevated eddy activity across the STCC region. The STCC region has an annual EKE cycle which averages +60/-50 cm^2 s^{-2}. The region has a mean EKE greater than 150 cm^2 s^{-2} across most of the region, with the western region exceeding a mean level of 200 cm^2 s^{-2}. (Fig. 2.1a,b) Among this band, there are particularly active regions near 170° E, and 182°-187°E. These correspond to the sea mount ridges of the Norfolk Ridge for the western band, and the Kermadec Ridge and Colville Ridge which surround the Lau basin, for the eastern band. In these sites, the mean EKE can exceed 350 cm^2 s^{-2}.

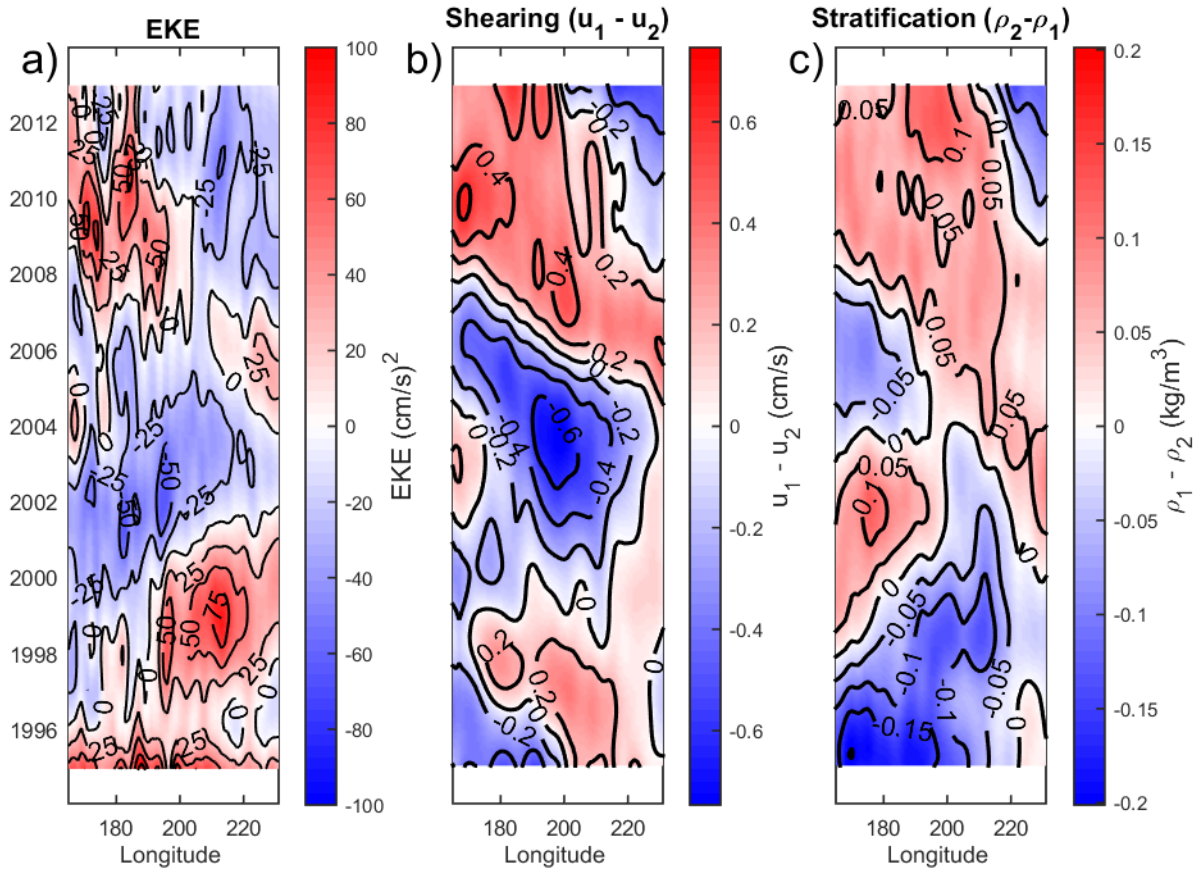

Figure 2.4: Meridionally-averaged bands of low-pass (<1 yr^{-1}) variation in the STCC. (a) EKE (cm^2 s^{-2}). (b) Shear (cm s^{-1}). (c) Stratification (kg m^{-3}).

For analysis, meridionally averaged bands of properties in the STCC-SEC region are used to look at the spatial and temporal patterns. These properties are EKE, shearing, stratification, temperature, and salinity. It is found that for the low-pass filtered signal (< 1 yr^{-1}), the meridionally averaged signal shows high correlation with the signal at any point, and is representative of the whole band. The low-pass filtered EKE values vary by nearly ± 75 cm^2 s^{-2}, which is comparable in magnitude to the seasonal variability (Fig. 2.4a). The patterns show significant spatial variability. A rough description of the variability would first break the region into an eastern and western half (east/west of 195°E). In these patterns, the east experiences higher EKE from 1993-2001 and a short period between 2005-2008. In the west, there is a short high-EKE period from 1993-1997 and from 2007-2012. It is these

long-term patterns that are hypothesized to be caused by changes in the strength of the baroclinic instabilities. The spatial-temporal patterns of long term changes in the baroclinic growth rate will need to exhibit similar patterns in order to verify the hypothesis that these variations are the primary driver of changes in eddy activity.

2.3.2 Shearing

To first approximate the vertically-sheared STCC-SEC system, a 2 1/2-layer model is utilized. The model is setup with a light, eastward-flowing top layer, a heavy, deeper, westward-flowing layer, and a quiescent bottom layer. The depth of the upper layer is chosen as 200 m. This is the mean depth of flow reversal, from which the currents switch from being eastward to westward with increasing depth. For the lower layer, a mean depth of 600 m (400 m layer thickness) is chosen, as this is the depth at which the mean shear changes from positive (eastward) to negative (westward). As a test, ventilated thermocline theory (Luyten et al. 1983) is used to calculate the respective layer depths for a similarly layered ocean. Using reference layer densities of $\rho_1 = 1024.75$ kg m^{-3}, $\rho_2 = 1026.4$ kg m^{-3}, $\rho_3 = 1027.25$ kg m^{-3}, and the mean wind stress curl field across the South Pacific, the layer thickness averaged in the STCC region is found to be 200-250 m for the upper layer and approximately 400 m for the lower layer. This corresponds quite well to our initial approximation of the two layer thicknesses. Within each of the layers, the density and velocity is taken as the depth-averaged value of the respective parameter.

Now using our representation of the STCC-SEC region, the shearing of the 2 1/2-layer system can be represented by the velocity difference between the two layers. This is the same representation of the shearing as used in section 2, where the shearing is defined as U_1-U_2, and U_1 and U_2 are the depth-averaged zonal velocity of each respective layer. The shearing experienced in the region depends upon the relative strengths of the STCC and the SEC, which manifests as the underlying current below the STCC, and is a component of the wind-driven South Pacific gyre circulation. For the mean state, the strongest shearing occurs to the north, exceeding 3.5 cm s^{-1} for much of the area. In the southern regions, the

mean shearing is between 2.5-3.5 cm s^{-1} (Fig. 2.1c,d).

As shown in Fig. 2.4b, the low-pass filtered shearing signal varies in excess of $\pm$ 0.5 cm s^{-1} for much of the region. This range, being greater than 1.0 cm s^{-1} in strength, is on the same order of magnitude as the seasonal cycle. Roughly speaking, the eastern half of the region experiences highs from 1993-1999 and 2006-2012, while the western half experiences a relatively minor high from 1998-2004, and a stronger high from 2008-2014.

2.3.3 Stratification

Just as with the shearing in the STCC-SEC region, the stratification can be simply described as the density difference between the two layers. This is given by ρ_2-ρ_1, where ρ_1 and ρ_2 are the depth-averaged densities of the respective layers. The mean density difference between the two layers is 1.5 kg m^{-3}, exceeding 1.8 kg m^{-3} to the north, and as low as 1 kg m^{-3} to the south. (Fig. 2.1e,f) There is a very strong seasonal cycle in the stratification. The majority of this seasonal cycle can be accounted for through the warming and cooling of the upper waters as the seasons change. This seasonal cycle has a range of 0.4-0.5 kg m^{-3}.

Low-frequency variation has mostly led to an increased level of stratification over the last 22 years (see Fig. 2.4c). This is accounted for primarily through the lightening of the upper waters. The average stratification has increased by roughly 0.15 kg m^{-3} over this time period, equaling 30% of the seasonal variation, and greater than a 10% increase of the mean state. The fluctuations in stratification can exceed $\pm$0.1 kg m^{-3} over the whole time range. The majority of this variability occurs, again, in the upper layer. While there is some slight variability in the deeper layer, it has maximum departures from the mean state of 0.05 kg m^{-3}, roughly a third of the total change. To understand the primary drivers of the changes in the stratification, looking at changes in the upper layer will provide the greatest insight.

2.3.4 Change in the state of the STCC

By focusing our analysis on the changing state of the upper layer, through temperature and salinity fluctuations, we are able to discover more about the driving forces in the region.

Stratification variability is directly explored through the changing of the upper layer density, using a linearized state equation for density of $\rho = \rho_0 - \alpha_T(T - T_0) + \beta_S(S - S_0)$, where T and S are the depth averaged temperature and salinity of the upper layer, α_T and β_S are thermal expansion and haline contraction coefficients, respectively, and ρ_0 is the mean density of the upper layer. Shear variability is explored, using a similar state equation while also applying a thermal wind balance and integrating through the layer. In this case, the upper layer zonal velocity is given by $U = U_0 + \frac{gH_1}{\rho_0 f}\Big(- \alpha_T \frac{\partial(T-T_0)}{\partial y} + \beta_S \frac{\partial(S-S_0)}{\partial y}\Big)$, where U_0 is the mean zonal velocity of the upper layer, and H_1 is the layer thickness of the upper layer.

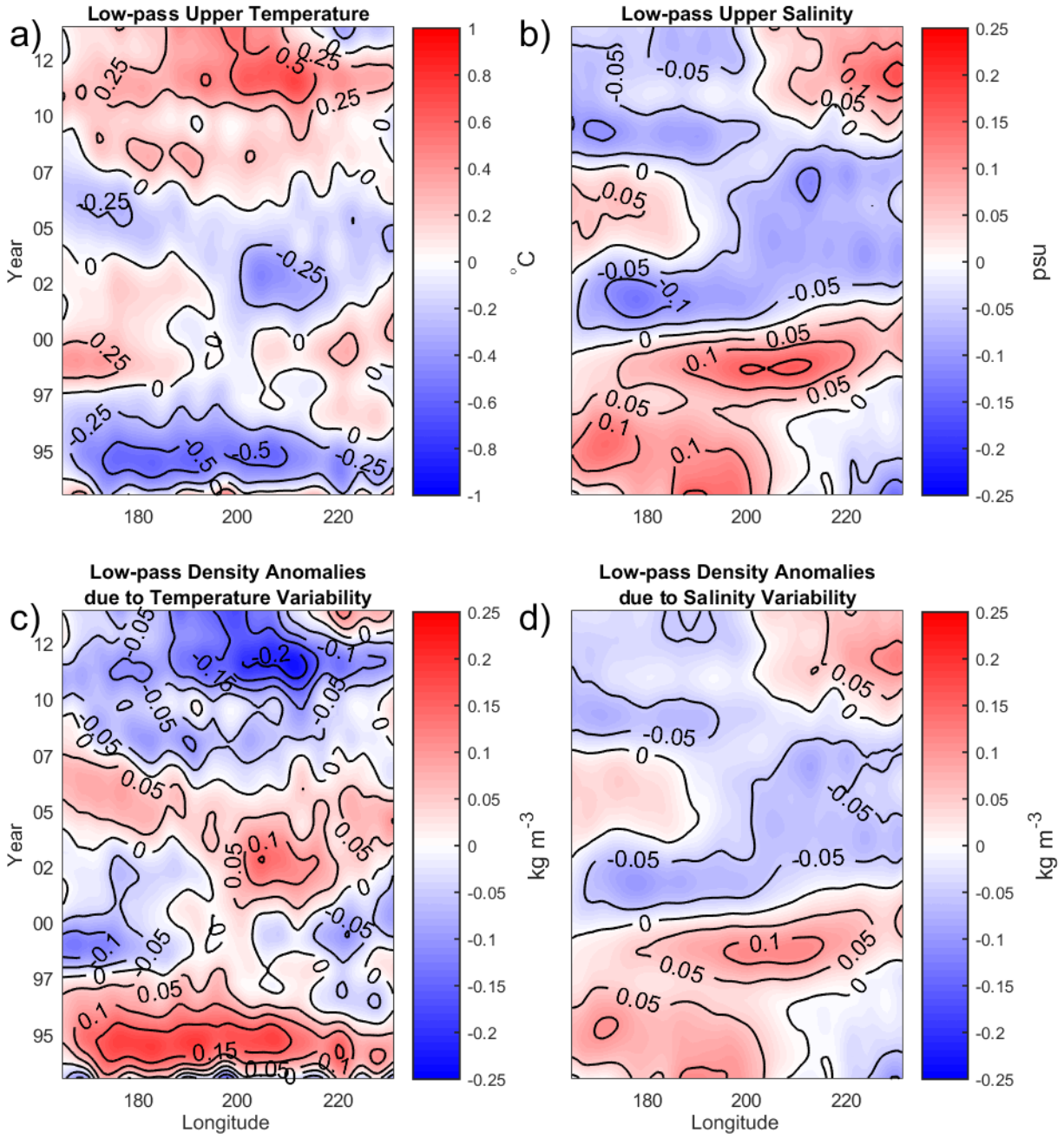

Figure 2.5: The upper row has meridionally-averaged bands of salinity and temperature variations. The lower row has meridionally-averaged bands of density anomalies, caused by varying salinity and temperature variations. (a) Low-pass salinity (psu). (b) Low-pass temperature (°C). (c) Low-pass density with varying salinity and fixed temperature (kg m^{-3}). (d) Low-pass density with varying temperature and fixed salinity (kg m^{-3}).

Temperature fluctuations are the dominant factor in the seasonality of density fluctuations. When holding salinity constant, temperature fluctuations can cause a change of 0.5 kg m^{-3} in the upper layer of the ocean. The low-frequency change in temperature shows a region-wide warming (Fig. 2.5a). From 1993 to 2013, there is roughly a 0.5° C increase in the upper layer temperature, which is more than double the rate of the globally average sea surface temperature rise of 0.11°C per decade for the upper 75 m, (IPCC 2013). This high warming causes a decrease in layer density by 0.2-0.3 kg m^{-3}, as can be seen in the Fig. 2.5c. Density changes caused by temperature variability in the upper layer is highly correlated, at a correlation of 0.83, to changes in the total layer density variability.

Figure 2.6a shows the anomalous meridional temperature gradients, with the resultant zonal velocity anomalies caused by the density gradients shown in Fig. 2.6c. The zonal velocity anomalies can exceed ± 0.5 cm s^{-1}, and is approximately equal in magnitude to the changes in the shearing in the STCC-SEC region. There is a high correlation of 0.84 between the shearing and the temperature-induced zonal velocity anomalies.

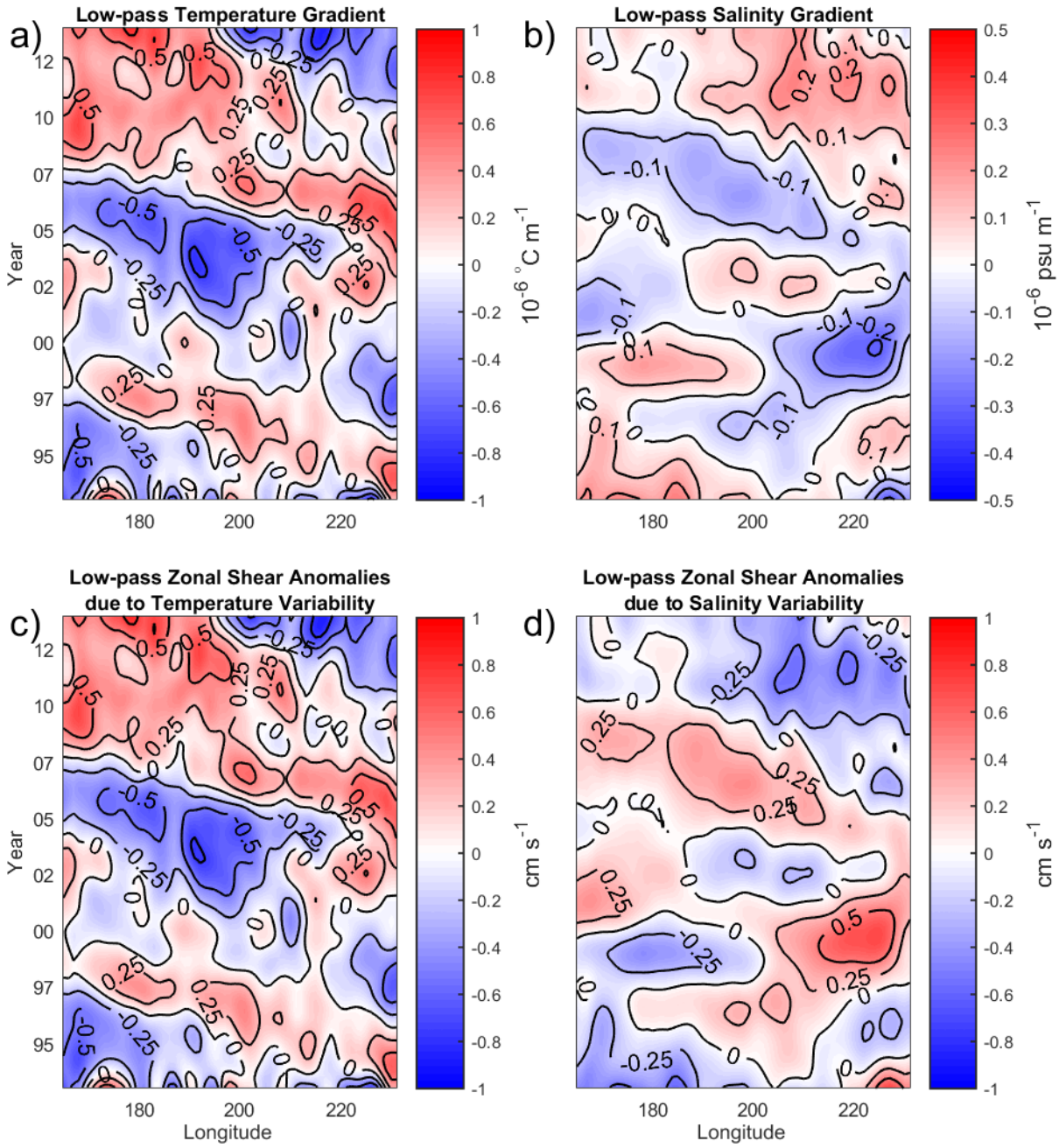

Figure 2.6: The upper row has meridionally-averaged bands of variations in the meridional gradient of salinity and temperature. The lower row has meridionally-averaged bands of the meridional density gradient anomalies, caused by varying salinity and temperature variations. (a) Low-pass salinity gradient (psu m^{-1}). (b) Low-pass temperature gradient (°C m^{-1}). (c) Low-pass velocity anomalies derived from varying salinity and fixed temperature (cm s^{-1}). (d) Low-pass velocity anomalies with varying temperature and fixed salinity (cm s^{-1}).

Seasonal salinity fluctuations are negligible when compared to the temperature fluctuations. Seasonal fluctuations of only 0.02 psu are responsible for a 0.01 kg m^{-3} change in density, which is only 2% of that caused by temperature fluctuations. This minute fluctuation can largely be ignored. The low-frequency salinity fluctuations are significant, however. The salinity varies by as much as 0.25 psu over the time period, as seen in Fig. 2.5b. This results in density anomalies up to as much as 0.15 kg m^{-3}, shown in Fig. 2.5d. While this is comparably smaller than the fluctuations caused by temperature, it is roughly of 50-75% of those temperature-caused density anomalies, and is not negligible. When compared to the variations in the upper layer density, there is a modest correlation with the salinity-induced density variability of 0.69.

The zonal velocity changes caused salinity variability is smaller. The changing salinity field results in velocity changes of ± 0.25 cm s^{-1}, with some patchy areas which can exceed ± 0.5 cm s^{-1} (Fig. 2.6d). This is about 50% of the velocity changes caused by temperature variability, and has a very low correlation of 0.04. The salinity-induced zonal velocity changes are nearly entirely out of phase with those of the more dominant temperature-induced changes.

There is previous work which has looked at changes in the salinity patterns across the South Pacific. Zhang and Qu (2014) explored a freshening of South Pacific Tropical Water (SPTW), which has a salinity maximum to the northeast of the STCC-SEC region of high eddy activity. They found a poleward shift of the salinity maximum, with sea surface salinities (SSS) along the northern section of the formation region being advected by the SEC. They also note a strong correlation of SSS to the Pacific Decadal Oscillation. Schneider et al. (2007) examined changes in the salinity fields due to the spin-up of the South Pacific gyre, in which the increased circulation brings colder, fresher, sub-Antarctic waters further north.

From these results, it can be said that temperature fluctuations are the major driver of variability in the state of the STCC-SEC region. Changes in the shearing and stratification induced by temperature variability are generally about twice as large as those caused by

salinity variability. However, the salinity variability is not negligible. Changes induced by salinity variability largely work to modulate those of temperature variability, and negate some of the largest temperature-induced fluctuations. In rare cases, the two parameters can work in phase with each other, and cause some of the greatest variability in shear and stratification. An example of this can be seen in the shear signal the middle of the STCC-SEC region, between 2002 and 2005 (see Fig. 2.6c, Fig. 2.6d, and Fig. 2.4b). Both the temperature and salinity variability cause negative zonal velocity anomalies, albeit of different magnitudes, and together create the weakest shearing across the STCC-SEC region over the time record.

2.4 Baroclinic instability growth rates

If the eddy activity in the region is the result of baroclinic instabilities, then calculating and analyzing shifts in how unstable the system is should correspond well to the shifts in the eddy activity. In understanding the baroclinic instability growth rate, the instability criterion given below tells us that the shearing of the layers must exceed the baroclinic Rossby wave speed plus a scaled advection by the lower layer. The criterion can be derived by following the same process as Qiu (1999):

$$U_1 - U_2 > \frac{(\rho_2 - \rho_1) g H_2}{\rho_1 f_0^2} \beta + \gamma_2 U_2 \tag{2.1}$$

where $\gamma_2 = \frac{\rho_2 - \rho_1}{\rho_3 - \rho_2}$, $[\rho_1, \rho_2, \rho_3]$ = the density of their respective layers, g = the gravitational constant, H_2 = the mean lower layer thickness, f_0 = the Coriolis parameter at a reference latitude (in this case 25°S), and $\beta = \frac{df}{dy}$ = the beta-parameter at the reference latitude. For derivations, see Eq. 16 in Qiu (1999).

From Eq. 2.1, we can tell that the shearing and the stratification are important parameters. Measuring the strength of baroclinic instabilities is done by calculating the peak baroclinic instability growth rate. As the degree of instability is a nonlinear process, it is expected that proportional changes in shearing or stratification do not necessarily result in

proportional changes in the baroclinic growth rate. In Fig. 2.7a, the baroclinic growth rate for a range of shearing and stratification scenarios is shown, where the red box indicates the average seasonal range of shearing and stratification for all areas in the STCC-SEC region, while the green line indicates the area-averaged seasonal cycle. As shearing increases, so does the baroclinic growth rate. Conversely, decreasing stratification leads to an increase in the baroclinic growth rates.

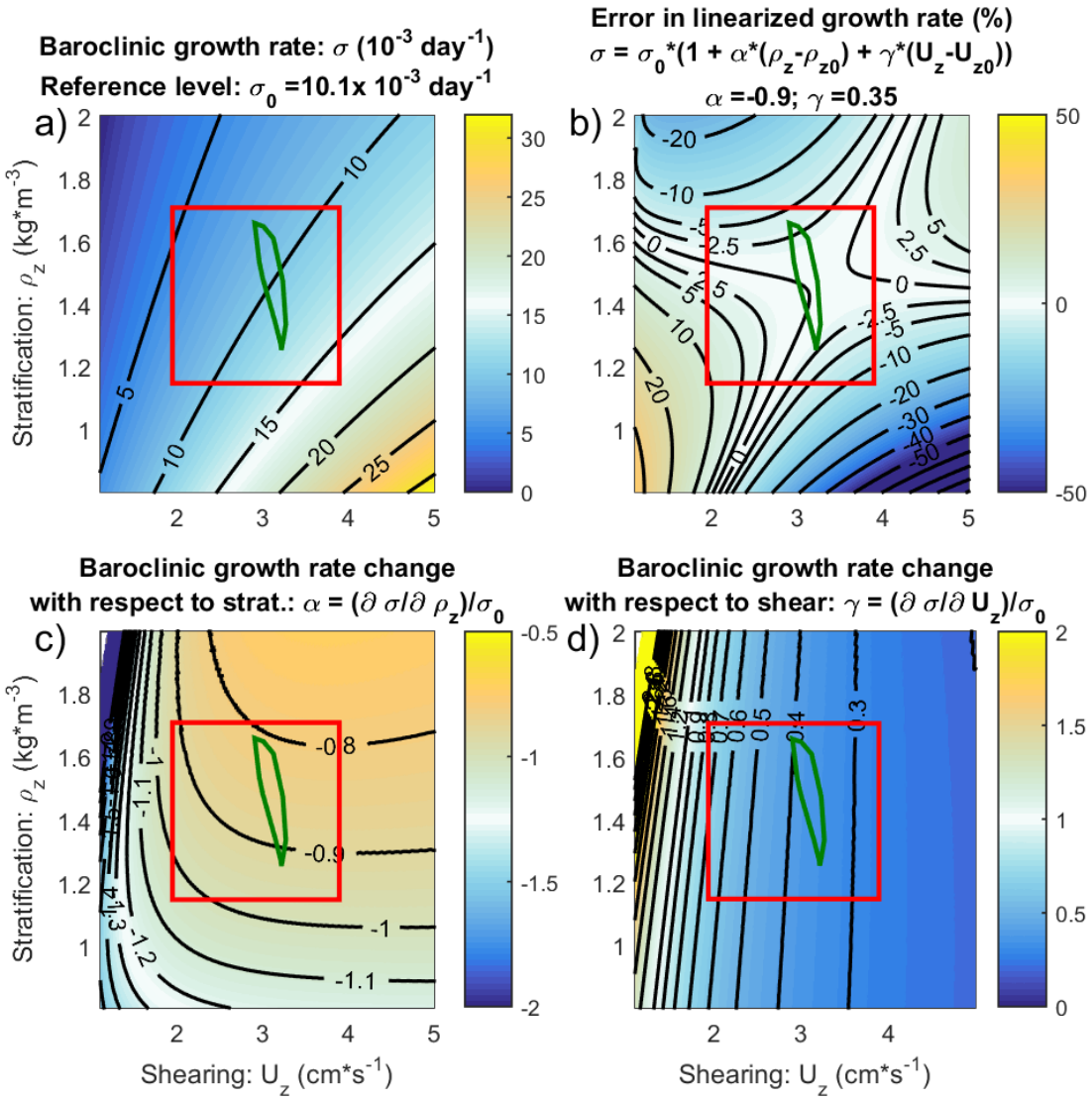

Figure 2.7: Baroclinic instability growth rates over a range of shearing and stratification states. In all plots, the red box indicates the range of average seasonal values across the region. The green line indicates the area-averaged seasonal cycle of shearing and stratification. (a) Baroclinic growth rates. (b) The percent error in a linearized baroclinic growth rate, using a Taylor series expansion. The reference levels are $\sigma_0 = 10.1\text{x}10^{-3}$ day^{-1},, $U_{z0} = 3.1$ cm s^{-1}, and $\rho_{z0} = 1.45$ kg m^{-3}. (c) Relative change in baroclinic growth with respect to stratificiation. (d) Relative change in baroclinic growth with respect to shearing.

While the peak baroclinic growth rate is a non-linear calculation, it is possible to linearize the growth rate around some reference state. By doing this, we are able to tease out the relative importance of the shearing and stratification in affecting the strength of the baroclinic instability. Assuming that changes in the baroclinic growth rate are locally linear at some reference level, after using a Taylor expansion, the baroclinic growth rate can be given by the following equation.

$$\sigma = \sigma_0\big[1 + \alpha(\rho_z - \rho_{z0}) + \gamma(U_z - U_{z0})\big] \tag{2.2}$$

In Eq. 2.2, U_z = the shear, or velocity difference between the layers, ρ_z = the stratification, or density difference between the layers, σ = the baroclinic growth rate, and U_{z0}, ρ_{z0}, and σ_0 = the reference level for the respective terms. α and γ are parameters determined by the local derivative of the baroclinic growth rate at the reference levels, scaled by the reference baroclinic growth rate. They are calculated as $\alpha = (\frac{\partial\sigma}{\partial U_z}|_{\rho_{z0}})/\sigma_0$ and $\gamma = (\frac{\partial\sigma}{\partial\rho_z}|_{U_{z0}})/\sigma_0$. The mean state, spatially and temporally, was used for the reference levels. For the STCC-SEC region, the mean state is U_{z0} = 3.1 cm s^{-1}, and ρ_{z0} = 1.45 kg m^{-3}, giving a reference baroclinic growth rate of $\sigma_0 = 0.0101$ day^{-1}.

Figures 2.7c and 2.7d show the linear rate of change, proportional to the reference baroclinic growth rate σ_0, for changing stratification and shearing (i.e. α and γ), respectively. Fig. 2.7c gives estimates of possible values of α, the stratification parameter. Within the range of variation across the STCC-SEC region, as indicated in the red box, α has a typical value of -0.9. Similarly, in Fig. 2.7d, the shearing parameter γ has typical values of 0.35. These reference parameters will be used in the following section. Figure 2.7b shows the percent error of the linearized growth rate, as given by Eq. 2.2, away from the original, nonlinear growth rate. As can be seen in Fig. 2.7b, the error is within $\pm 2.5\%$ for most possible STCC-SEC ocean states, and only exceeds $\pm 5\%$ in the most extreme states of high (low) shearing and low (high) stratification combinations. This low level of error gives confidence that this linearization of the baroclinic growth rate can be used to simplify the non-linear calculation, and to give estimates of the relative importance of each parameter.

By using the linearization parameters, and the range of variability for the shear and stratification, we can estimate how much the baroclinic growth rate will change. Based upon fluctuations in shear of ± 0.5 cm s^{-1} and a shearing parameter $\gamma = 0.35$, we can expect changes in the growth rate of 1.77 x 10^{-3} day^{-1}, or 17.5% percent of the reference baroclinic growth rate. Stratification fluctuations of ± 0.1 kg m^{-3} and a stratification parameter $\alpha =$ -0.9 indicates that the baroclinic growth rate would vary by ∓ 0.91 x 10^{-3} day^{-1}, or 9% of the reference baroclinic growth rate. If the variation by the two parameters are assumed to be in phase and positively correlated, it can be expected that maximum possible variability in the baroclinic growth rate would be ± 2.68 x 10^{-3} day^{-1}, or 26.5% of the reference growth rate. In the case of this maximum total variability, 66% would be caused by variations in shear and 34% would be caused by variations in stratification. However, the variations do not necessarily occur in phase with each other.

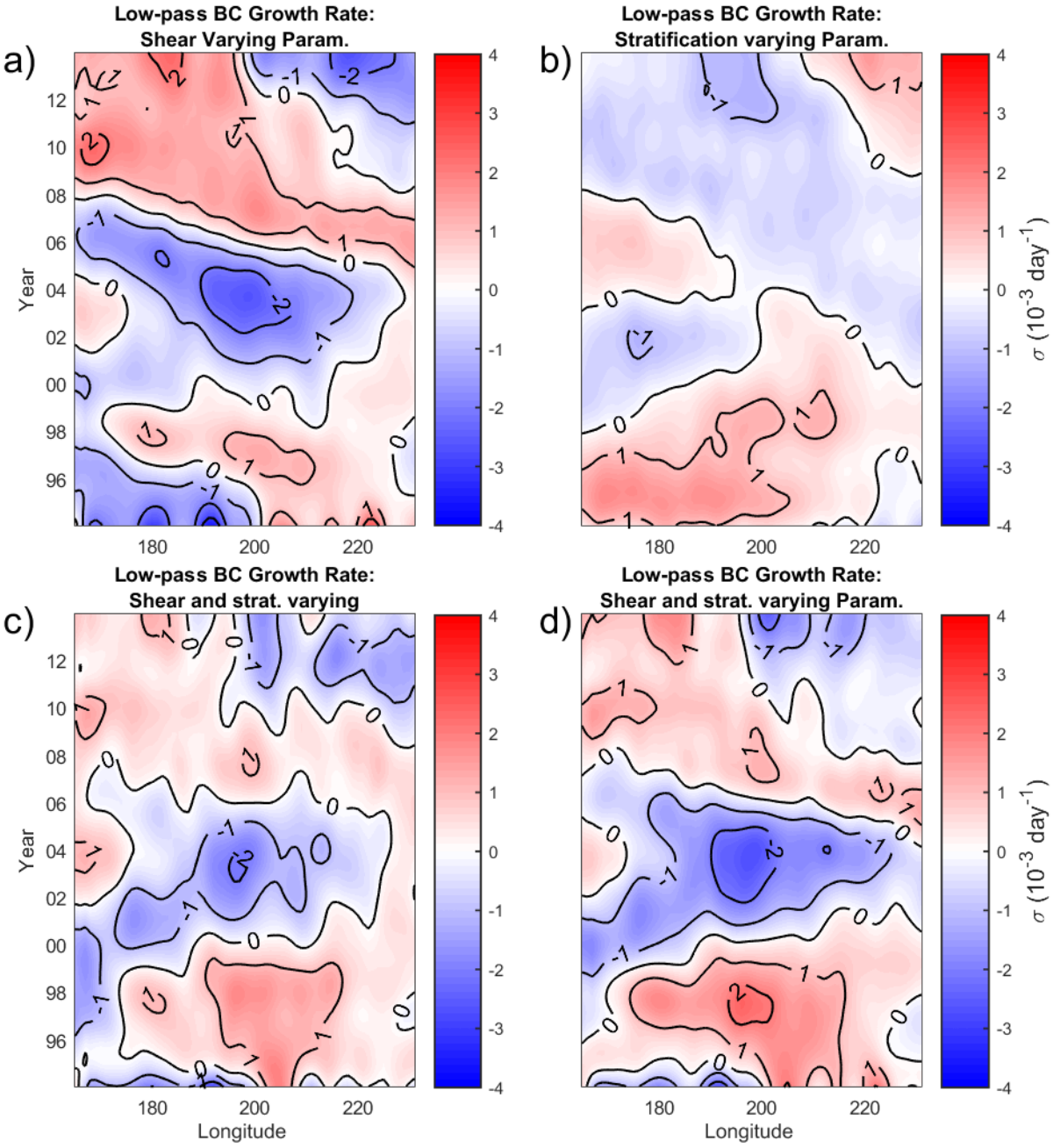

Figure 2.8: Meridionally-averaged bands of baroclinic instability growth rates. The upper row shows the baroclinic growth rate variability, assuming holding a parameter constant. (a) Assuming fixed stratification, and allowing shearing to vary. (b) Assuming fixed shearing, and allowing stratification to vary. (c) Fully non-linear baroclinic growth rates. (d) Baroclinic growth rates, using the linearized growth rate.

When the variations by each parameter are taken as a fraction of the total variability, we find that they contribute in significantly different proportions. Figure 2.8 shows the baroclinic growth anomalies as caused individually by the shear (Fig. 2.8a) and stratification (Fig. 2.8b) parameters. In the early part of the data record, from 1994-1999, both the shear and stratification are contributing to create a particularly high baroclinic growth rate anomalies. In the middle of the record, from 2000-2006, the shearing is particularly weak, whereas the stratification variability shows only slight departures from the mean state. The weak shear state is the primary driver of the low baroclinic growth rates. Finally, during the time period of 2007-2013, the two parameters are mostly working to counteract each other. For a large portion of the region, there is high shearing, but also high stratification. During this time, the shearing would cause a tendency toward particularly high growth rates, but the stratification negates at least part of that variability, and the STCC-SEC region experiences only slightly elevated growth rates.

When the linearized baroclinic growth rate is compared to the fully non-linear calculated baroclinic growth rates, there is a high agreement, with a correlation of 0.86 (Figs. 2.8c and 2.8d). Overall, the character of the two signals matches well, with the periods of highs and lows in the linearized version corresponding to those in the non-linear version. The magnitudes of variation in the linear growth rates are higher than in the non-linear growth rates. The largest discrepancies occur in the central STCC-SEC region from approximately 180°E-200°E. As this region corresponds to some of the highest mean shear in the STCC-SEC region, it would be a more significant departure from the reference state used to linearize the growth rate, and it would be expected that the linearization would overestimate these growth rates.

The low-frequency variability of the baroclinic growth rate, as shown in Fig. 2.8c, and the low-pass EKE signal, as shown in Fig. 2.4a show excellent agreement. There is relatively high correlation of 0.66 between the two signals. The patterns of highs and lows are very similar. In describing both the baroclinic growth rate and the eddy kinetic energy patterns, it can be said that there is widely elevated signal from 1994-1999, followed by a depressed

signal from 2000-2006. From 2007-2014, there is a rebound in the west, while the east has a slight positive anomaly between 2005-2007 before returning to a negative period.

2.5 Summary and Discussion

Using more than two decades of satellite altimetry data, the low-frequency spatial-temporal patterns of EKE variability are described. The combined use of ECMWF ORAS4 ocean reanalysis data for an extended data record, and gridded Argo float data for verification purposes provides a record of the subsurface state of the ocean. This data is used to calculate the theoretical strength of baroclinic instabilities in an idealized 2 1/2-layer system, which are believed to be the cause of the eddy activity in the STCC-SEC region. Through the linearization of the dominant parameters affecting the strength of the instabilities, it is found that the changes in the shearing and stratification of the STCC-SEC system are both significant. In the range of maximum variability, the effect of changing shear would be roughly twice as large as that of changing stratification.

Further examination of the state of the STCC-SEC region allows the relative effects of changing temperature and salinity to be explored. The relative effect on changing stratification is seen directly through the change in density fields. Changes in the shear are found by using a thermal wind balance on the linearized state equation, and integrating through the layer depth. When the parameters are compared, the contribution of salinity variability is approximately 50%-75% of the temperature variability, for both the stratification and shear.

A number of papers have explored the variability in the South Pacific caused by the gyre spin-up. The increased wind stress curl over the larger ocean is found to have a clear effect on sea level trends (Qiu and Chen 2006; Roemmich et al. 2007; Sasaki et al. 2008), among others). Baroclinic Rossby wave adjustment to the changing basin-scale wind stress curl is largely able to account for the observed sea surface height variability (Qiu and Chen 2006); however, the one region where these dynamics break down is in the STCC-SEC region. Nevertheless, the decadal patterns of temperature variability agree well with the local sea surface height variability, and exhibit features of Rossby wave propagation. In agreement

with Chelton and Schlax (1996) and Wang et al. (1998), the observed propagation speed is roughly 6.5 cm s^{-1}, and exceeds that as predicted by linear theory. In further investigating sea level trends in the region, Bowen et al. (2006) were able to find that a combination of local wind and heat forcing are able to explain between 40% to 60% of the sea surface height variability. However, a large portion of this variability remains unexplained. Eddy activity could be a driver of this variability. Indeed, in the North Pacific, it has been shown by Qiu et al. (2015) that eddy activity can be a significant driver of regional sea level variability. If a similar dynamic exists in the South Pacific, it is fair to expect the low-frequency variability of eddy activity in the STCC-SEC region to impact the regional sea level change. Future work will be needed to investigate this change.

Greatbatch et al. (2010) looked into the effect of eddy-driven transport in the Gulf Stream region, and found that the eddy-momentum fluxes can be a significant driver of circulation. While the South Pacific STCC would have a weaker forcing, it is possible that the eddy activity in the STCC-SEC band has a similar effect on transport in the region. An investigation of this circulation feature could help to explain the transports in the region, and how they relate to the larger, wind-driven gyre circulation.

There are likely many connections to forcings from the atmosphere, with many varied effects. Kessler and Gourdeau (2007) found that linear wind forcing can explain annual thermocline depth variability in the southwest interior South Pacific through Rossby wave dynamics. Additionally, local wind stress forcing can cause anomalous Ekman pumping/suction. Morris et al. (1996) used this framework to explore the annual density variability, although Kessler and Gourdeau (2007) note that this does not preclude the presence of Rossby waves. If significant, the decadal variability of the strength of this local forcing could be a factor in the changing state of the waters of the STCC-SEC region. A number of papers (Martinez et al. 2009; Montecinos and Pizarro 2005; Hill et al. 2011), among others) have looked at the effect of large, basin-scale forcings and their impact on circulation and the state of the ocean across the South Pacific, and in some cases, their connection to various climate indices. For example, Cai (2006) and Roemmich et al. (2007) examine the connection of the larger South

Pacific gyre spinup to the Southern Annual Mode (SAM), while Sasaki et al. (2008) explore the connection to ENSO-like variability. Zilberman et al. (2014) looked into the effect of the SAM on mid-latitude meridional transport, which could directly effect the STCC-SEC region by advecting anomalous waters into the region. Additionally, the same indices could have changes on local forcing. Zhang and Qu (2014) showed connections of sea surface salinity variability to the shifting of the South Pacific Convergence Zone (SPCZ) by altering evaporation-precipitation patterns, and this connection to the Pacific Decadal Oscillation (PDO). The shifting of the SPCZ could have local forcing through changes in sea surface salinity and temperature, and through local wind forcing (Ganachaud et al. 2014).

Lastly, further work is also needed to investigate the topographic influence on the region. As noted in the introduction, within the STCC-SEC region, there are hot spots of eddy activity which correspond well with topographic features such as the Kermadec Ridge. These are also the regions in which there is weaker correspondence between variability in the eddy activity and variability in the strength of baroclinic instabilities. The strong topographic features, with some peaks extending to less than 500 meters below the surface, could have steering effects of the circulation of the region. Additionally, these sites could be sources of wave generation (Anderson and Killworth 1977) or even eddy disruption, dissipation, or reorganization (Adcock and Marshall 2000; Dewar 2002). The connection of these direct topographic influences, as well as the connections to larger atmospheric forcings, would give greater insight into the character of these eddy activity variations and the role they play in the larger South Pacific oceanic variability.

CHAPTER 3
DYNAMICAL FORCING OF EDDY ACTIVITY IN THE SOUTH PACIFIC SUBTROPICAL COUNTER-CURRENT

Abstract

Mesoscale eddy activity variability on interannual to decadal time scales in the South Pacific Sub-tropical Counter-current (STCC) is caused by changes in the strength of baroclinic instabilities. Eddy activity, as observed through eddy kinetic energy (EKE), has been found to be strongly correlated to the baroclinic growth rate, and has significant longitudinal variation. The baroclinic growth rate is set by variations in the magnitude of regional stratification and vertical zonal velocity shear, which can be understood through spatial and temporal changes in temperature and salinity. Temperature and salinity patterns in the ocean can be driven by local heat and moisture fluxes and by the advection of temperature and salinity gradients. It is expected that local changes, such as those caused by changes in the South Pacific Convergence Zone (SPCZ), would be a dominant driver of surface forcing, whereas basin-scale wind pattern shifts could alter gyre circulation and the advection of anomalous water properties into the region. This work will examine the relative importance of each forcing term on the state of the ocean and subsequently, how these changes affect how baroclinically unstable the region is. Through these connections, changes in eddy activity in the STCC can be linked to changes in dynamical forcings. Lastly, connections of these forcings to larger climatic patterns, such as the Interdecadal Pacific Oscillation (IPO), will be explored.

3.1 Introduction

In the western South Pacific, the Subtropical Counter-current (STCC) is a relatively weak, eastward flowing current and is a highly eddying region located in a band roughly between 20° - 30°S. This current lies north of New Zealand and flows into the open South Pacific. While the current has typical speeds of 3-5 cm s^{-1}, the currents associated with eddies can be up to an order of magnitude faster. The eddies in the region have been previously found the be generated through baroclinic instabilities (Qiu et al. 2008; Rieck et al. 2018; Travis and Qiu 2017). The current overlays the mean westward flow of the South Equatorial Current (SEC), a component of the larger South Pacific Gyre circulation. This vertically sheared system provides a suitable environment for the development of baroclinic instabilities.

Travis and Qiu (2017) looked at the decadal variability of the eddy activity in the STCC, and found that the changing eddy kinetic energy (EKE) could be related directly to the changing strength of the baroclinic instability through variability in the shear and the stratification in the region. There are a number of likely causes for the variation in the strength of these parameters such as changes in the momentum fluxes from wind forcing and net buoyancy fluxes. Net heat fluxes in the region would correspond well to seasonal fluctuations in the temperature in the region, and thereby the density of the upper layer of the ocean. However, on interannual time scales, Travis and Qiu (2017) found that the majority of the EKE variations could be attributed to shear variability. If variability in velocity structures are the dominant driver of changes in the stability of the STCC region, it is reasonable to expect that they could also dominate changes in the state of the ocean through the advection of anomalous waters in and out of the region. However, without fully investigating each of these forcing terms, their relative contributions cannot be quantified.

Through model simulations, Rieck et al. (2018) looked at decadal variations in the south-eastern extension of the STCC (25-33°S,175-153°W), an area with the distinctive property that the decadal variability of EKE is on the same order as the time mean EKE. Rieck et al. (2018) explored the relative effects of buoyancy and momentum fluxes, and concluded that the wind forcing is the dominant mechanism leading to decadal EKE variability in this branch

of the STCC. They found that changing local wind stress curl can drive changes in local density gradients, while in the eastern South Pacific, wind stress curl anomalies can generate Rossby waves, which can propagate westward, carrying density perturbations. These density perturbations can cause changes in the meridional density gradient and therefore changing vertical shear of zonal velocity, which can subsequently lead to changing EKE. It was also found that this response can be correlated to the Interdecadal Pacific Oscillation (IPO).

However, when considering the wider STCC area (165°E-130°W, 22° -28°S), a number of additional features need to be considered. (Kessler and Gourdeau 2006) found that linear wind forcing can impact annual pycnocline depth variability through Rossby wave dynamics, and Qiu and Chen (2006) found that Rossby wave dynamics are very important and useful in describing decadal variability of changes in sea surface height across the South Pacific; however, they do note that in the western tropical South Pacific, in the STCC band, Rossby wave dynamics have less skill in explaining SSH trends, and hypothesize that additional impacts by the western Pacific warm pool could be important.

Another important feature to consider is the South Pacific Subtropical Convergence Zone (SPCZ), which lies just to the north of the STCC. The SPCZ is a region of the convergence of northeasterly winds from the Pacific subtropical pressure high and the southeasterly winds for higher latitudes, leading to an atmospheric moisture convergence, and a broad, persistent band of clouds. The SPCZ has a mean position as a diagonal axis extending southeastward from near New Guinea, at approximately 6°S, 144°E to about 30°S, 120°W (Vincent 1994). Shifting of the SPCZ has been shown to affect local precipitation rates (Griffiths et al. 2003), and thereby impacting the surface salinity front (Gouriou and Delcroix 2002). A number of studies (Haffke and Magnusdottir 2013; Borlace et al. 2014; Gouriou and Delcroix 2002; Folland 2002; Kidwell et al. 2016) have explored the connection between the SPCZ and climatic indices such as ENSO and IPO. These climatic patterns have been shown to be connected to alter the location, orientation, and extent of the SPCZ, which could directly impact the wind patterns and buoyancy forcings at the eastern boundary of the extent of the STCC under consideration.

Lastly, changes in deeper gyre circulation could impact the overall circulation patterns; more directly, the change in the relative velocities between the eastward flowing STCC at the surface and the deeper SEC, the westward flowing branch of the South Pacific gyre circulation. While the greatest variability in shear and strain is due to changes in the state of the STCC in the upper ocean, the low-frequency changes in the deeper SEC should not be discounted without exploring these dynamics. A number of studies have looked at a decadal spin-up of the South Pacific Gyre and it's connection to basin-wide wind stress curl increases (Kessler and Gourdeau 2006; Qiu and Chen 2006; Roemmich et al. 2007, 2016; Schneider et al. 2007). Zhang and Qu (2015) observed that this spin-up of the gyre has caused a 20% to 30% increase in SEC transport, while additionally finding that the linear trend of deep ocean steric height (1000-1800m) between 22-38°S is caused by salinity and temperature changes acting in concert, which is reverse of the upper ocean, in which density-compensating patterns of temperature and salinity changes were observed by Roemmich et al. (2016).

This study will examine surface buoyancy and momentum fluxes to assess direct forcings of the STCC, while larger, regional changes in the wind fields will be explored for their impact of remote forcings which can propagate into the STCC region or alter the overall gyre circulation patterns. A study of the forcings of the eddy activity in the STCC region will need to look at momentum fluxes through wind stresses and buoyancy fluxes through heat and moisture fluxes. For this region, a dynamically and thermodynamically consistent model will be needed so that the impacts of specific processes can be connected directly to observed changes in the ocean states. For this reason, this study will use model output from Estimating the Circulation and Climate of the Ocean, phase II (ECCO2). As will be described (Section 3.2.1), the ECCO2 model output is designed to be dynamically and thermodynamically consistent, and as such, will be ideal for the purposes of this study. Lastly, these larger wind and buoyancy forcing patterns will be explored for their connection to broader climatic indices, such as the IPO and ENSO.

3.2 Methodology

3.2.1 Data Sets

Model output is taken from the ECCO2 ocean state estimate. The ECCO2 model is based upon the Massachussetts Institute of Technology General Circulation Model (MITgcm; Marshall et al. (1997)). This is a three-dimensional, z-level, hydrostatic and Boussinesq global ocean model, and uses a cubed-sphere grid projection (cube92 version). The model has a mean horizontal grid resolution of 18 km. Vertically, the model has 50 levels, with 10 m level spacing in the upper 600 m, increasing to 456 m near the lowest levels, with a maximum depth of 6150 m. A least squares fit of the MITgcm to available satellite and in situ observational data is used to obtain an ocean state estimate, and Green's function approach is utilized to optimize a number of control parameters (Menemenlis et al. 2008). These include initial temperature and salinity conditions, surface boundary conditions, background eddy viscosity and diffusivity, and bottom drag. These optimized parameters are then used in the model, which is run forward unconstrained, just as in other prognostic model simulations. In the forward run, no additional observational data are used to interrupt the run, allowing the model to be dynamically and thermodynamically consistent (Wunsch et al. 2009). This model has been used extensively for similar eddy energetic studies (Fu 2009; Chen et al. 2014; Zemskova et al. 2015; Yang et al. 2017; Qiu et al. 2017). The three-dimensional data taken from this model includes zonal, meridional, and vertical velocities, and temperature, salinity, and density. These data are provided in 3-day time steps. Surface parameters include sea surface height, net heat flux, net moisture flux, and zonal and meridional wind stress. The wind stress data are used to calculated wind stress curl and wind stress divergence. The surface parameters are given a 1-day time steps. For consistency, the ECCO2 surface parameters are downsampled to match the 3-day time steps of the three-dimensional data from the ECCO2 state model by taking 3-day averages of daily data to match the three-dimensional time interval.

For observational comparisons, the Aviso satellite altimetry data, as processed by CNES/CLS,

is used. The data has a 0.25° x 0.25° spatial-resolution, and a 1-day temporal-resolution. Absolute dynamic topography is used for sea surface height (SSH), while geostrophic velocities are also available, and will be used. The data were analyzed from January 1993 to December 2017. The satellite altimetry data is also downsampled to 3-day time steps to match the ECCO2 state model data.

For additional validation of ocean state parameters, such as temperature, salinity, and velocities, the European Centre for Mid-Range Weather Forecasts (ECMWF) Ocean Reanalysis Version 5 (ORAS5) is used (Zuo et al. 2019). ORAS5 is an ocean state reanalysis product, which incorporates observational data into model runs to "correct" for inaccuracies in the model output as compared to observational data. As such, this data product is not appropriate for ocean state budget analyses, as the corrections introduce artificial fluxes to bring the model state towards the observed values. However, as the reanalysis model seeks to reproduce observed states more accurately, it can be a useful tool to check how well the ECCO2 product reproduces the basic ocean state (temperature and salinity fields, currents) and the related interannual variability.

3.3 ECCO2 Validation

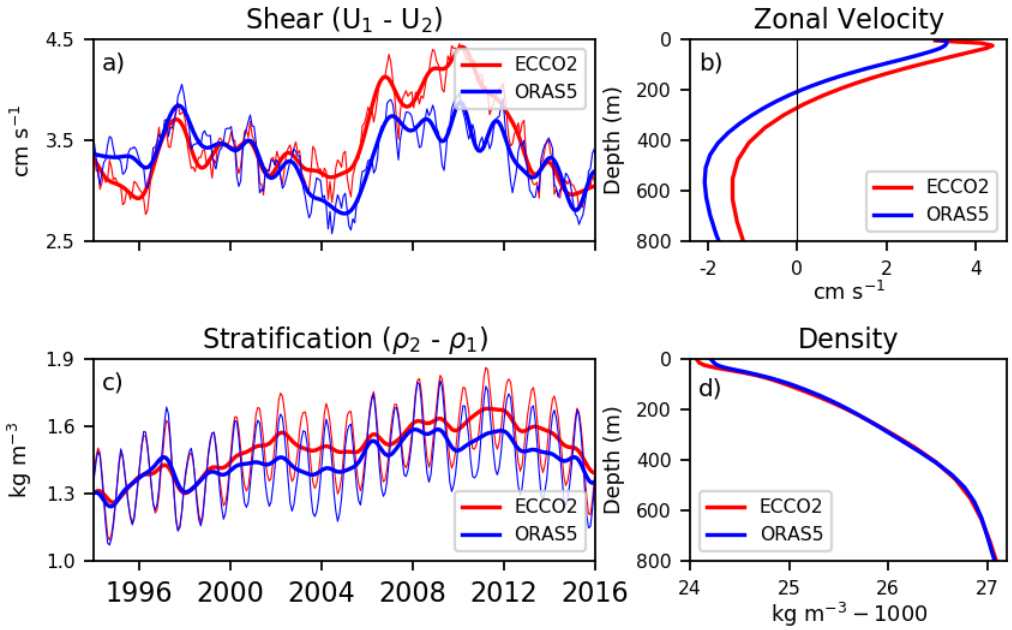

Figure 3.1: Comparison of zonal velocity and density data between the ECCO2 model output and ORAS5 reanalysis output. Shearing is calculated as the difference between the upper and lower layer averaged zonal velocity, while stratification is the difference between the lower and upper layer averaged density. The upper layer is defined as the surface to 200m depth. The lower layer is defined as 200m to 600m depth. The area is defined as 165°E - 130°W, 22°S - 28°S. The time period of consideration is January 1st, 1993 - December 31st, 2018. The thin lines are the area-averaged data, while the thick lines are low-pass filtered (< 1 yr^{-1}). a) Time series of the area and depth averaged shear. b) Vertical profile of the area and time averaged zonal velocity. c) Time series of the area and depth averaged stratification. d) Vertical profile of the area and time averaged density.

In Figure 3.1, comparison is shown between the ECCO2 data and the ORAS5 data for the two most relevant ocean state parameter: density and zonal velocity. Vertical profiles of the area and time averaged zonal velocity and density in the STCC are shown in Figures 3.1b and 3.1d, respectively. Zonal velocity in the ECCO2 data set is approximately 0.2 cm s^{-1} stronger in the eastward direction than the ORAS5 data at all depths. The difference is smallest at the surface and largest near 500 m depth. The density profile of the ECCO2 data is approximately the same as that of the ORAS5 data, with a small difference in the upper

40 m, in which the ECCO2 density is less than the ORAS5 by approximately 0.15 kg m^{-3}. Figures 3.1a and 3.1c show the area-averaged time series of the shear and stratification in the STCC region in the ECCO2 and ORAS5 data. Shear and stratification are defined as the difference in zonal velocity and density, respectively, between an upper and lower ocean layer. For the purposes of this comparison, the upper layer is defined as 0-200m depth, while the lower layer is defined as 200-600m depth. This choice in layer set-up is chosen for simplicity in calculation, as well as for congruity with Travis and Qiu (2017). In Figure 3.1a, we see that the time-varying ECCO2 shear compares well with the ORAS5 shear. They follow similar low-frequency patterns of highs and lows, with the low-passed ECCO2 data showing higher shear during the second half of the data record. Overall, the low-frequency shear patterns show high agreement, with a correlation of 0.734 between the two datasets. Figure 3.1c also shows high agreement between the two datasets in the stratification patterns. The ECCO2 data is more stratified during some periods, but shows similar overall patterns, and has a correlation of 0.925 with the ORAS5 data.

3.3.1 Methods

Travis and Qiu (2017) found significant spatial and temporal variability in eddy activity in the STCC on decadal timescales. In that study, changes in shear and stratification were shown to lead to changes in the strength of baroclinic instability and were found to be highly correlated to changes in EKE. Additionally, the changes in shear and stratification were connected back to changes in the temperature and salinity fields. This study will utilize the ECCO2 model output to examine the drivers of the temperature and salinity fields. Once found, these can then be linked to changes in shear and stratification, and subsequently, to the strength of the baroclinic instabilities through the baroclinic growth rate.

Following other studies (Qiu and Chen 2004; Qiu et al. 2008; Travis and Qiu 2017), the STCC region can be represented as a 2-1/2 layer model, with the eastward STCC being contained in the upper layer, the westward flowing branch of the SEC existing in the lower layer, and an assumed quiescent layer at depth. From this idealized set-up, the baroclinic

growth rate can be calculated (see Appendix). In this set-up, an instability criterion is found to be:

$$U_1 - U_2 > \frac{(\rho_2 - \rho_1) g H_2}{\rho_0 f_0^2} \beta + \frac{\rho_2 - \rho_1}{\rho_3 - \rho_2} U_2, \tag{3.1}$$

where U_1, U_2 = depth-averaged zonal velocity for the upper and lower layers, respectively, ρ_1, ρ_2, ρ_3 = depth-averaged density for the upper, lower, and quiescent layers, respectively, g = gravitational acceleration, H_2 = lower layer thickness, f_0 = Coriolis parameter at a reference latitude, and β = beta parameter at a reference latitude. (U_1 - U_2) = the zonal velocity between the active layers, hereafter called the layer shear, and (ρ_2 - ρ_1) = density difference between the active layers, hereafter called the layer stratification. The criterion indicates that the layer shear needs to exceed the baroclinic Rossby wave speed (the first term on the right-hand side on the inequality) plus a scaled advection by the lower layer (the second term on the right-hand side of the inequality). In both of these terms, the layer stratification is an important parameter. For this reason, the primary parameters to be studied are the layer shear and the layer stratification.

Using the ECCO2 model output, temperature and salinity budgets will be calculated. The governing equations for the upper ocean temperature and salinity budgets can be written as follows:

$$\frac{\partial T}{\partial t} = -\mathbf{u} \cdot \nabla T + \frac{1}{\rho_0 C_p} \frac{\partial q}{\partial z} + K_h \nabla_h^2 T + \frac{\partial}{\partial z}\left(K_z \frac{\partial T}{\partial z} \right) \tag{3.2}$$

$$\frac{\partial S}{\partial t} = -\mathbf{u} \cdot \nabla S + \frac{S}{\rho_0} \frac{\partial F_W}{\partial z} + K_h \nabla_h^2 S + \frac{\partial}{\partial z}\left(K_z \frac{\partial S}{\partial z} \right) \tag{3.3}$$

In these equations, $\mathbf{u}$=(u,v,w), the three-dimensional velocity vector, ρ_0 is the reference seawater density, C_p is the specific heat of seawater, ∇ is the three-dimensional gradient operator, ∇_h^2 is the horizontal Laplacian operator, and K_h and K_z are the horizontal and vertical eddy diffusivity coefficients, respectively. Heat flux is represented by q, while freshwater flux is represented by F_W. Freshwater flux is the difference between precipiation

and evaporation (i.e., F_W = P - E). In the ECCO2 data, positive q represents net heat flux into the ocean (i.e., heating the ocean), and positive F_W represents net water mass flux into the ocean (i.e., decreasing salinity).

In evaluating the influence of the various processes affecting these budgets, and for consistency with the 2-1/2 layer idealized system, these budgets will be analyzed by integrating through each layer, and dividing by the layer depth to get the depth-averaged budget equations for the upper layer:

$$\frac{\partial}{\partial t}\Big(\frac{1}{H_1}\int_{-H_1}^{0} T\Big) = -\frac{1}{H_1}\int_{-H_1}^{0} \mathbf{u}\cdot\nabla T + \frac{Q_{net}}{\rho_0 C_p} + \left(\frac{K_h}{H_1}\int_{-H_1}^{0} \nabla_h^2 T + \frac{K_z}{H_1}\frac{\partial T}{\partial z}\Big|_{H_1}\right) \tag{3.4}$$

$$\frac{\partial}{\partial t}\Big(\frac{1}{H_1}\int_{-H_1}^{0} S\Big) = -\frac{1}{H_1}\int_{-H_1}^{0} \mathbf{u}\cdot\nabla S + \frac{SF_w}{\rho_0 H_1} + \left(\frac{K_h}{H_1}\int_{-H_1}^{0} \nabla_h^2 S + \frac{K_z}{H_1}\frac{\partial S}{\partial z}\Big|_{H_1}\right) \tag{3.5}$$

In these equations, the first term on the left hand side of the equations are the time rate of change of temperature and salinity, respectively. The first terms on the right hand side represent the advective temperature/salinity flux convergence. The second term on the right hand side of the temperature equation represents the net heat exchange at the sea surface, while the second term on the right hand side of the salinity equation represents the net freshwater exchange at the surface. The last terms on the right hand side represent the diffusive temperature/salinity flux convergence due to subgrid scale perturbations in the model. Data availability from the 3-day ECCO2 product does not allow for accurately evaluating the diffusive convergence terms. However, as has been previously stated, the ECCO2 model is internally consistent, and as such, the diffusive terms can be assumed to be equal to the residual from the other three terms in the temperature and salinity equations. Similar equations as 3.4 and 3.5 can be written for the second layer.

For the purposes of the exploration of low-frequency changes, as well as for more direct application to calculating the baroclinic growth rates, these budget equations can be more

conveniently examined by removing seasonal, high-frequency variability (i.e., periods < 15 months), and then integrating the equations in time. The resulting calculations directly give the time-varying temperature and salinity signals and the relative contributions to those signals from each terms in the budget (advective, diffusive, and heat and freshwater flux terms for the temperature and salinity equations, respectively).

By assuming a linear density equation, the temperature and salinity budgets can be written in terms of density through the following relation:

$$\rho = \rho_0\Big(1 - \alpha(T - T_0) + \beta(S - S_0)\Big) \tag{3.6}$$

In this equation, α = thermal expansion coefficient, T_0 = reference layer temperature, β = saline expansion coefficient, and S_0 = reference layer salinity. Additionally, by assuming that the system is primarily zonal flow and assuming a thermal wind balance, a relationship to the shearing in the system can be found:

$$f\frac{\delta U_g}{\delta z} = \frac{g}{\rho_0}\frac{\delta \rho}{\delta y} \tag{3.7}$$

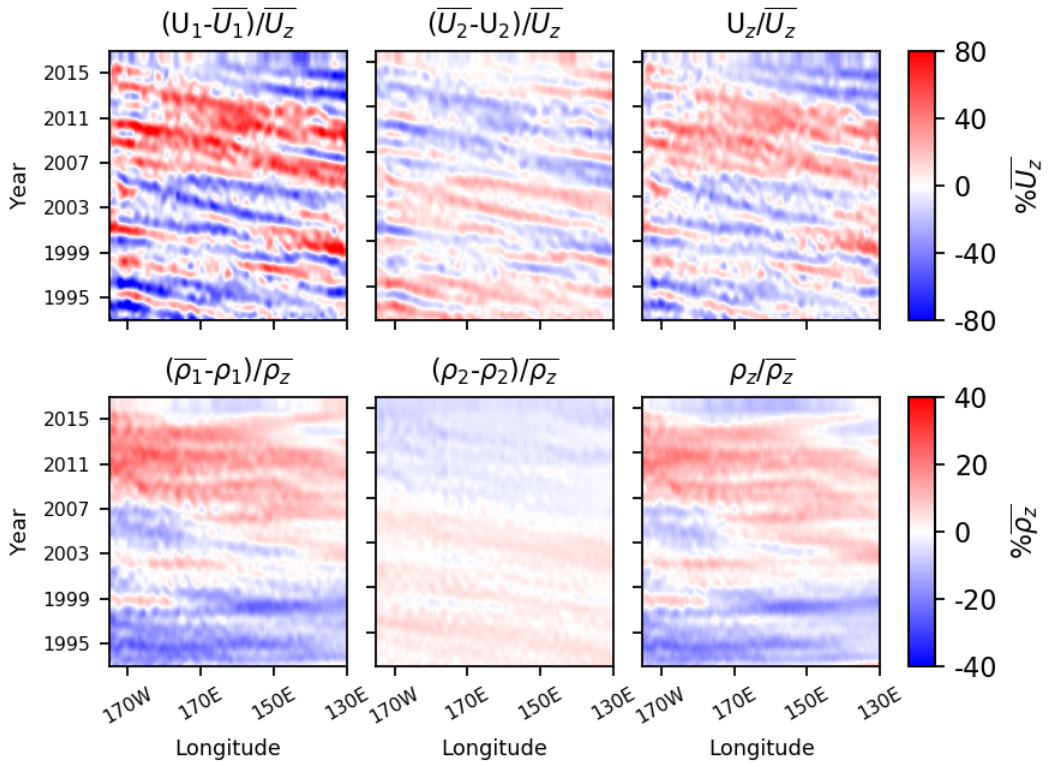

Figure 3.2: The upper row (a,b,c) shows the total variability in layer shear as a percent of the mean layer shear ($\overline{U_z}$ = $\overline{U_1}$ - $\overline{U_2}$). a) Layer shear variability with only upper layer varying. ((U_1 - $\overline{U_2}$ - $\overline{U_z}$)/$\overline{U_z}$) b) Layer shear variability with only lower layer varying. (($\overline{U_1}$ - U_2 - $\overline{U_z}$)/$\overline{U_z}$) c) Layer shear variability with both layers varying. (U_z/$\overline{U_z}$) The lower row (d,e,f) shows the total variability in layer stratification as a percent of the mean layer stratification ($\overline{\rho_z}$ = $\overline{\rho_2}$ - $\overline{\rho_1}$). d) Layer stratification variability with only the upper layer varying. (($\overline{\rho_2}$ - ρ_1 - $\overline{\rho_z}$)/$\overline{\rho_z}$) e) Layer stratification variability with only the lower layer varying. ((ρ_2 - $\overline{\rho_1}$ - $\overline{\rho_z}$)/$\overline{\rho_z}$) f) Layer stratification variability with both layers varying. (ρ_z/$\overline{\rho_z}$)

Shear and stratification in the 2-1/2 layer system are represented as the difference in velocity and stratification between the upper and lower layer, respectively. Layer shear is represented as: U_z = U_1 - U_2. Layer stratification is represented as ρ_z = ρ_2 - ρ_1. As can be seen in Figure 3.2, variation in the upper layer (Figures 3.2a and 3.2d) is the most significant driver of these two parameters. For this reason, analysis of the drivers of low-frequency variability in these parameters through temperature and salinity budgets will be restricted to the upper layer.

To determine the depth layers used in the 2-1/2 layer system, profiles of averaged zonal shear and averaged meridional potential vorticity gradients are first calculated. For a positively sheared system (i.e., $U_z > 0$), the upper layer potential vorticity gradient is necessarily positive (refer to Appendix Eq. A.3 for layer 1), and a necessary and sufficient criterion for a baroclinically unstable system is that the lower layer potential vorticity gradient is negative. From the ECCO2, we can calculate the vertical shear of zonal velocity and the potential vorticity gradients as:

$$\frac{\partial}{\partial y}(PV) = \frac{\partial}{\partial y}\Big(- \frac{f}{\rho}\frac{\partial \sigma}{\partial z}\Big), \tag{3.8}$$

where PV = potential vorticity, f = Coriolis parameter, g = gravitational acceleration, ρ_0 = reference density, and $\sigma = \rho$ - 1000 kg m^{-3}.

For consistency in calculations and with a 2-1/2 layer framework, a final constraint on determining layer parameters is applied, stating that the lower layer should not outcrop at all in the study region. Using the criteria that the lower layer should have a negative PV gradient, there should be positive shear between the upper and lower layers, and that the lower layer should not outcrop in our study region, we see that the most relevant isopycnals are $\sigma_1 = 25.75$, $\sigma_2 = 26.8$, and the bottom, quiescent layer is integrated from the bottom of the lower layer to a depth of 2000 m. The choice of σ_1 lies below the reversal in the sign of the PV gradient, but is at a depth which allows for ensuring that isopycnal outcropping is minimized. Additionally, the deeper isopycnal choice ensures that the core of the eastward flowing STCC and the regions of greatest positive shear are captured in the upper layer.

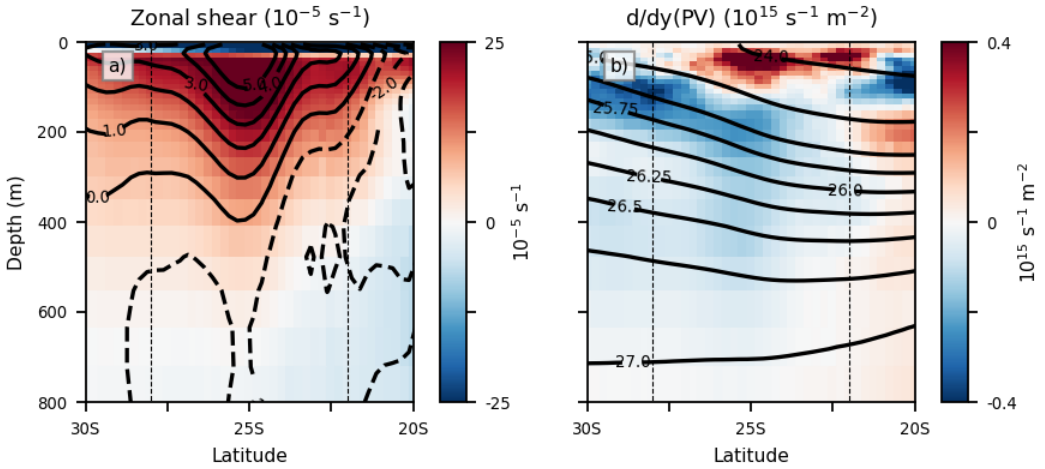

Figure 3.3: Zonally-averaged profiles of zonal velocity, vertical shear of zonal velocity, meridional gradients of potential vorticity (PV), and density. Profiles are averaged between 165°E-130°W. Vertical dashed lines are shown as 22°S and 28°S, indicating the northern and southern boundaries of the STCC study region. a) Zonal velocity and vertical shear of zonal velocity. Red/blue shading indicates zonal velocity shear, while black contours indicate zonal velocity, given in (cm s^{-1}). Solid contours indicate eastward flow, while dashed contours indicate westward flow. b) Density and meridional gradient of PV. Red/blue shading indicates PV gradient, while black contours indicate isopycnals, given as (kg m^{-3} - 1000)

Using these chosen values, each layer is averaged between the respective isopycnals (i.e., layer 1 = surface to σ_1, layer 2 = σ_1 to σ_2, layer 3 = σ_2 to 2000 m). This gives average depths of 235 m for the upper layer and 530 m for the lower layer. These depths are approximately equivalent to those used in the 2-1/2 layer set-up in Travis and Qiu (2017). By using isopycnal surfaces to define layers instead of fixed layer depths, isopycnal uplift or depression caused by Rossby wave propagation is intrinsic in the observations, and the effect on observed ocean state parameters within those moving layers is minimized.

Lastly, similar to Travis and Qiu (2017), a comparison to a fully non-linear baroclinic growth rate (BCR) and a linearized BCR will be performed. Through a linearization of the local BCR, the relative importance of each term in the temperature and salinity budget equations to the BCR can more directly be determined. A reference BCR can be determined

using mean state parameters of shear and stratification, and then, through a Taylor expansion about the mean state, the effect of anomalous shear and stratification can be determined. Subsequently, the influence of the forcing factors on the temperature and salinity fields and their influence on the changing shear and stratification fields can be directly related to the baroclinic growth rates.

3.4 Results

Before looking at how the ocean state variability can impact eddy activity in the STCC region, it is useful to first understand the mean state. This is shown in Figure 3.4, which shows maps of the impact of the mean, low frequency trend in each of the forcing terms in the budget equations. For instance, Figure 3.4a shows the impact of net heat flux forcing, which broadly shows a negative pattern across the STCC band, indicating a general cooling trend in the region, with heat being released by the ocean into the atmosphere. This is largely balanced by a horizontal advective temperature flux convergence (Figure 3.4b, showing a net increase in temperature. Similarly, net freshwater flux and horizontal advective salinity flux convergence are shown in Figures 3.4f and 3.4g, respectively. The STCC region broadly shows an increase in salinity due to net freshwater forcing, indicating a net evaporation across the region, which is largely offset by the horizontal advection. These two patterns help us to interpret a general pattern of the advection of warmer, fresher waters into the STCC region, which then evaporate, leading to the increase of salinity and the cooling of the region through latent heat flux. The residual terms, which amount to the diffusive flux terms, have weak signals across the whole region, with patchy patterns. Broadly speaking, the diffusive flux terms are more positive in the north and more negative in the south, and could be indicative of the smoothing of the gradients across the region, where eddies span a transition from warm, salty waters to the north and fresher, colder waters to the south. Figures 3.4e and 3.4j show the seasonally-averaged component of each term in the temperature and salinity budgets, respectively. On a seasonal basis, temperature variability is primarily driven by changes in heat flux, while salinity variability is driven by freshwater flux variability, which

is slightly offset by changes in the advective flux terms.

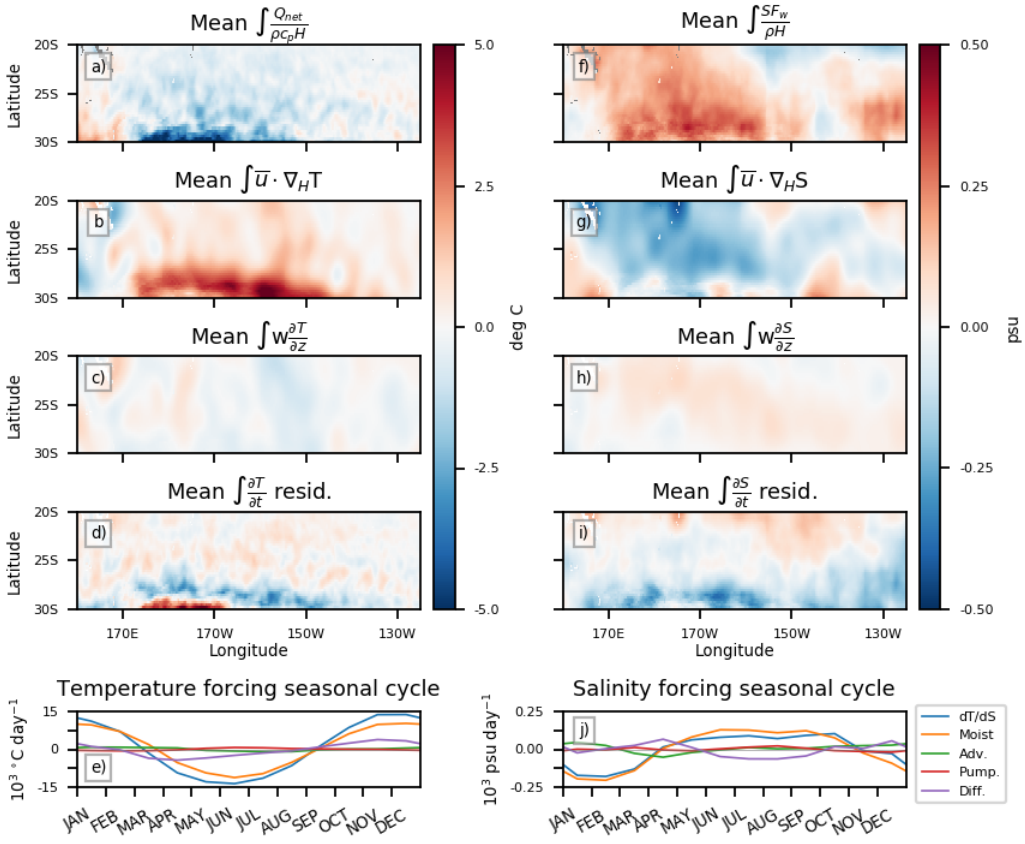

Figure 3.4: Mean contributions of each term to net temperature and salinity forcing.

3.4.1 Eddy Kinetic Energy

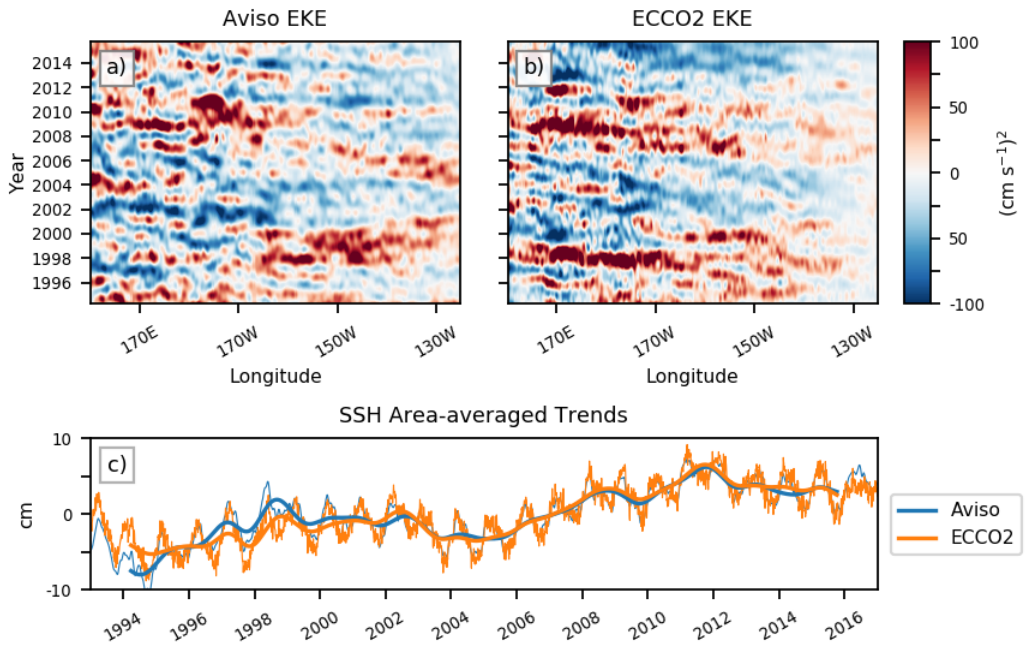

Figure 3.5: ECCO2 vs Aviso Variability. Figures a) and b) show low-frequency variability in eddy kinetic energy (EKE) across the STCC band, averaged between 22°S to 28°S. a) EKE variability, as derived from Aviso geostrophic velocity anomalies. b) EKE variability, as derived from ECCO2 geostrophic velocity anomalies. c) Time series of area-averaged sea surface height (SSH), as compared in Aviso and ECCO2. The area over which SSH is averaged is 165°E-130°W, 22°S-28°S. The thin lines indicate the area-averaged SSH signal, while the thick lines indicate the low-pass filtered (period $>$ 15 months) SSH variability.

As seen in Figure 3.5, ECCO2 is able to reproduce the SSH variability observed from Aviso satellite altimetry data. Figure 3.5c shows the area-averaged SSH signals in the two data sets, and indicates that these two patterns are very similar, with a very high correlation of 0.956 in the low-frequency SSH signals. To calculate eddy kinetic energy (EKE), the following equation is used:

$$EKE = \frac{1}{2}\left(\frac{g}{f}\right)^2\left(\frac{\partial\eta}{\partial x}^2 + \frac{\partial\eta}{\partial y}^2\right), \tag{3.9}$$

where g = gravitational acceleration, f = Coriolis parameter, and $\partial\eta/\partial x$, $\partial\eta/\partial y$ = the zonal and meridional sea surface height gradients, respectively. The EKE patterns seen

in Figures 3.5a and 3.5b are also low-pass filtered to remove a high-frequency variability (periods $<$ 15 months), allowing the interannual variability to be seen. The ECCO2-derived EKE shows very similar patterns to the observed EKE variability from Aviso, with a high correlation of 0.689. For instance, both patterns show elevated signals at the beginning of the time record, and also show elevated EKE in a band starting in the east between 2006-2010 and in the west between 2008-2012. There are also regions of differences, such as in the western region during 2008, where ECCO2 shows much higher EKE than Aviso observations, as well as elevated EKE in the east around 2010. Regardless, the overall spatial and temporal patterns show similar character, and are well correlated. It is noticed that ECCO2 variability tends to have lower levels in the eastern STCC, particularly east of 150°W. Also, while not shown here, it is noted that seasonal EKE variability in ECCO2 has a smaller range than the observed Aviso EKE, even as the interannual EKE strength is approximately equal between the two data sets.

3.4.2 Stratification

Figure 3.6 shows the spatial and temporal patterns of temperature variability in the upper layer, and the relative influence of each of the forcing terms. It can be seen that net heat flux and advective terms all contribute roughly the same to the total response, with each having periods of contributing more significantly to the total response. In an area averaged sense, temperature anomalies are most strongly correlated with horizontal advection (correlation = 0.417). Heat flux anomalies show a low correlation with temperature anomalies (correlation = 0.163). Heat flux anomalies also have a strong negative correlation to the horizontal advection terms (correlation = -0.684). From 2000-2010, this inverse correlation can be seen in the temporal-spatial patterns (Figures 3.6b and 3.6c), where regions of large positive advective flux anomalies correspond to regions of negative heat flux anomalies. A large cooling pattern occurs in the heat flux, with local anomalies exceeding -1° C, coincides with a large warming horizontal temperature flux convergence with local anomalies exceeding 1.5 °C, leading to a net positive temperature anomaly. As the STCC region is an area of net heat

loss (i.e., cooling), it is likely that anomalously warm waters are advected into the region, and then cool as they reside in the STCC area, leading to anomalous net heat loss from the STCC waters.

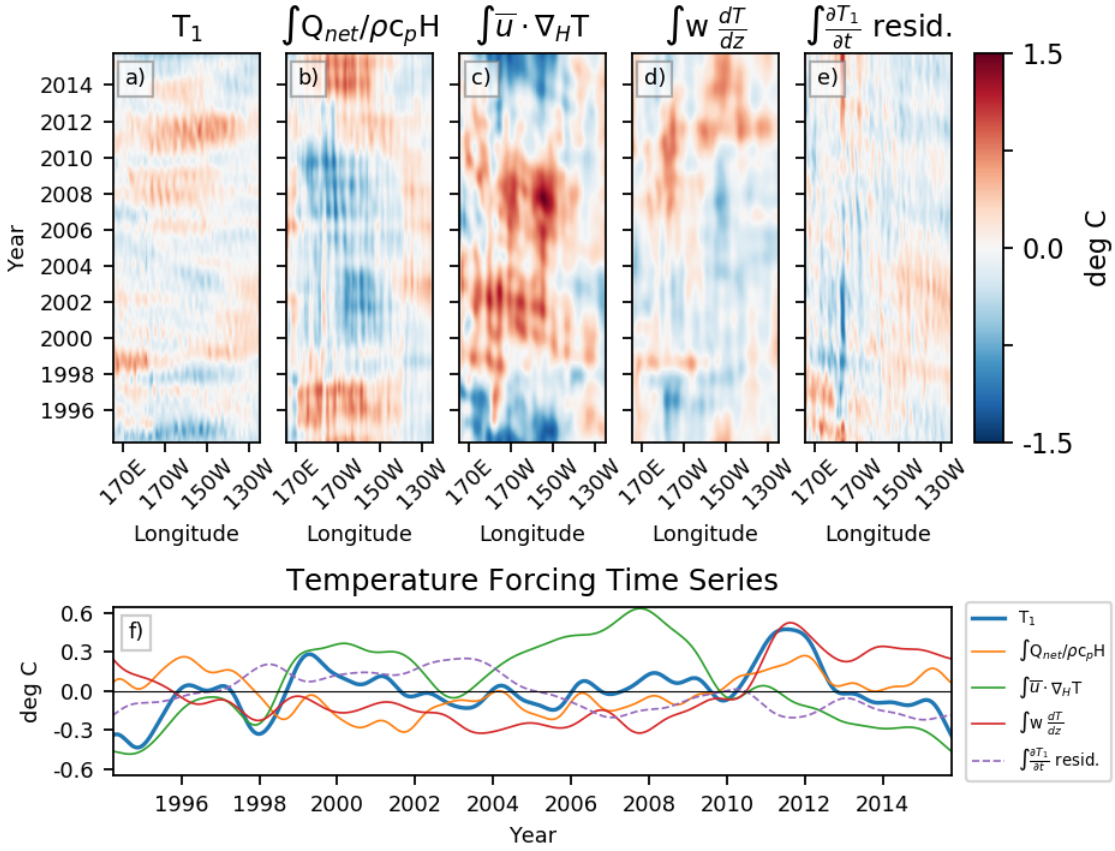

Figure 3.6: The upper row shows Hovmueller diagrams of integrated temperature variability from each of the forcing terms. a) Low-frequency temperature anomalies. b) Temperature anomalies due to net heat flux anomalies. c) Temperature anomalies due to anomalous horizontal temperature flux convergence. d) Temperature anomalies due to vertical temperature flux convergence. e) Diffusive temperature flux convergence, calculated as the residual from the other terms. Bottom row: Time series of area-averaged temperature variability, due to the respective forcing terms (net heat flux, advective temperature flux convergence, diffusive temperature flux convergence.

Similar to the observed temperature anomalies, salinity anomalies seems to be strongly dominated by horizontal advection and freshwater fluxes. These patterns can be seen in Figure 3.7. The largest anomalies are generated by horizontal salinity flux convergence, with

freshwater fluxes also playing a significant role. Horizontal advective flux convergence has the highest correlation (correlation = 0.857), and is responsible for the largest anomalies. Locally, horizontal advective flux anomalies can be as large as ± 0.3 psu, leading to the possibility of significant changes in stratification due to salinity changes. Vertical flux convergence seems to play a smaller, but still significant role for salinity anomalies, and generally works to modulate some of the larger horizontal advective flux convergence anomalies. Fresh water fluxes are weakly correlated to salinity anomalies (correlation = 0.322), but seem to play a significant role in modulating the advective fluxes.

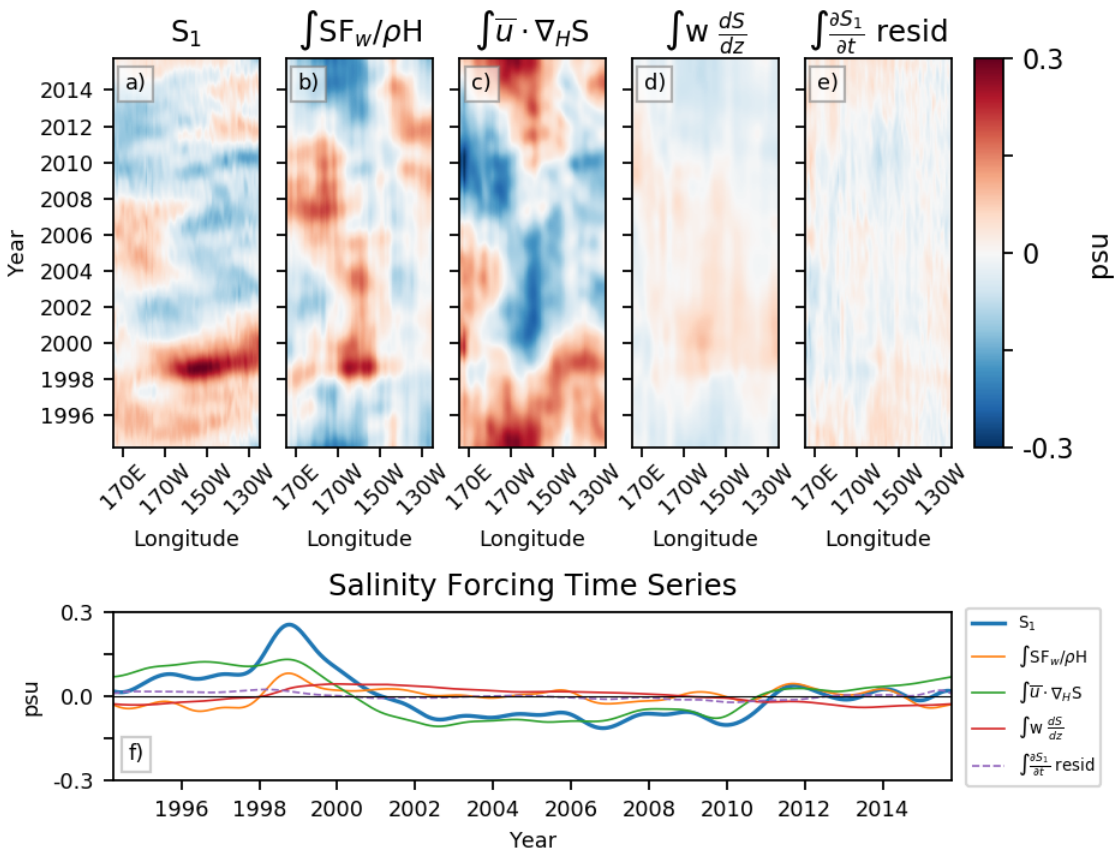

Figure 3.7: The upper row shows Hovmueller diagrams of integrated salinity variability from each of the forcing terms. a) Low-frequency salinity anomalies. b) Salinity anomalies due to net freshwater flux anomalies. c) Salinity anomalies due to anomalous horizontal salinity flux convergence. d) Salinity anomalies due to vertical salinity flux convergence. e) Diffusive salinity flux convergence, calculated as the residual from the other terms. Bottom row: Time series of area-averaged salinity variability, due to the respective forcing terms (net freshwater flux, advective salinity flux convergence, diffusive salinity flux convergence.

Using the results found in Figure 3.6 and Figure 3.7, the impact of the relative forcing terms on stratification in the 2-1/2 layer system can be calculated. As previously described (see Figure 3.2), it is assumed that the most significant variability occurs in the upper layer, and so only changes in this layer are assumed to impact stratification changes. For the purposes of visualization, advective flux convergence of temperature and salinity are combined into a single density flux term. Likewise, the diffusive flux terms are also combined

into a single flux term. The results are presented in Figure 3.8.

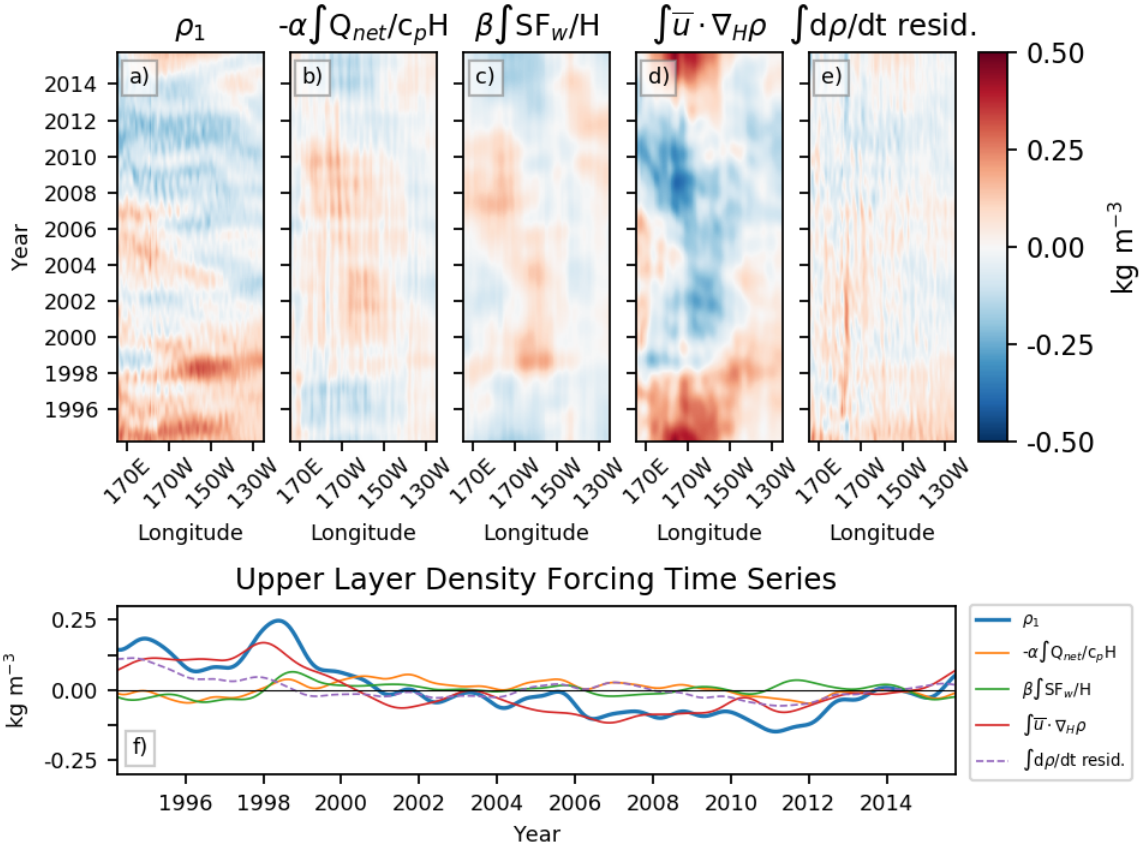

Figure 3.8: The upper row shows Hovmueller diagrams of integrated density variability from each of the forcing terms. a) Low-frequency density anomalies. b) Density anomalies due to net heat flux anomalies. c) Density anomalies due to net freshwater flux anomalies. d) Density anomalies due to anomalous total density flux convergence. e) Density anomalies due to total diffusive flux convergence. Total advective flux convergence is the sum of horizontal temperature and salinity flux convergence and vertical temperature and salinity flux convergence. Diffusive flux convergence is calculated as the residual from the other terms. Bottom row: Time series of area-averaged density variability, due to the respective forcing terms (net heat flux, net freshwater flux, advective density flux convergence, diffusive density flux convergence.

In this figure, it can be seen that advective flux convergence is the strongest driver of upper layer density variability and is most strongly correlated to the density anomaly patterns (area-averaged signal correlation = 0.900). Local advective flux-induced density

anomalies can exceed ± 0.40 kg m^{-3}, leading to significant stratification changes. However, these advective changes are modulated by the heat and fresh water flux terms. Each of these terms is smaller than the total advective flux, with peak anomalies of approximately $\pm$ 0.15 kg m^{-3} for each, but work constructively to offset the most extreme advective flux-induced anomalies. From Figures 3.6f and 3.7f, it can be seen that the low-frequency temperature and salinity changes have different dominant periods of variability, and as such, the combination of the two patterns could alternately exhibit constructive of destructive interference signals. It is noted that the heat flux-induced density anomalies have a high correlation to the freshwater flux-induced density anomalies (correlation = 0.579), and each has a large negative correlation to the advective flux anomalies (correlation = -0.722, -0.673 for heat flux and freshwater flux, respectively). When comparing to Figures 3.6c and 3.7c, we see that the density fluxes are caused by the anomalous advection of warm, fresh water into the region. Increased evaporation of these warmer waters would cause the observed increase patterns seen in Figures 3.6b and 3.7b. It can be interpreted that the anomalously warm waters would lead to an increased heat flux out of the ocean, with evaporative cooling causing a decrease in the temperature of the waters while also increasing the salinity in the region.

3.4.3 Shear

Similar to stratification, variability in shear is assumed to be dominated by changes in the upper layer. For this reason, all analysis of variability in shear will be restricted to changes in the upper layer (U_1). However, as can be seen in Figure 3.2, the lower layer zonal velocity variability plays a more significant role to total shear variability, and neglecting changes in this layer could lead to larger errors. This will be addressed more directly in the Discussion section. To assess the impact of each of the forcing terms in the temperature and salinity budgets, a thermal wind balance is assumed, in which the meridional gradient of density can be related to vertical shear of zonal velocity. Referring back to Eq. 3.7, assuming a linear density equation, and integrating through the layer, the changes in zonal velocity can be calculated by the following:

$$U_1 = \overline{U_1} + \frac{gH_1}{\rho f}\frac{\partial}{\partial y}\Bigg[- \alpha \int \left(\frac{Q_{net}}{c_p \rho H} + \overline{u} \cdot \nabla_H T + (\text{Diff. T}) \right) \partial t + \beta \int \left(\frac{SF_w}{\rho H} + \overline{u} \cdot \nabla_H S + (\text{Diff.S}) \right) \partial t \Bigg], \quad (3.10)$$

where U_1 = upper layer zonal velocity, $\overline{U_1}$ = mean upper layer zonal velocity, g = gravitational acceleration, H_1 = upper layer thickness, f = Coriolis parameter, Q_{net} = net heat flux, c_p = specific heat of seawater, ρ = reference density, $\overline{u}$ = three-dimensional velocity vector, T = upper layer temperature, S = upper layer salinity, and (Diff.) = diffusive terms. This equation is constructed by integrating the temperature and salinity budget equations and taking the meridional gradient. From this, each term in the temperature and salinity budgets can be evaluated for the relative contribution to the total change in the upper layer zonal velocity.

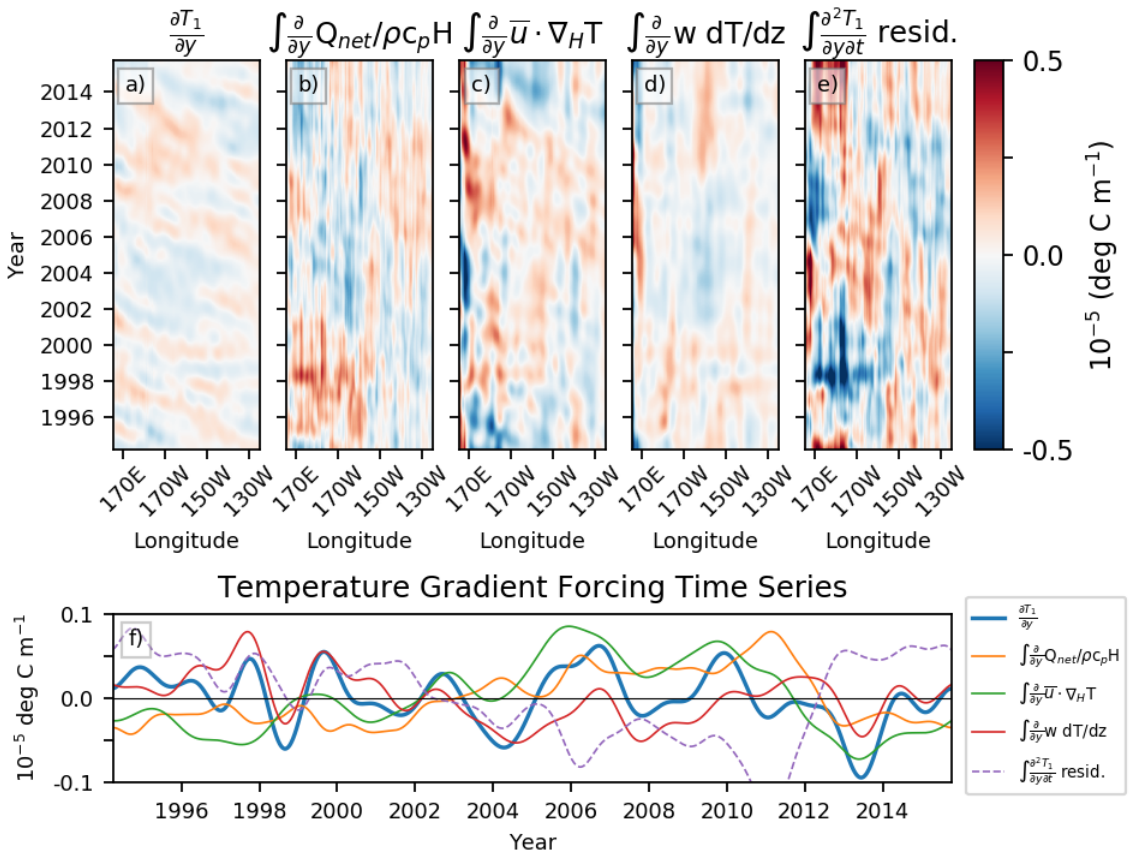

Figure 3.9: The upper row shows Hovmueller diagrams of integrated meridional temperature gradient variability from each of the forcing terms. a) Low-frequency temperature gradient anomalies. b) Temperature gradient anomalies due to the gradient of net heat flux anomalies. c) Temperature gradient anomalies due to the gradient of anomalous horizontal temperature flux convergence. d) Temperature anomalies due to the gradient of vertical temperature flux convergence. e) Gradient of diffusive temperature flux convergence, calculated as the residual from the other terms. Bottom row: Time series of area-averaged temperature gradient variability, due to the respective forcing terms (gradient of net heat flux, advective temperature flux convergence, diffusive temperature flux convergence.

Figure 3.9 shows the variability in the meridional temperature gradient in the STCC. Temperature gradient variability is impacted by all terms in the budget equation, with no single term dominating throughout the time series. Horizontal and vertical advective flux terms have the highest correlation with meridional temperature gradient (correlation = 0.466, 0.529, respectively). While local meridional temperature gradient anomalies can be as large

as $\pm$ 0.15 x 10^{-5} °C m^{-1}, local anomalies from the forcing terms can be more than double that. The competing and compensating interactions work to modulate the temperature gradient variability.

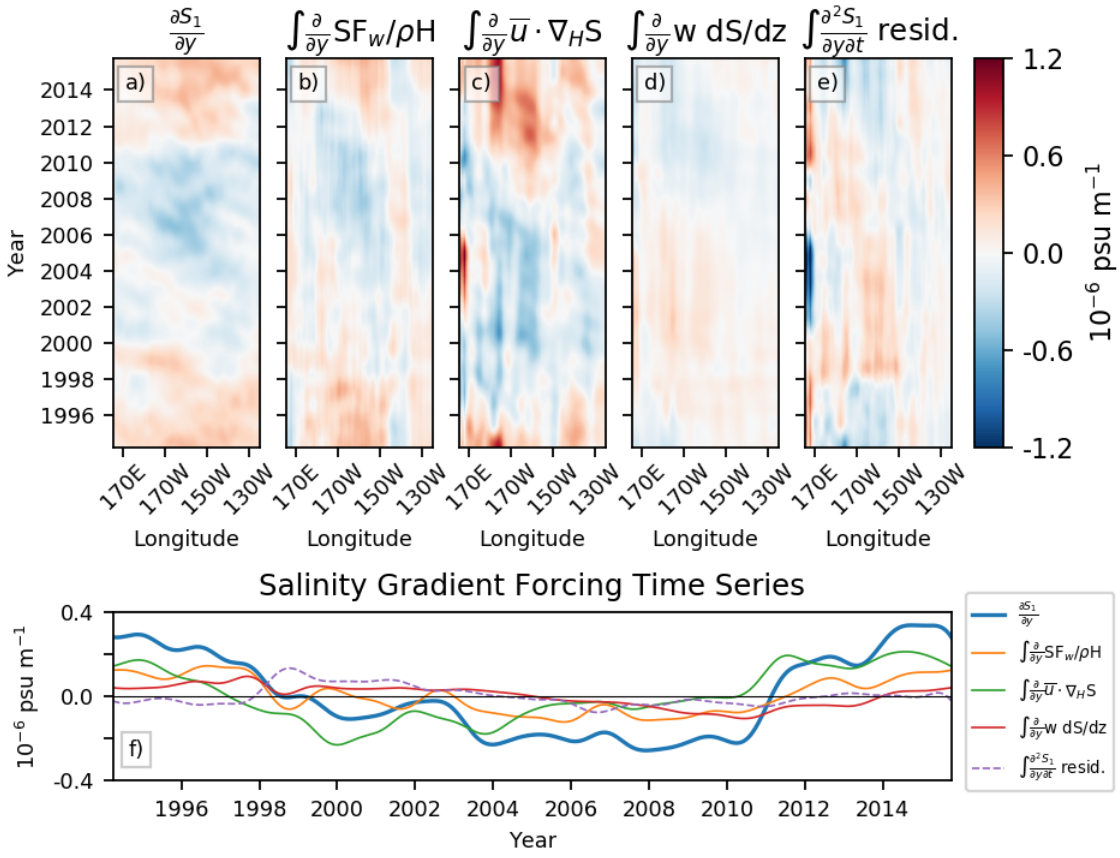

Figure 3.10: The upper row shows Hovmueller diagrams of integrated meridional salinity gradient variability from each of the forcing terms. a) Low-frequency salinity anomalies. b) Salinity gradient anomalies due to the gradient of net freshwater flux anomalies. c) Salinity anomalies due to the gradient of anomalous horizontal salinity flux convergence. d) Salinity anomalies due to the gradient of vertical salinity flux convergence. e) Gradient of diffusive salinity flux convergence, calculated as the residual from the other terms. Bottom row: Time series of area-averaged salinity gradient variability, due to the respective forcing terms (gradient of net freshwater flux, advective salinity flux convergence, diffusive salinity flux convergence.

Variability in meridional salinity gradients, as shown in Figure 3.10, is dominated by changes in the freshwater flux forcing and horizontal advection terms, and are most strongly

correlated, with correlations of 0.930 and 0.725 for freshwater flux gradients and horizontal advective flux convergence gradients, respectively. Advective flux gradients are the largest, and can exceed 1.0 x 10^{-6} psu m^{-1} locally, and 0.2 x 10^{-6} psu m^{-1} on average. Area-averaged freshwater flux gradients have typical magnitudes close to 0.15 x 10^{-6} psu m^{-1}. Fresh water flux and horizontal advective forcings have constructive interference patterns, leading to larger salinity gradient anomalies.

Using the results from the gradients of the temperature and salinity budgets, shown in Figures 3.9 and 3.10, density gradient variability can be reconstructed, and by applying the thermal wind balance, as shown in Eq. 3.10, the upper layer zonal velocity forcing can be reconstructed. This is shown in Figure 3.11. Overall, area-averaged advective flux-induced anomalies are the most correlated to area-averaged zonal velocity anomalies (correlation = 0.927), and have the largest magnitudes, with local anomalies exceeding 2 cm s^{-1}. Heat flux and fresh water flux gradients exhibit similar patterns and generally work constructively to generate zonal velocity anomalies. Locally, the zonal velocity anomalies from these two terms can exceed 1 cm s^{-1}.

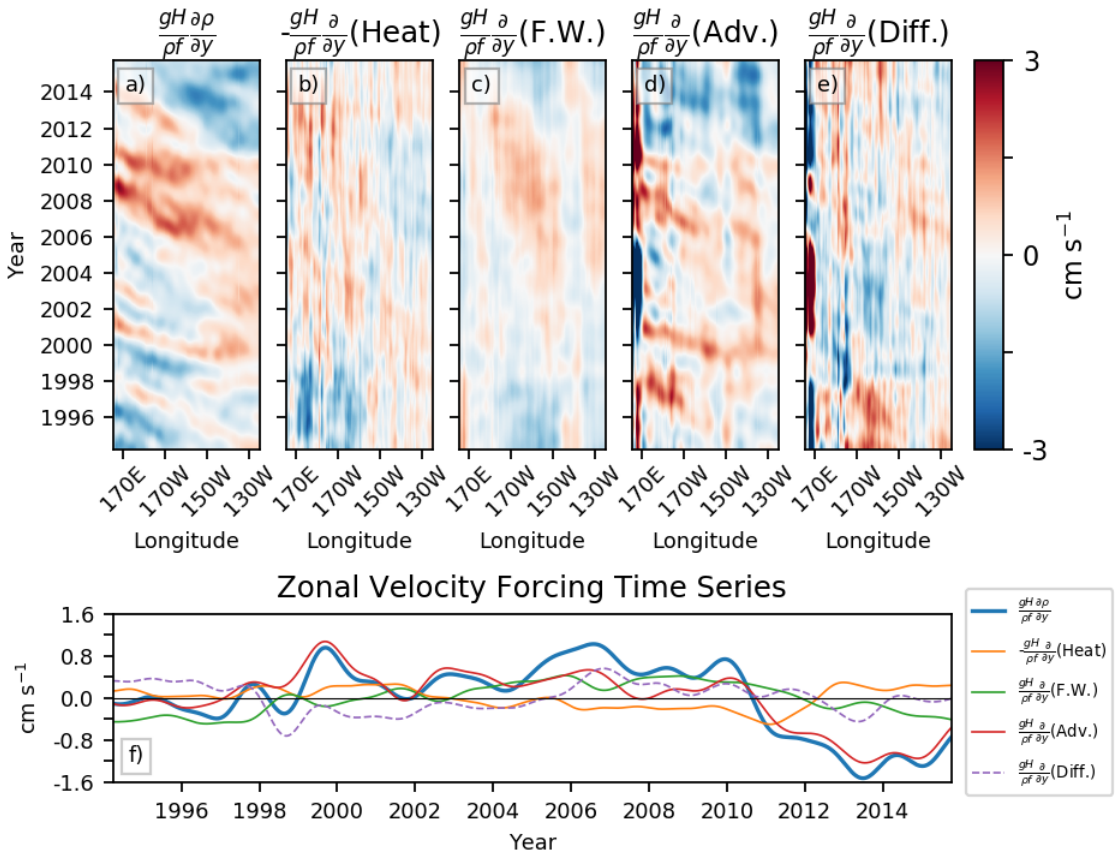

Figure 3.11: The upper row shows Hovmueller diagrams of zonal velocity variability, as derived by assuming a thermal wind balance on meridional density gradients, from each of the forcing terms. a) Low-frequency zonal velocity anomalies. b) Zonal velocity gradient anomalies due to the gradient of net heat flux anomalies. c) Zonal velocity gradient anomalies due to the gradient of net freshwater flux anomalies. d) Zonal velocity anomalies due to the gradient of anomalous total flux convergence. e) Zonal velocity anomalies due to the gradient of total diffusive flux convergence. Total advective flux convergence is the sum of horizontal temperature and salinity flux convergence and vertical temperature and salinity flux convergence. Diffusive flux convergence is calculated as the residual from the other terms. Bottom row: Time series of area-averaged zonal velocity gradient variability, due to the respective forcing terms (gradient of net heat flux, net freshwater flux, advective flux convergence, diffusive flux convergence.

The contribution of the advective terms for temperature and salinity are found to be similar in magnitude, with salinity playing a slight larger contributor. Peak magnitude

anomaly contributions from the salinity advective flux are 0.84 cm s^{-1}, as compared to 0.56 cm s^{-1} for temperature advective fluxes. When compared to the total advective flux terms, salinity is more highly correlated (correlation = 0.908) than temperature (correlation = 0.742).

3.4.4 Baroclinic Growth Rate

Using a similar linearization to the baroclinic growth rate (BCR) as Travis and Qiu (2017), the contributions of each forcing to variability in the baroclinic growth rate can be directly estimated. In the linearization, the following reference parameters are used: $2\pi/l$ = 250 km, H1 = 240 m, H2 = 300 m, u_2 = -0.8 cm s^{-1}, ρ_2 = 1026.35 kg m^{-3}, ρ_3 = 1027.5 kg m^{-3}, σ_0 = 25°S. For more details on how BCR is found, refer to the Appendix. Using these parameters, mean layer shear and layer stratification values are found, and can be used to calculate a mean BCR. These mean values are: U_{z0} = 3.21 cm s^{-1}, ρ_{z0} = 1.37 kg m^{-3}, and ω_0 = 11.8 x 10^{-3} day^{-1}. A Taylor series expansion about these reference values can be given as follows:

$$\omega = \omega_0\Big(1 + \gamma(U_z - U_{z0}) + \zeta(\rho_z - \rho_{z0})\Big) \tag{3.11}$$

From this linearization, the appropriate scaling parameters are γ = 0.343 s cm^{-1} for the shear parameter and ζ = -0.978 m^3 kg for the stratification parameter. The combined use of all of these factors, as well as the results found in Figures 3.8 and 3.11 allow us to identify the contributions to variability from each of the terms in the budget equations. The results of these contributions can be seen in Figure 3.12.

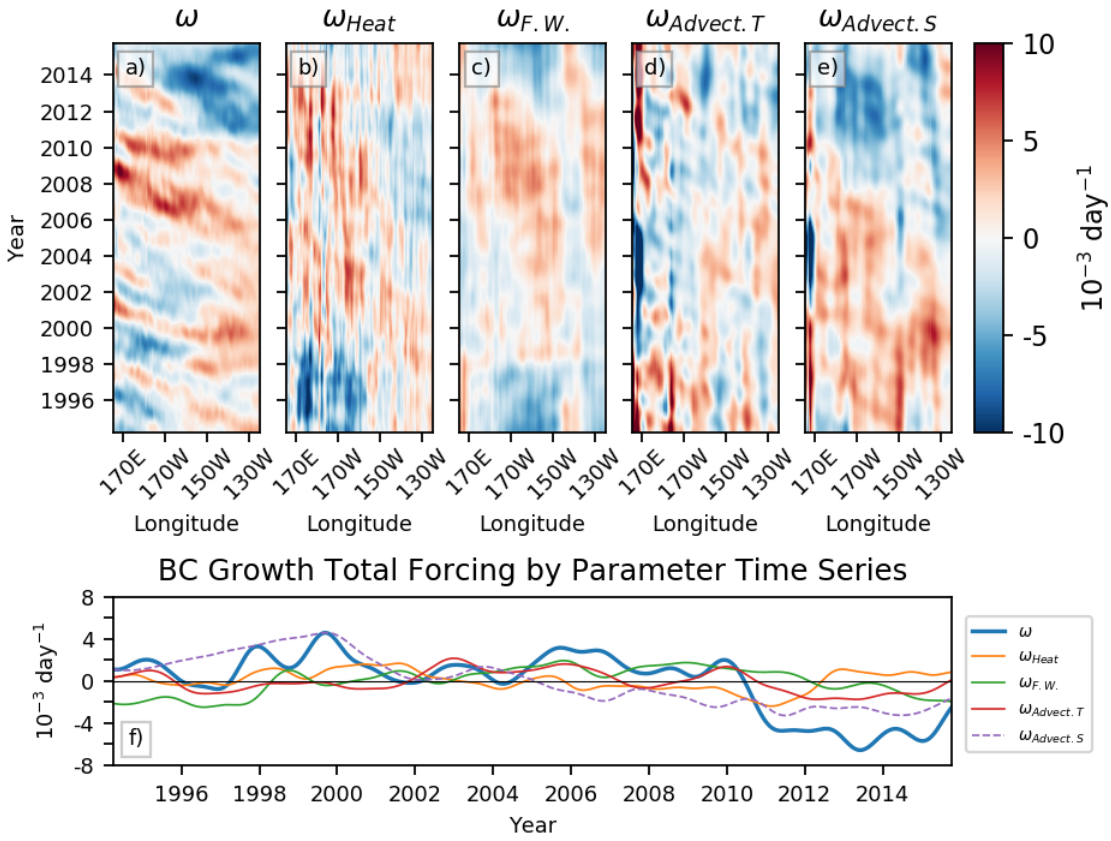

Figure 3.12: The upper row shows Hovmueller diagrams of linearized baroclinic growth rate(BCR) variability, as derived by linearization about mean upper layer shear and stratification, from each of the forcing terms. a) Low-frequency BCR. b) BCR anomalies due to heat flux forcing. c) BCR anomalies due to the net freshwater flux forcing. d) BCR anomalies due to total advective flux convergence. e) BCR anomalies due to diffusive flux convergence. Total advective flux convergence is the sum of horizontal temperature and salinity flux convergence and vertical temperature and salinity flux convergence. Diffusive flux convergence is calculated as the residual from the other terms. Bottom row: Time series of area-averaged BCR variability, due to the respective forcing terms (net heat flux, net freshwater flux, advective flux convergence, diffusive flux convergence).

From this figure, we can identify the advective terms to be the most dominant, with temperature and salinity advection being approximately equally significant. However, all terms have significant contributions, at different times, are the most significant contributors, and can work constructively or destructively with each other to contribute to the total

baroclinic growth rate variability. In an area-averaged sense, total BCR anomalies can reach a maximum magnitude of approximately 6.45 x 10^{-3} day^{-1}. For comparison, heat forcing can reach a maximum of 2.41 x 10^{-3} day^{-1}, freshwater forcing can reach a maximum of 2.51 x 10^{-3} day^{-1}, and advection of temperature and salinity gradient fluxes can reach a maximum of 2.17 x 10^{-3} day^{-1} and 4.63 x 10^{-3} day^{-1}, respectively.

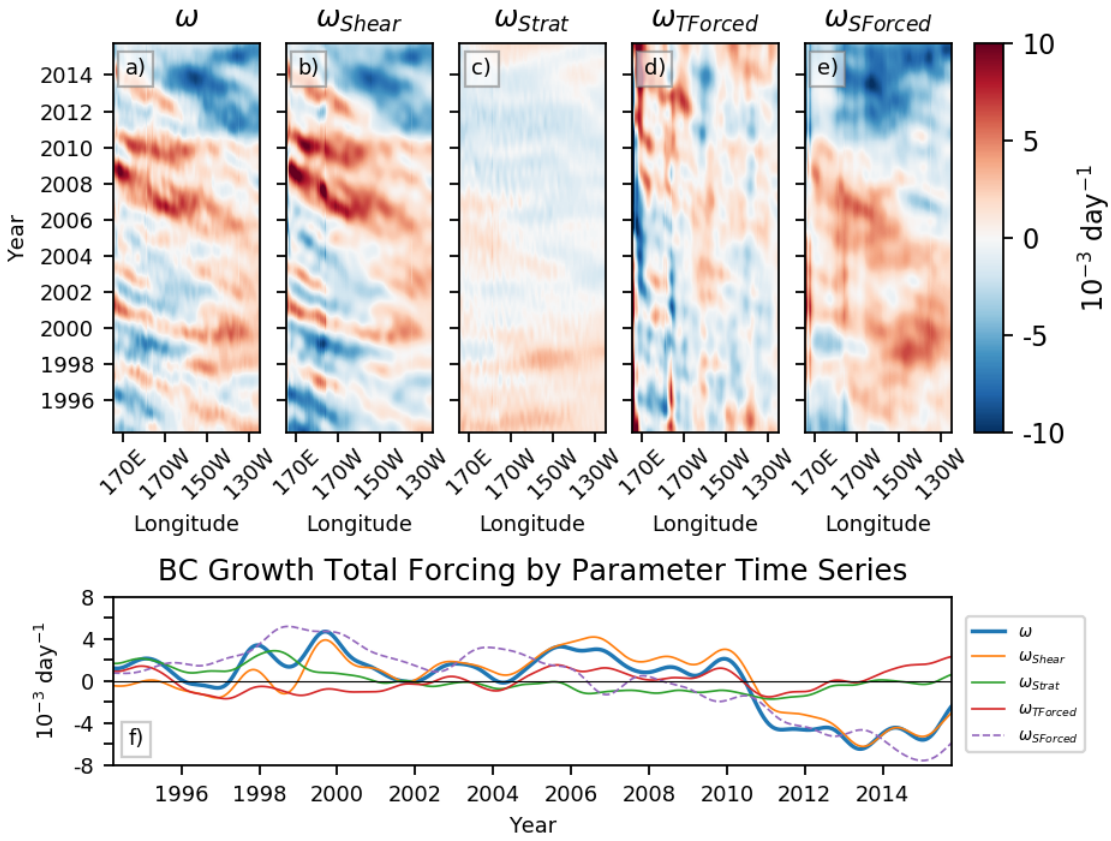

Figure 3.13: The upper row shows Hovmueller diagrams of linearized baroclinic growth rate(BCR) variability, as derived by linearization about mean upper layer shear and stratification, from each of the forcing terms. a) Low-frequency BCR. b) BCR anomalies due to shear variability. c) BCR anomalies due to stratification variability. d) BCR anomalies due to temperature variability. e) BCR anomalies due to salinity variability. For temperature and salinity-induced variability, the terms represent the change due to total changes in the respective parameter; i.e., total temperature-induced BCR variability is the temperature-induced shear and stratification variability. Bottom row: Time series of area-averaged BCR variability, due to the respective forcing terms (shear, stratification, temperature, and salinity).

To get another perspective on the relative contributions on the degree on instability in the STCC region, Figure 3.13 shows the contributions to total BCR variability from shear and stratification changes, as calculated from changes in the upper layer (Figs. 3.13b and Fig. 3.13c), and from temperature and salinity changes (Figs. 3.13d and Fig. 3.13e). In these

Figures, the parameters are the summation of all relevant terms. For instance, Figure 3.13b shows the total variability due to changes in shear, which is the summation of the changes in the zonal velocity due to changes in the meridional gradient of net heat flux, net freshwater flux, and advective and diffusive flux convergences. Likewise, Figure 3.13d shows the changes due to temperature variability, which is the summation of changes in stratification due to changes in net heat flux and advective and diffusive temperature gradient flux convergence, and in shear due to changes in the gradient of those same terms.

Shear is found to be the larger contributor to total BCR variability, and is most strongly correlated to the total variability (correlation = 0.923). Area-averaged shear-induced changes have a maximum magnitude of 6.21 x 10^{-3} day^{-1}, while stratification-induced changes have a maximum of 2.86 x 10^{-3} day^{-1}; about 40% of the shear-induced changes. These results are roughly in agreement with the findings of Travis and Qiu (2017), which found that shear changes accounted for approximately 2/3 of total variability and stratification changes accounted for approximately 1/3 of total variability. A comparison of the total temperature-forced and salinity-forced variability shows maximum area-averaged anomaly magnitudes of 2.30 x 10^{-3} day^{-1} and 7.55 x 10^{-3} day^{-1}, respectively. Total salinity variability shows a higher correlation to BCR variability (correlation = 0.832) than total temperature variability to BCR variability (correlation = -0.010).

Table 3.1: Overview of Temperature and Salinity Budgets Impacts on Shear and Stratification

Parameters	**Heat**	**Moist**	**u $\cdot\nabla$T**	**u $\cdot\nabla$S**	**Diff.T**	**Diff.S**
Max Anomalies: Found as the absolute value of maximum area-averaged anomaly magnitude						
T (°C)	0.32	–	0.64	–	0.25	–
S (10^{-2} psu)	–	8.08	–	13.0	–	2.32
dTdy (10^{-7} °C m^{-1})	7.86	–	8.50	–	13.9	–
dSdy (10^{-7} psu m^{-1})	–	1.43	–	2.32	–	1.32
Shear (cm s^{-1})	0.50	0.49	0.56	0.84	0.40	0.47
Strat. (kg m^{-3})	5.51	6.45	10.6	10.3	2.67	2.43
BC (10^{-3} day^{-1})	2.41	2.51	2.17	4.63	1.71	1.62
Correlation: Found as the correlation between the area-averaged signals						
Shear	-0.345	0.540	0.660	0.547	-0.424	0.143
Stratification	0.071	-0.041	0.654	0.796	-0.611	0.547
Baroclinic Growth Rate	0.099	0.233	0.407	0.580	-0.355	0.353
Max. Anomalies are found as the absolute value of maximum area-averaged anomaly magnitude.						

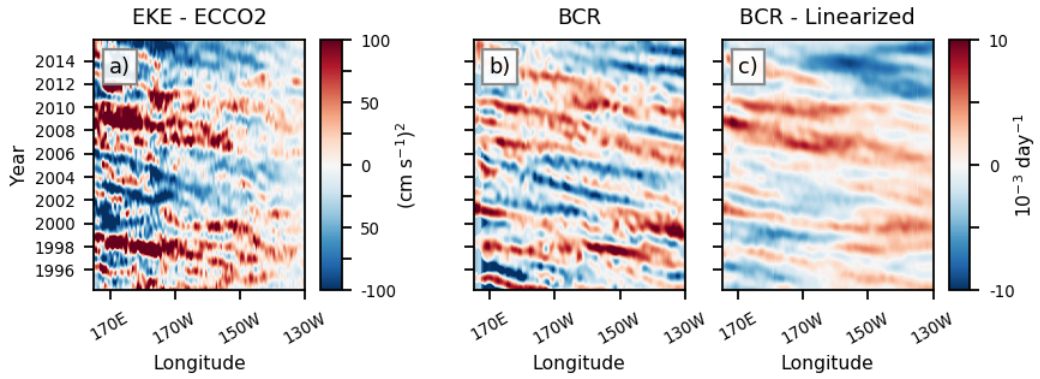

Figure 3.14: Comparison between eddy kinetic energy (EKE) and baroclinic growth rate (BCR). a) EKE derived from ECCO2 geostrophic velocity anomalies. b) BCR anomalies, fully non-linear, calculated using total variations in shear, stratification, and layer thicknesses. c) Linearized BCR, calculated through a linearized parameterization about the mean shear and stratification state, allowing only variations in the upper layer density and zonal velocity.

Lastly, a comparison between the ECCO2 EKE variability and BCR can illustrate how successful this linearization can be at describing the relative importance of each forcing on changing eddy activity. In Figure 3.14, variability in EKE in the ECCO2 model output, the fully non-linear BCR, and the linearized BCR are shown. The fully non-linear BCR calculation allows for variation in upper and lower layer density, as well as variability in layer thickness. When comparing the non-linear BCR (Figure 3.14b) to the linear BCR (Figure 3.14c), we see that the overall patterns between the two are very similar and highly correlated (correlation = 0.666). The non-linear BCR has more extreme local highs and lows than the linear BCR, but overall, the patterns are well matched. In the most extreme cases, linear BCR can have errors as large as ± 3 x 10^{-3} day^{-1}, roughly 30% of the mean baroclinic growth rate. However, these extreme errors are typically more of a scaling issue. This can be seen clearly during the early period of the time record, from 1996-2000, when the linearized BCR underestimates the full range of BCR variability, and misses some of the most extreme EKE anomalies. Even still, both the non-linear BCR and linear BCR are well correlated to EKE variability (correlation = 0.748 for non-linear BCR, correlation = 0.566 for linear BCR), and capture the spatial and temporal patterns seen in EKE variability. In regards to evaluating the relative importance of each of the forcing mechanisms, as seen in the temperature and salinity budgets, the linearization of BCR can capture the most significant variability, and can be a useful tool.

3.5 Basin scale connections

A large number of previous studies have looked a basin-wide trends in different parameters. For instance, Volkov et al. (2017) looked at decade-long warming in the South Pacific, while Zhang and Qu (2014) and Hasson et al. (2013) looked at salinity variability across the South Pacific Gyre. A number of studies have investigated decadal sea surface height variability (Bowen et al. 2005; Qiu and Chen 2006; Roemmich et al. 2007, 2016). For a majority of these studies, it was found that a large degree of the variability could be connected to changes in the Interdecadal Pacific Oscillation index (Henley et al. 2015; ?). A more recent study of the

southeastern branch of the STCC by Rieck et al. (2018) concluded that local atmospheric wind forcing, through variability in Ekman pumping, was strongly correlated to IPO, while density anomalies propagating into the region from further east make up a smaller percentage of the total variability, are are not associated with the IPO.

To assess any larger scale connections to basin scale climatic patterns, an EOF analysis of the major driving forces in the temperature and heat budgets are performed. An EOF analysis is performed on low-pass filtered (frequency < 1 yr^{-1}) net surface heat flux, net surface moisture flux, zonal velocity, and wind stress curl. Zonal velocity is assessed to look at the changing strength of horizontal advection, which is dominated by zonal flows. Wind stress curl is assessed to look at the changing strength of local Ekman pumping, which is a dominant factor in vertical advection. The results are shown in Figure 3.15.

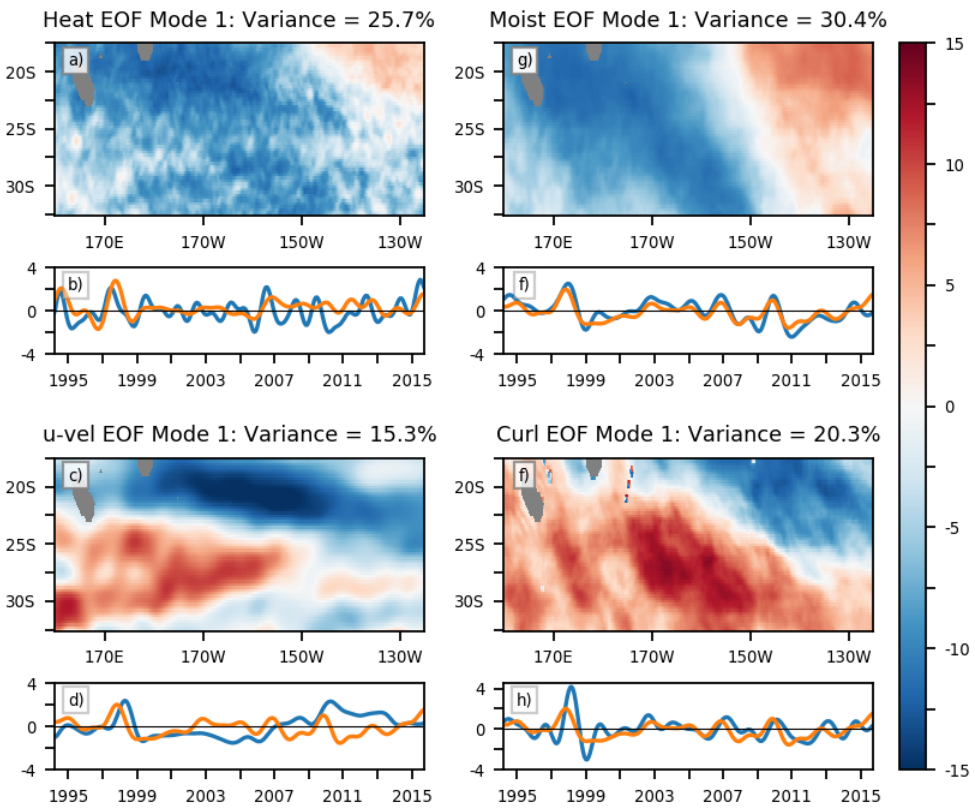

Figure 3.15: First EOF mode of driving terms in budget equations: net surface heat flux, net moisture flux, zonal velocity, and wind stress curl. EOF modes are given in figures a), b), e), and f). Corresponding principal component time series of the EOF modes are given in figures c), d), g), and h). The time series is given as the blue line, while a low-pass smoothed (< 1 yr^{-1}) IPO time series is given in orange. a) EOF-1 of net surface heat flux. b) Principal component time series of heat flux EOF mode 1. c) EOF-1 of zonal velocity of the averaged upper 200 m. d) Principal component time series of upper 200 m zonal velocity. e) EOF-1 of net moisture flux. f) Principal component time series of net moisture flux. g) EOF-1 of wind stress curl. h) Principal component time series of wind stress curl.

The EOF analysis is done in the region of 17.5°S-32.5°S, 160°E-125°W, which is a region slightly extended beyond the band of heightened eddy activity shown in the previous section. This box size was chosen to isolate signal variability to the regional analysis of interest. In the principal component time series of each of the modes (Figures 3.15b, 3.15d, 3.15f, 3.15h), the low-pass smoothed (< 15 months^{-1}) IPO index is shown. The first EOF mode is shown

in Figure 3.15, as this mode shows the most variance. All of the terms have more than twice as much variance in the first mode than any other mode, except for zonal velocity, which has 15.3% of the variance as compared to 14.3% of the variance in the second mode.

Generally, all of the modes show a dipole pattern, dividing the signal into a northeast versus southwest pattern. For example, net heat flux EOF-1 (Figure 3.15a) shows a broad negative pattern, roughly extending from 20°S, 175°E to 30°S, 150°W, and a positive pattern to the northeast. Likewise, net moisture flux EOF-1 has a similar spatial pattern. These patterns would be consistent with patterns of evaporative cooling, in which regions of heat loss correspond to regions of moisture loss.

Except of zonal velocity, there is strong correlation in the principal component time series for all of the signals with the IPO. Net moisture flux shows the strongest agreement with IPO, with a correlation of 0.84 at a 1-month lag of moisture flux leading IPO. Heat flux is correlated at 0.60 at a 5-month lead of heat flux to IPO. Wind stress curl lags IPO by 3 months, and has a correlation of 0.72. Zonal velocity has the lowest correlation to IPO, and has a correlation of 0.16 at a 5-month-lag to IPO.

The diagonal, northwest-to-southeast band found in each of the EOF modes is a pattern similar to that of the South Pacific Convergence Zone (SPCZ), an atmospheric pattern of low-level wind convergence with associated increased cloudiness and precipitation (Vincent 1994). The SPCZ has a latitudinal tilt, and can span the tropics and subtropics (Widlansky et al. 2011). The precipitation patterns associated with the SPCZ strongly influence the ocean salinity and stratification (Widlansky et al. 2011). The SPCZ has strong influences on ocean circulation (Ganachaud et al. 2014) and oceanic patterns, including ENSO (McGregor et al. 2012).

The position of the SPCZ has been shown to alter in relation to ENSO and IPO. Folland (2002) examined this variability, and found that the SPCZ location and orientation would vary based upon these two patterns. They found that the mean SPCZ position moves north and has a more zonal orientation during a times of positive IPO and negative SOI, while it moves south and has a more diagonal orientation during time of negative IPO and positive

SOI. Due to the diagonal nature of the SPCZ, a north/south transition also results in an eastward/westward movement of the band for any given latitude. During these times, the SPCZ mean position would coincide with the eastern branch of the STCC, and correspond well with the diagonal bands band seen in the EOF-1 spatial patterns for net moisture flux. Additionally, Kidwell et al. (2016) examined variability in the strength as well as position of the SPCZ on interdecadal timescales, and also found a strong relationship with ENSO-related indices. This connection can be seen in Figure 3.16.

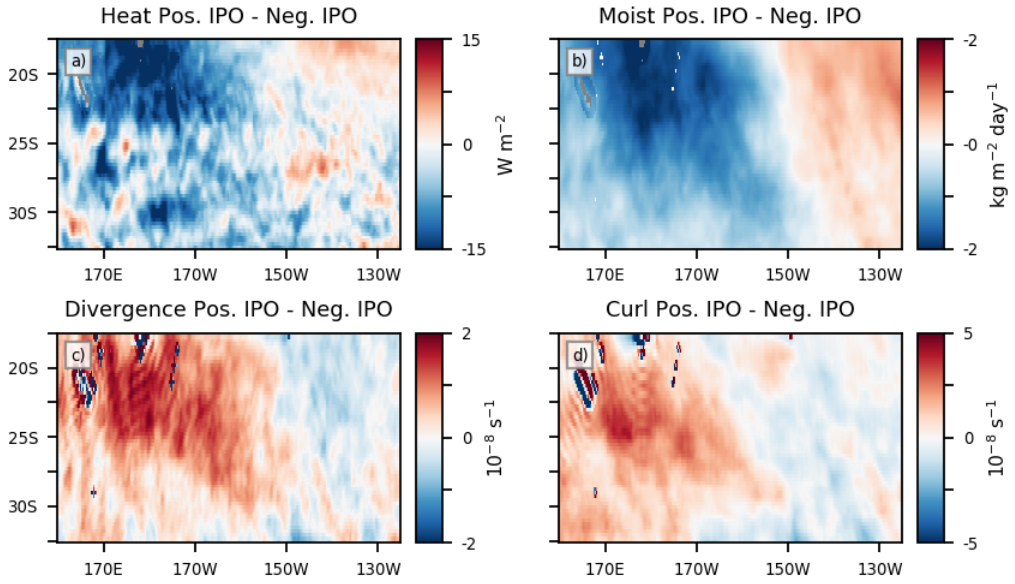

Figure 3.16: Difference in forcings during positive versus negative IPO periods. a) Change in net surface heat flux. Positive heat flux is heat into the ocean, leading to increasing temperature. b) Change in net surface moisture flux. Positive moisture flux is moisture into the ocean, leading to decreasing salinity. c) Change in surface wind divergence/convergence. Positive values indicate wind divergence while negative values indicate convergence. d) Change in surface wind stress curl.

In Figure 3.16, the similarity in patterns between wind convergence and the other atmospheric forcing terms can be seen. During a positive IPO phase, the SPCZ would move north and east, leading to decreased wind convergence (increased divergence) across the STCC band. This corresponds to decreased moisture flux into the STCC band. It can be

conjectured that the change in heat flux could be related to changing patterns associated with cloudiness and evaporative cooling.

3.6 Discussion

Eddy activity in the South Pacific Sub-tropical Counter-current has been previously understood to be forced by baroclinic instabilities. (Travis and Qiu 2017). Through the use of temperature and salinity budgets in the upper ocean, the forcing factors on the ocean, leading to changes in eddy activity, have been explored. A summary of these results is shown in Table 3.1. The advection of temperature and salinity gradients have been shown to have the most significant impact on total baroclinic growth rate (BCR) variability, with the advection of salinity gradients being more impactful and correlated than temperature gradients. Similarly, surface forcing on temperature via net heat flux is less correlated overall than surface forcing on salinity via net freshwater flux. In combination, large scale changes in salinity fields are much more impactful and well correlated to BCR changes (correlation $= 0.828$), while changes in temperature are more localized, and help to modulate large scale salinity-induced BCR changes. This is in contrast with seasonal changes in the region, in which temperature-induced variability dominates, and is driven by changes in heat flux.

Variance in the forcings in the STCC region are shown to be connected to the Interdecadal Pacific Oscillation (IPO), with strong dipole patterns across the STCC band. Surface forcings are strongly impacted by the position of the South Pacific Convergence Zone (SPCZ), which alters wind patterns and surface heat and moisture fluxes. The position of the SPCZ has previously been shown to be connected to ENSO variability, as can be shown through IPO changes (Folland 2002; Kidwell et al. 2016). As the position of the SPCZ moves north(south), heat flux out of the ocean increases(decreases) and moisture flux into the ocean decreases(increases). These anomalies in the forcings are integrated with time, leading to the observed variability seen in Figures 3.6 and 3.7.

While the linearized method for studying eddy variability presented here is able to explain a significant amounts of the changes observed, a number of factors have for now

been unexplored. For instance, lower-layer variability was assumed to be insignificant, and therefore, assumed to be constant; however, this is not necessarily true. As seen in Figure 3.2, the lower layer variability is smaller than the upper layer, but is certainly still of sufficient magnitude to have a discernible impact. This is particularly true for the lower layer zonal velocity. Decadal South Pacific Gyre spin-up could increase gyre circulation (Roemmich et al. 2007, 2016; Zhang and Qu 2015; Zilberman et al. 2014), leading to a strengthening of the South Equatorial Current, which is partially contained within our linearized lower-layer state. This spin-up has been suggested to be related to changes in the Southern Annual Mode (SAM), and variations associated with this would have a lagged response as anomalies propagate into the region. Long term trends in the ocean state, such as the decade-long warming described in Volkov et al. (2017), would push isopycnals deeper, also leading to changes in the lower layer. Lastly, topographic impacts have not been accounted for at all. The STCC region is dotted with many high seamounts, providing localized points of flow disturbance and variability. In the western part of the STCC band, the Kermadec ridge provides a significant disruption to the idealized flow patterns. Lou et al. (2019) describe that the Kermadec ridge can trap Rossby waves, and that these topographically trapped nonlinear Rossby waves can act to low-pass filter signals propagating into the region, leading to a more pronounced IPO pattern.

Additionally, this study has only looked at the impacts of forcings on the state of the ocean in the STCC region, and how this relates to the degree of instability leading to mesoscale eddy activity. Future work could explore any potential feedbacks of the eddies onto the mean state of the ocean. Mass transport by eddies (Zhang et al. 2014) can advect anomalous waters, and could smooth density gradients. Eddy fluxes have also been shown in other areas to drive sea surface height variability Qiu et al. (2015). Beyond the observed variability and the direct forcings on the ocean states, understanding the feedbacks of the eddies back to the larger-scale systems would enhance our understanding of circulation in the region.

CHAPTER 4
SEASONAL REVERSAL OF THE NEAR-SURFACE CHLOROPHYLL RESPONSE TO THE PRESENCE OF MESOSCALE EDDIES IN THE SOUTH PACIFIC SUBTROPICAL COUNTER-CURRENT

This work also appears as: Travis, S. and B. Qiu, 2020: Seasonal Reversal of the Near-Surface Chlorophyll Response to the Presence of Mesoscale Eddies in the South Pacific Subtropical Counter-Current. J. Geophys. Res. Ocean., https://doi.org/10.1029/2019JC015752

Abstract

Mesoscale eddies have been shown to have significant effects on biogeochemical cycles, as observed in local levels of near-surface chlorophyll. There are many regional differences in the expected response of near-surface chlorophyll to the presence of eddies, caused by differences in the driving mechanisms. However, in many high eddy-activity areas, previous studies found low correlation and an inconsistent chlorophyll anomaly response to the presence of eddies. One such area is in the South Pacific Subtropical Counter-current. Using GlobColour ocean color data and Aviso altimetry data, an investigation of the area found that a seasonal reversal occurs in the character of the chlorophyll anomaly within eddies (reversal from positive to negative, and vice versa). The cause of this reversal is inferred to be a seasonally-changing limiting factor within the region. Argo float profiles co-located inside and outside of eddies are used to show the coincidence of chlorophyll anomalies with seasonally changing mixed layer depths and the ability of the eddies to access deep nutrient pools. Observations of other mechanisms, such as eddy stirring or eddy-Ekman pumping, are found to be seasonally less important than the mixed layer depth change induced nutrient flux. Additionally, metrics are developed to globally identify oceanic regions in which such seasonal reversals in chlorophyll anomalies could occur.

4.1 Introduction

Primary production in the ocean can be strongly affected by mesoscale eddies (Chelton et al. 2011; Gaube et al. 2014; Klein and Lapeyre 2009; McGillicuddy 2016), which can trap and transport waters, advect water properties and nutrients across gradients, and generate vertical movements of waters and nutrients. Implications for the local influence of eddies on biological activity are diverse. Local primary production can effect net carbon flux to the deep ocean (Guidi et al. 2012), and increased productivity in a region can increase biological abundance at higher trophic levels (Lavelle and Mohn 2010; Morato et al. 2009; Godø et al. 2012). Eddies have been shown to trap planktonic communities over multiple generations (Condie and Condie 2016), while Shulzitski et al. (2016) found that larval coral fish communities entrained within some eddies have higher survivability to settlement on coral reefs. Cyclonic eddies have even been shown to be a preferred foraging habitat for Kerguelen elephant seals in the Polar Frontal Zone of the Southern Ocean (Bailleul et al. 2010). Because of this wide range of possible physical-biological interactions, an understanding of the driving mechanisms and the subsequent biological responses is crucial.

A useful proxy of phytoplankton biomass is the near-surface chlorophyll signal, for which we have an increasingly robust data record through ocean color satellite programs such as SeaWifs and MODIS/Aqua, among others. The mean near-surface chlorophyll concentrations can vary by orders of magnitude, and are not necessarily associated with areas of strong eddy activity. However, as has been shown in other regions, eddies can have a significant effect on the near-surface chlorophyll levels (Chelton et al. 2011; Dufois et al. 2014; He et al. 2016a; Gaube et al. 2013, 2014; Huang and Xu 2018). The cross-correlation between spatially high-passed chlorophyll anomalies and sea surface height anomalies, recreated as following Gaube et al. (2014) to isolate mesoscale features, is shown in Figure 4.1. There is large spatial variability in this cross-correlation, indicating significant variation in the near-surface chlorophyll response to the presence of eddies. One such area with an inconsistent chlorophyll anomaly to sea surface height anomaly correlation is in the South Pacific Subtropical Counter-Current (STCC) (see Figure 4.1b). This is an area of heightened eddy

activity with a relatively weak mean current (approximately 3-5 cm s^{-1}), and the pinching off of meanders has not been observed to be a significant feature. The current is associated with baroclinic instabilities (Travis and Qiu 2017; Rieck et al. 2018; Qiu et al. 2008), and spans a transition into highly oligotrophic waters as moving down current from west to east. This study explores the possible driving mechanisms in the region which could cause the inconsistent response. Known driving mechanisms include trapping of surface waters and nutrients during eddy formation to sustain chlorophyll anomalies, stirring of surface waters and chlorophyll gradients, mixed layer depth anomalies affecting the availability of access to deep nutrient pools, and upwelling/downwelling generated during eddy formation, through eddy-Ekman pumping, or by submesoscale frontal processes (Chelton et al. 2011; Dufois et al. 2014; Gaube et al. 2013; He et al. 2016a; Martin and Richards 2001; McGillicuddy 2016; Zhang and Qu 2014; Zhang et al. 2019).

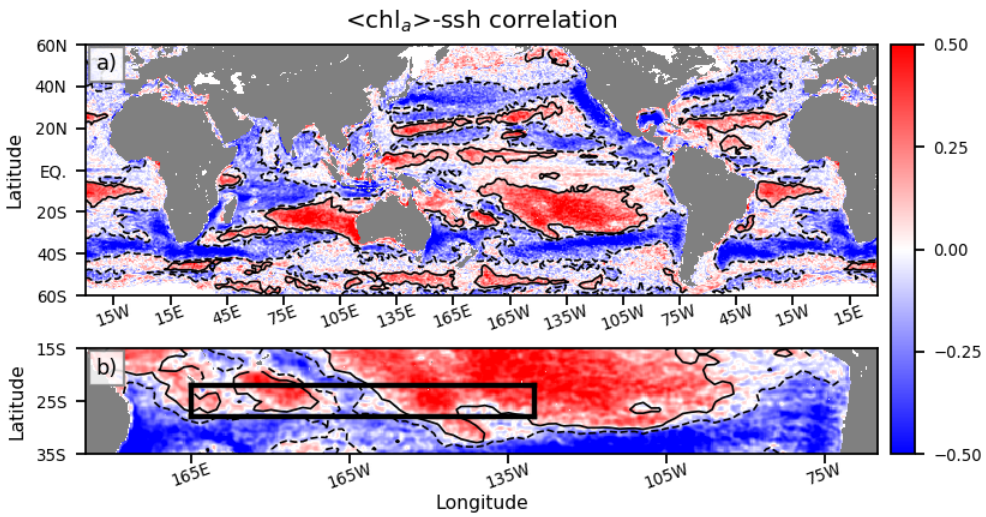

Figure 4.1: a) Global map of <chl$_a$>-ssh anomaly cross correlation. b) South Pacific map of <chl$_a$>-ssh anomaly cross correlation, with the STCC region of study indicated by the black box from 22°-28°S and 165°E-130°W. In both maps, cross correlation is taken between spatially high-passed SSH anomalies and chl$_a$ anomalies. The cross correlation has been spatially smoothed with a 2^{nd}-order Lanczos filter with a 1 degree half-width window. The solid black contours indicate areas of significant positive cross correlation ($>$ 0.1) and the dashed black contours indicate area of significant negative cross correlation ($<$ -0.1). Correlation significance is calculated at the 95% significance level, following von Storch and Zwiers (1999), using the formula $q_t(\pm 0.025; \text{n-2})/\sqrt{n}$, where $q_t(\pm 0.025; \text{n})$ is the 2.5 percentage point of the Student's t distribution with n-2 degrees of freedom, and n is estimated as the number of days of data.

When eddies form, they can trap waters of a particular temperature and/or salinity (Dong et al. 2014; Dufour et al. 2015) as well as local phytoplankton and nutrients. As the eddies move throughout the ocean, they can carry these signatures with them. This mechanism is particularly important during the start of the eddy life cycle, as any nutrients can be quickly consumed to support biological activity already present in the eddy. Eddy stirring is important at gradients of chlorophyll, where the largely horizontal eddy currents skew the surface gradients, creating a dipole of positive and negative chlorophyll signals based upon the strength of the gradient, the orientation of the gradient and the strength of the eddy. These horizontal mechanisms primarily create chlorophyll anomalies through advection of

chlorophyll, and do not necessarily involve any change in levels of primary production in the region (Chelton et al. 2011; McGillicuddy 2016)

Cyclonic/anticyclonic eddies generate upwelling/downwelling during their intensification periods, the initial growth and development period of eddies. This is typically on the order of 1 m day^{-1} (Gaube et al. 2015). Eddy-induced Ekman pumping is caused by the curl of surface wind stress due to the relative motions of the surface currents and surface winds (Martin and Richards 2001; Gaube et al. 2015). Locally, this can be larger than the Ekman pumping caused by the surface stress derived only from the curl of the surface winds, as the eddy-induced wind stress curl occurs over length scales of hundreds of kilometers, much smaller than the regional Ekman pumping. Relative to the eddy pumping during the spin-up of the eddy, this is an order of magnitude smaller (~10 cm day^{-1}). Gaube et al. (2015) explored the regional strength of eddy-induced Ekman pumping, including an area to the northeast of the South Pacific STCC region, and found a typical eddy Ekman-induced pumping velocity is 8 cm day^{-1}. This mechanism would be present throughout the life cycle of the eddy, and in the case of eddy-Ekman induced upwelling in anticyclones, can provide a continuous source of deep nutrients to the euphotic zone. Lastly, frontal instabilities have been shown to create strong vertical velocities at the sub-mesoscale (Klein and Lapeyre 2009; Zhang et al. 2019); however, this mechanism will be outside of the purview of this work.

Mixed layer depth anomalies are also expected to alter the surface expression of chlorophyll concentrations. It has been observed that anticyclones typically have deeper mixed layers than cyclones (He et al. 2016a; Dufois et al. 2014; Gaube et al. 2019) due to the relative isopycnal displacement of the two types of eddies. As described in McGillicuddy (2016), the expected character of the phytoplankton response to mixed layer depth anomalies is dependent on whether light or nutrients limit phytoplankton growth. In highly oligotrophic, low nutrient regions, deeper mixed layers are able to access a deep pool of nutrients which would otherwise be unavailable in the surface waters. In these cases, the deeper mixed layers of anticyclones can spur higher chlorophyll levels than cyclones, as they are able to access a larger nutrient pool. Conversely, in a highly productive, high-nutrient region, there are

often sufficient nutrients, and it is the lack of sufficient light penetration which prevents further production. In this case, the deeper mixed layers can cause mixing to occur deeper than the euphotic layer. When this happens, phytoplankton in the mixed layer receive lower average ambient light, thus decreasing productivity. In these cases, the deep mixed layers of anticyclones would lead to lower chlorophyll levels than cyclones.

Large portions of the oceanic basins are in areas of low mean chlorophyll, which often have nutriclines too deep to have injection of nutrients into the mixed layer (McClain et al. 2004). Mignot et al. (2014) examined the seasonality of these oligotrophic areas, finding that the seasonal depth of the mixed layer is important in determining whether changes in near-surface chlorophyll are caused by new production or changes in intracellular pigmentation due to photoacclimation. Similarly, Dufois et al. (2016) found that anticyclonic eddies have elevated chlorophyll levels in subtropical gyres due to deep winter mixing. In the South Pacific, the oligotrophic region of the gyre is found to have very low nutrient levels, and an exceptionally deep nutricline (Bender and Jonsson 2016; Dufois et al. 2016). He et al. (2016a), as well as others (Chelton et al. 2011; Dufois et al. 2014), found a connection between the chlorophyll response to the presence of eddies and the relative depths of the mixed layer and the nutricline. A deep nutricline could prevent eddies from having a strong effect of local productivity. However, in regions of transition between highly oligotrophic waters with a particularly deep nutricline and more productive waters, typical closer to coastal areas, then the seasonally varying mixed layer depth could cause intermittent access to this deep nutrient pool.

The wide range of forcing mechanisms and the varied responses to these forcings, as well as the seasonally varying environment in which the eddies are situated create a complex system. Careful consideration of the relative strengths of each of these forcings is required. It is hypothesized that the eddying STCC region crosses a transition region from a modestly productive region to one of ultra-low nutrient availability (Bender and Jonsson 2016), and that within this transition, seasonally-changing access to deep nutrient pools can result in an seasonally-alternating character of response of near-surface chlorophyll in eddies. A seasonal

analysis is needed to fully quantify the effect that eddies have on biological signals in the region. Using a combination of data of near-surface chlorophyll, sea surface height, and eddy tracks, seasonal patterns of chlorophyll anomalies within eddies can be observed. Additional data, such as light availability, mixed layer depths within eddies, nutrient availability, and wind forcing, can be used to determine the dominant drivers of the chlorophyll anomalies and the subsequent limiting factors.

4.2 Data and Methods

4.2.1 Data Sets

An analysis of the regional near-surface chlorophyll response to mesoscale eddies draws from a large number of data sources. These include the Glob-Colour merged satellite ocean color product, Aviso satellite altimetry data of sea surface height, eddy tracks as provided from the Aviso eddy atlas, Argo float profiles of temperature and salinity, as well as the Argo float profile mixed layer depth product from Holte et al. (2017). For climatological nutrient data, the World Ocean Atlas 2018 was used (Garcia et al. 2019). Lastly, wind stress data was taken from QuikSCAT V3. Each of these data sets will be used to construct eddy-centric seasonal cycles of the relevant parameters. For anomalies of near-surface chlorophyll, sea surface height, geostrophic velocities, and wind stress, monthly composites can be made to illustrate spatial patterns of these parameters within a "typical" eddy. The analysis period runs from January 2004 to December 2017, with the exception of the wind stress data, for which the analysis will run from January 2000 to December 2008. The period of January 2004 to December 2017 was chosen, as there is robust data coverage in ocean color, satellite altimetry data, and Argo float profiles. The wind data period is chosen to provide maximum observational time coverage in order to construct seasonal patterns of eddy-Ekman pumping.

The Aviso 0.25° x 0.25° gridded daily satellite product of absolute dynamic topography, as processed by CNES/CLS is used for sea surface height (SSH). Geostrophic velocities are also available, and will be used. The data were analyzed from January 2004 to December

2017. A mesoscale eddy trajectory atlas is processed and generated by CNES/CLS. The eddy trajectories are generated following the same method for eddy identification and tracking as developed by Schlax and Chelton. From this atlas, eddy centers and radii were used to approximate the size of the eddies, which can then be used to co-locate the corresponding chlorophyll, SSH, and wind stress anomalies within the area of the eddies.

Wind stress data are from a gridded product of daily data with 0.25° x 0.25° spatial resolution, as produced by Ifremer/CERSAT. The data used in producing the gridded product are taken from QuikSCAT V3 data, a reprocessing of QuikSCAT scatterometer wind retrievals. The wind data are produced for the time period of October 1999 to November 2009. For the purposes of this analysis, data from January 2000 to December 2008 is used.

Argo floats are used to examine subsurface characteristics - primarily, they are used to examine mixed layer depths and isopycnal displacements. Argo profiles are accessed from U.S. Global Ocean Data Assimilation Experiment (USGODAE) (`https://www.usgodae.org/argo/argo.html`). Mixed layer depths for individual Argo profiles are taken from the Argo profile mixed layer depth product (Holte et al. 2017).

Nutrient information is taken from climatological nitrate data for the World Ocean Atlas 2018. (Garcia et al. 2019) Climatological monthly means of nitrate are given on 1°x1° spatial resolution at standard depth levels (47 depth levels in the upper 1000 meters). For the purposes of this analysis, the nitracline shall be defined as the depth where NO_3^{-1} exceeds 1 μmol kg^{-1}.

The Glob-Colour ocean color dataset is a merged product of the various ocean color sensor platforms in use during the operational periods, such as SeaWIFS (Sea-Viewing Wide Field of View Sensor), MERIS (Medium Resolution Imaging Spectrometer), MODIS (Moderate Resolution Imaging Spectrometer) Aqua, VIIRS (Visible Infrared Imaging Radiometer Suite), and OLCI-A (Ocean Land Color Instrument), giving the advantage of improved temporal and spatial coverage. The 0.25° x 0.25° gridded product of daily data was chosen. For the purposes of this study, the analysis is restricted to the period of January 2004 to December 2017, as this provides spatial and temporal resolution consistency with the SSH data set.

From this Glob-Colour product, the following data are accessed: a) near-surface chlorophyll-a (chl_a) merged using the Garver-Siegel-Maritorena (GSM) (Maritorena et al. 2002) method for type 1 waters; b) diffuse attenuation coefficient of downwelling irradiance at 490 nm ($k_{d(490)}$), which can be used as a measure of turbidity, while the inverse of the coefficient gives a measure of how deep the satellite is able to "see"; c) photosynthetically available radiation (PAR) between 400 and 700 nm, which is a measure of how much solar energy reaches the ocean and is available for photosynthesis. The GSM method is a semi-analytic technique for calculating and merging data from multiple sensors, and was tuned using chlorophyll data in the range of 0.02-10 mg m^{-3}. It should be noted that while the method has no theoretical limits, the range of values observed in the regional seasonal background chlorophyll levels approaches the bottom limit of this range. A combination of these parameters is used to test for changes in light penetration depth and any chlorophyll changes due to photoacclimation, which is the adjustment of intracellular pigmentation compensating for changing ambient light levels (Behrenfeld et al. 2005).

4.2.2 Methods

While the Glob-Colour product provides improved spatial and temporal coverage by drawing upon the data from multiple sensors, the data can still have gaps due to lack of coverage for a specific day or from cloud coverage preventing observation of an area. To help fill the gaps, a spatio-temporal smoothing of the data is performed. First, the chlorophyll data are $\log_{10}$ transformed to account for the skewed distribution of chlorophyll measurements (Campbell 1995). Following this, a three-dimensional convolution with a 2nd-order Lanczos window is then applied to the data to help interpolate between points. The Lanczos window has a 7-day temporal half-width and a 0.5 degree half-width in the latitudinal and longitudinal directions, respectively. Additionally, the interpolated data point is only used if the summed weight given to the nearby observations exceeds the maximum weighted point in the window, i.e., the point at which the interpolation occurs; if the summed weight of the points for which data are available is not larger than the maximum weight, then the point is left as a missing

gap. This is done to ensure that any interpolation is sufficiently robust, and not done by an interpolation from the points only at the edge of the window.

After filling the data gaps, additional processing of the chlorophyll data is done to attempt to remove small-scale, high-frequency signals which are not associated with mesoscale dynamics. This can include signals associated with intermittent bloom events (He et al. 2016a) or events associated with filament structures along submesoscale instability fronts (Zhang et al. 2019). First, the data are temporally smoothed using a 2nd-order Lanczos filter with a 30-day half-width. Next, a 2nd-order Lanczos filter with a 1-degree half-width is applied in the longitudinal and latitudinal directions.

The chlorophyll data are log-transformed back to linear concentrations (chl_a), and a spatial high-pass Lanczos filter with a 6-degree half-width is applied to isolate the mesoscale features ($\mathrm{chl}_a{}'$), removing larger basin-scale signals ($\overline{\mathrm{chl}_a}$), such as seasonal background levels.

$$\mathrm{chl}_a{}' = \mathrm{chl}_a - \overline{\mathrm{chl}_a} \tag{4.1}$$

The residual from this filtering, being the low-pass Lanczos filtered data, is retained to give a measure of the background chlorophyll state, which permits basin-wide chlorophyll changes such as a seasonal cycle. These methods follow similar work by others observing mesoscale features (Chelton et al. 2011; Gaube et al. 2014; He et al. 2016a,b). These filtering processes are also applied to $\mathrm{k}_{d(490)}$, while the last step of spatial high-pass filtering is also applied to SSH, geostrophic velocities, and wind stress data for consistency. The filtering process allows the retention of the chlorophyll anomalies ($\mathrm{chl}_a{}'$), the background, seasonally-varying chlorophyll ($\overline{\mathrm{chl}_a}$), and the normalized chlorophyll anomalies ($<\mathrm{chl}_a>$), which is the ratio of the chlorophyll anomaly to the background chlorophyll.

$$<\mathrm{chl}_a> = \frac{\mathrm{chl}_a{}'}{\overline{\mathrm{chl}_a}} \tag{4.2}$$

Figure 4.1a shows the global patterns of the cross-correlation between near-surface chlorophyll-a anomalies and sea surface height anomalies, recreated following (Gaube et al. 2014). Figure 4.1b provides a closer look at the patterns within the South Pacific, with the eddying region

of the South Pacific STCC highlighted within the black box, which runs from 165°E-130°W and 22°S-28°S. In the STCC, there is a predominantly positive $<chl_a>$-ssh correlation in the eastern half of the box while the western half of the box has no clear positive or negative pattern. For this reason, the analysis in this paper will divide the STCC region into an eastern and western analysis region. The western region extends from 165°E to 170°W and the eastern half extends from 160°W to 130°W. To examine the seasonal and regional differences in chlorophyll response to eddies, the following analyses are performed:

1. A Hovmueller diagram of $<chl_a>$ across a latitudinal band (22°S-28°S) is created to reconstruct a seasonal cycle while also examining some spatial variability. This is done separately for cyclones and anticyclones. To do so, the average chlorophyll anomaly within all cyclones(anticyclones) within a 5-degree longitude box for a given month are binned to find the average anomaly.

2. Composite averages of the $<chl_a>$, ssh, geostrophic velocities, and wind stress fields can be made. The composites are made by using the eddy track atlas to identify the location of the eddy center and the size of the eddy (eddy radius). For each instance of an eddy, the distance from the eddy center is normalized by the eddy radius, the x-y coordinate axes are aligned perpendicular to the strongest local background chlorophyll gradient, and data within ± 2 eddy radii are used to create the composites (i.e., data from $\pm$ 2 eddy radii in the x and y-direction). In the normalization, 0 is the eddy center, and ± 1 is the edge of the eddy. This method allows for the construction of eddy composites from eddies of various sizes, and is frequently used in studies of eddy anomalies. (Chelton et al. 2011; Dawson et al. 2018; Dufois et al. 2016, 2017; Frenger et al. 2018; Gaube et al. 2013, 2014, 2015; He et al. 2016a; Song et al. 2018) Table 4.1 provides statistical information on the eddies used in creating the composites. For consistency, the spatial chlorophyll gradient ($\nabla <chl_a>$) is calculated, and the data are rotated such that the maximum chlorophyll gradient occurring within an eddy decreases in the positive y-direction (i.e., the chlorophyll decreases from a maximum at the bottom of the composite to a minimum at the top of the composite). Composites are made onto

a ± 2 eddy-radius window with $^1/_8$ eddy-radius step size for grid resolution. Additional composites are made of SSH anomalies, geostrophic velocities, and wind stress curl anomalies. These composites are made over the same spatial region as the chlorophyll composites and are subjected to the same rotation. In the case of the wind stress curl composites, the data are rotated such that the large-scale wind field is in the positive x-direction (left to right).

Using the background chlorophyll data and the Aviso geostrophic velocity data, composites are made of the material derivative of chlorophyll ($\mathrm{D(chl}_a)/\mathrm{Dt}$). The material derivative is the sum of the local time rate of change and the advection of the signal gradient.

$$\frac{\mathrm{D(chl}_a)}{\mathrm{Dt}} = \frac{\partial}{\partial \mathrm{t}}\big(\mathrm{chl}_a\big) + \mathbf{u} \cdot \nabla\big(\mathrm{chl}_a\big) \tag{4.3}$$

In this equation, the time derivative is the local rate of change. $\mathbf{u}$ is the geostrophic velocity vector and $\nabla(\mathrm{chl}_a)$ is the chlorophyll gradient, with $\mathbf{u} \cdot \nabla(\mathrm{chl}_a)$ representing the advection of the chlorophyll gradient. The advection of the chlorophyll gradient by geostrophic velocity includes the advection of both the background chlorophyll ($\overline{\mathrm{chl}_a}$) and the chlorophyll anomaly ($\mathrm{chl}_a{}'$). The time derivative of chlorophyll is calculated using a central differencing scheme in time. The chlorophyll gradients are calculated using forward differencing in space. The material derivative can then be normalized by the background chlorophyll gradient to create $\mathrm{D(chl}_a)/\mathrm{Dt}$. Composites of $\mathrm{D(chl}_a)/\mathrm{Dt}$ are constructed to explore the effect of the advection of background chlorophyll by eddies on the observed chlorophyll anomalies.

From the composites of chlorophyll anomalies and the chlorophyll material derivative, the monopole/dipole structure is found. Following He et al. (2016a), the monopole structure is found by calculating the radially averaged signal from each composite. The dipole structure is taken as the residual after the monopole structure is removed from the original composite.

The eddy-composites are averaged by month. In connection with the Hovmueller diagrams, these can illustrate how the structure of the chlorophyll anomaly response changes by region, by season, and by eddy type.

3. Eddy composites are separated into their monopole and dipole structures for the $<\text{chl}_a>$ and $\text{D}(\text{chl}_a)/\text{Dt}$. Monthly composites are combined into 3-month quarterly averages, with the quarterly periods centered on the month of the maximum of amplitude in the seasonal reversal. For example, if the yearly average cyclonic $<\text{chl}_a>$ for a region is positive, and the region experiences a large negative value (i.e., the maximum magnitude of the seasonal reversal) in July, then the quartile will be centered in July, with all subsequent quartiles conforming as necessary.

4. Eddy-composites of eddy-Ekman pumping are created for the available time period of the data. The composites are constructed by quarter, as found for the monopole/dipole structures, and by eddy type. Eddy-Ekman pumping can be decomposed into surface current-induced Ekman pumping, vorticity gradient-induced Ekman pumping, and a planetary gradient-induced Ekman pumping (Gaube et al. 2015). However, for the purpose of this paper, only the surface current-induced Ekman pumping is considered, as it typically is of the largest magnitude:

$$w_{ek} = \frac{\nabla \text{x} \overline{\tau}}{\rho(f + \zeta)} \tag{4.4}$$

where $\overline{\tau}$ is the surface wind stress, ρ is the reference seawater density of 1025 kg m^{-3}, f is the Coriolis parameter at the eddy center, and ζ is the local vorticity within the eddy. In an idealized scenario of constant wind forcing over an eddy, the surface current-induced Ekman pumping would have a monopole structure with a maximum magnitude at the eddy center (Martin and Richards 2001).

5. Within each region, the seasonal cycle of nitrate availability as distributed with depth is found. The nitracline depth, being defined as the depth where nitrate exceeds 1

umol L^{-1} ($NO_3^- > 1$ μmol kg^{-1}), is calculated for each month. Additionally, this cycle is explored in relation to monthly values of mixed layer depth, the euphotic layer depth (z_{eu}), and the averaged nitrate anomalies within mixed layers of eddies. Mixed layer nitrate concentrations are calculated by determining a monthly averaged mixed layer depth for anticyclones, cyclones, and outside of eddies from co-located Argo profiles, using the Argo MLD database (Holte et al. 2017). This mixed layer depth is then used with the WOA18 nitrate climatology to calculate the mixed layer depth nitrate concentration in anticyclones, cyclones, and outside of eddies for any given month.

6. Regionally averaged seasonal changes are examined for background chlorophyll, chlorophyll anomalies, and photosynthetically available radiation within the mixed layer (PAR_{ML}). Following Morel et al. (2010), PAR_{ML} is calculated as:

$$PAR_{ML} = \frac{1}{MLD} \int_{MLD}^{0} PAR(0) exp(-k_{d(PAR)} z) \delta z \tag{4.5}$$

where PAR_{ML} is related to $k_{d(490)}$ by the following equation, following Morel et al. (2007):

$$k_{d(PAR)} = 0.0665 + 0.874 k_{d(490)} - 0.00121 k_{d(490)}^{-1} \tag{4.6}$$

Within these equations, $k_{d(490)}$ is the diffuse attenuation coefficient at 490 nm, PAR(0) is the photosynthetically available radiation at the surface of the ocean, and MLD is the mixed layer depth averaged regionally and within eddies. To calculate MLD, the Argo profile mixed layer depth product (Holte et al. 2017) is used. Annual cycles of MLD for the western and eastern regions are constructed for inside and outside of eddies, and these MLD values are used in equation 4.5 according to each location's respective case (in cyclones, in anticyclones, or not in an eddy).

A photoacclimation response would show that chl_a has an inverse response to PAR_{ML}. As ambient light levels increase in the summer, phytoplankton are able to respond

Table 4.1: Overview of Eddy Statistics for Each Region in the South Pacific Subtropical Counter-Current for the time period of January 2004 - December 2017

Parameters	**West (165°W-165°E)**		**East (160°E-130°E)**	
	Anticyclones	Cyclones	Anticyclones	Cyclones
Average N per month	2419 ± 159	2549 ± 156	3279 ± 249	3337 ± 123
Average N* per month	102 ± 7	111± 7	132 ± 11	137 ± 7
Length (km)	100 ± 32	96 ± 32	96 ± 31	93 ± 30
Axial Speed (cm s^{-1})	24.3 ± 7.6	25.3 ± 7.6	16.7 ± 5.2	17.6 ± 5.4
Max $<chl_a>$	6.10 ± 2.66	3.34 ± 1.50	5.90 ± 0.94	-0.64 ± 1.48
Min $<chl_a>$	-3.14 ± 1.30	-6.17 ± 1.67	0.98 ± 1.54	-5.29 ± 0.78
Max chl_a' (10^{-2} mg m^{-3})	0.55 ± 0.24	0.53 ± 0.24	0.31 ± 0.05	-0.30 ± 0.03
Min chl_a' (10^{-2} mg m^{-3})	-0.38 ± 0.15	-0.53 ± 0.14	0.03 ± 0.05	-0.02 ± 0.04
Max $<chl_a>$ Month	February	August	August	December
Min $<chl_a>$ Month	September	March	December	July
Min $\overline{chl_a}$ (mg m^{-3})	0.078		0.026	
Max $\overline{chl_a}$ (mg m^{-3})	0.163		0.062	

N is the total number of eddy realizations during a given month.
N* is the number of individual eddies during a given month.
Confidence intervals (± ranges) are 1 standard deviation for N, N*, Length, and Axial Speed
Confidence intervals for $<chl_a>$, chl_a' are 95% intervals, as calculated using the student's t distribution.

more efficiently, and require less chlorophyll to sustain photosynthesis. Additionally, shallow summer mixed layers would constrain waters closer to the surface, where ambient light levels are the highest. Conversely, the low ambient light in the winter in combination with deep mixed layers mean that there is less PAR available to phytoplankton. In this case, phytoplankton may need to produce more chlorophyll to meet their photosynthetic demands.

4.3 Results

In the South Pacific STCC, there are distinct separations of the character of the chlorophyll response to eddies (Figure 4.2). This separation is expected from the inconsistent $<chl_a>$-

ssh anomaly correlation (Figure 4.1b). A summary of the major results are found in Table 4.1. Monthly composites of chlorophyll anomalies in eddies in eastern and western region are shown in Figures 4.3 and 4.5, respectively, while monopole/dipole quartile composites of $<chl_a>$ and $D(chl_a)/Dt$ for the eastern and western region are shown in Figures 4.4 and 4.6, respectively. Seasonal cycles of $\overline{chl_a}$, chl_a', and PAR_{ML} are shown in Figure 4.9.

In the eastern portion of the STCC, there is a consistent chlorophyll anomaly response throughout the year, with maximum anomalies occurring during the austral winter. Cyclones(anticyclones) consistently have negative(positive) chlorophyll anomalies. This is consistent with the positive $<chl_a>$-ssh correlation in the region. The magnitude of the chl_a' is largely in phase with the seasonal variability of the background chlorophyll ($\overline{chl_a}$), which reaches a maximum of 0.062 mg m^{-3} in August, during the austral winter. The chlorophyll anomalies, chl_a', can reach a maximum magnitude of 0.0031 mg m^{-3} in August and -0.0030 mg m^{-3} in July for anticyclones and cyclones, respectively. The normalized peak anomalies ($<chl_a>$) are $5.90\% \pm 0.94\%$ and $-5.29\% \pm 0.78\%$ of the background chlorophyll for anticyclones and cyclones, respectively (Figure 4.3). It should be noted that the magnitudes of these anomalies are low when compared to the tuned range of the GSM method. This highlights the advantage of the eddy-centric composites, in which the mesoscale eddy signal, even at low relative signal, can be observed.

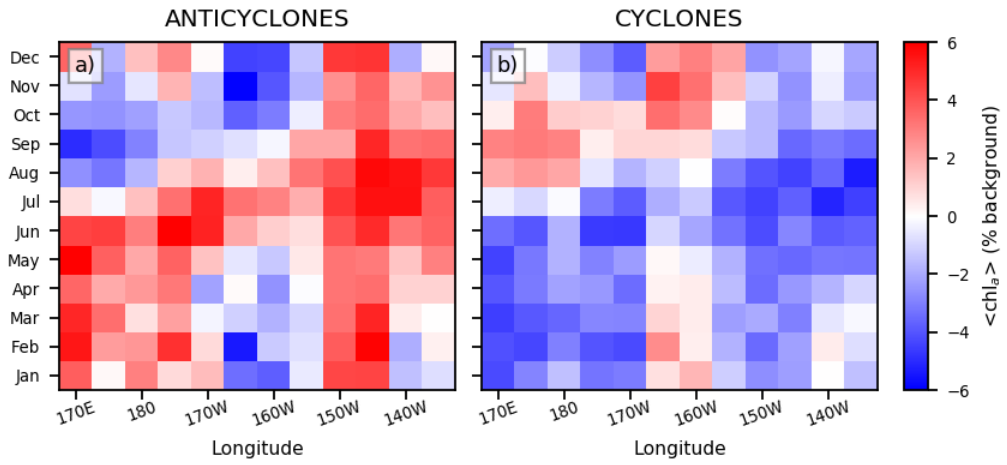

Figure 4.2: Hovmueller x-t diagram of normalized chlorophyll anomalies (<chl$_a$>) by month. The x-t diagram is averaged between 22°S - 28°S, binned into 5 degree longitude boxes from 165°E to 130°W. This region is the boxed area seen in Figure 4.1b.

Composites of <chl$_a$> and D(chl$_a$)/Dt for the eastern STCC are shown split into a monopole/dipole structure, with the intensity of those structures varying throughout the year (Figure 4.4a). The composites are grouped into quarterly periods, with the peak anomaly period centered around September. The monopole/dipole structures for the eastern STCC show a consistent pattern throughout the year. Cyclones(anticyclones) have a negative(positive) chlorophyll anomaly throughout the year, which peaks to a maximum magnitude in July/August, during the austral winter. The magnitude of the dipole structure is calculated as the average of the absolute value of the <chl$_a$> within 1 eddy radius. The monthly average of the monopole/dipole magnitudes in cyclones and anticyclones is shown in Figure 4.4b. The magnitude of the dipole anomalies is similar for cyclones and anticyclones, and remains at approximately 1-2% of $\overline{\text{chl}_a}$ throughout the year. The magnitude of the dipole is of the same magnitude of the monopole during the austral summer, and is roughly half of the monopole signal during the austral winter. The D(chl$_a$)/Dt dipole pattern strongly resembles that of the chlorophyll anomaly dipole pattern, with a reversed anomaly sign. This is indicative that the dipole pattern observed is largely due to advection of the background chlorophyll gradient. The D(chl$_a$)/Dt monopole pattern is dominated by the background

seasonal signal, with an increasing signal during the fall/winter and decreasing during the spring/fall.

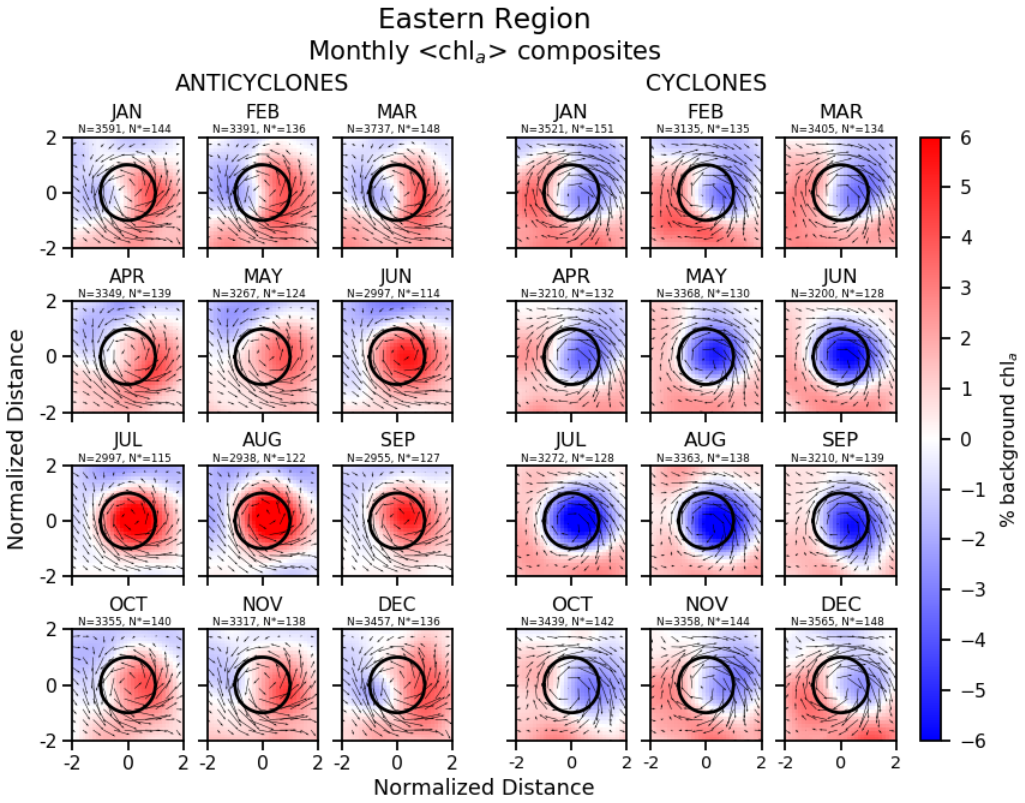

Figure 4.3: Composites of normalized chlorophyll anomalies in eddies in the eastern South Pacific STCC (160°W-130°W) by month, as a percent of the background chlorophyll level. Anticyclones are shown by month in the left half of the figure, while cyclones are shown by month in the right half of the figure. The black circle indicates one eddy radius from the center. The arrows are calculated geostrophic velocity vectors, as calculated from sea surface height anomalies. The colorbar indicates the normalized chlorophyll anomaly, given as a percent of the large scale, background chlorophyll signal. Above each composite, the number of daily eddy composites used for each monthly average is given as N, while the number of individual eddies, which persist throughout the month, is given as N*. For the purposes of conservative efforts in estimating confidence intervals, seen in Figure 4.4, N* is used in an estimate of the number of degrees of freedom. For statistical characteristics of the eddies used in composites, refer to Table 4.1.

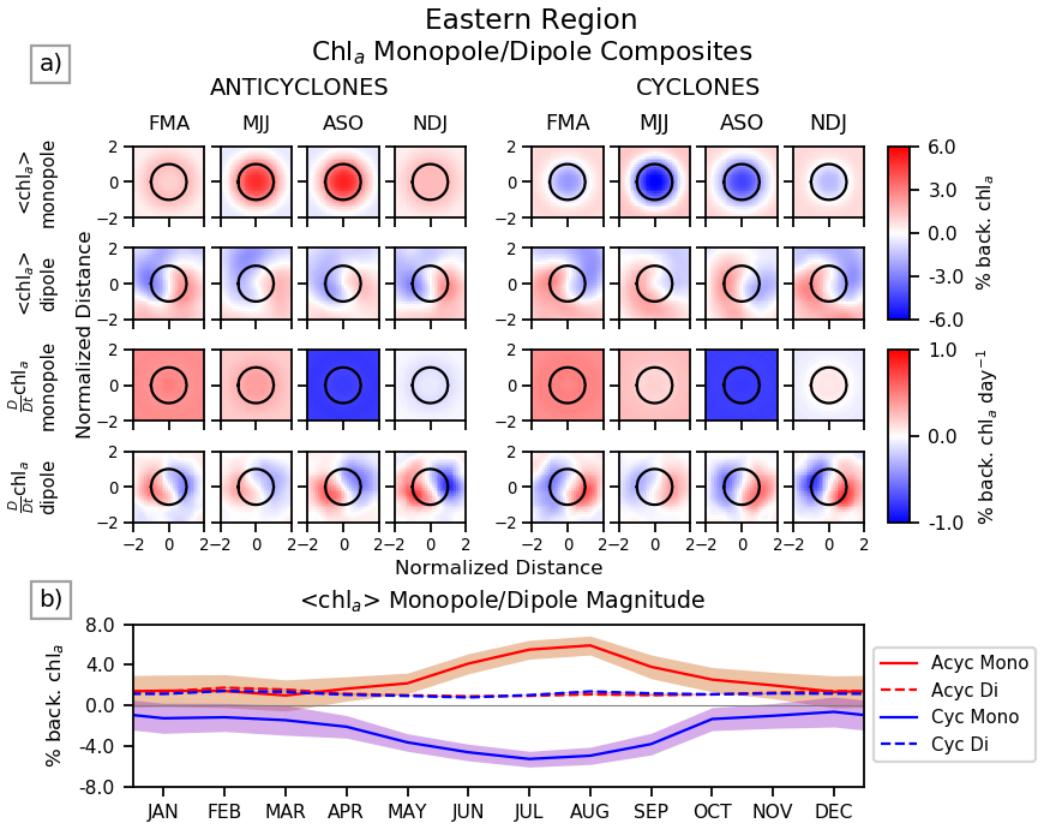

Figure 4.4: a) Composites by quarterly period for the eastern South Pacific STCC (160°W-130°W). Anticyclones/cyclones are shown in the left/right halves of the figure, respectively. Quarterly periods are as follow: FMA = February - April, MJJ = May - July, ASO = August - October, NDJ = November - January. The top row is the monopole structure of the normalized chlorophyll anomaly, with the dipole structure shown on the second row. The colorbar for these composites is the normalized chlorophyll anomaly, given as a percent of the large scale, background chlorophyll signal. The third and fourth row show the monopole and dipole structure, respectively, for the Lagrangian derivative $\frac{D}{Dt}(\text{chl}_a)$ of normalized chlorophyll anomalies. The colorbar for these composites is a normalized chlorophyll rate of change, given as a percent of the large scale, background chlorophyll signal per day. The black circle indicates one eddy radius from the center. b) The bottom figure shows the relative magnitude of the monopole/dipole structure, by month, by eddy type. Anticyclones/cyclones are indicated by the red/blue lines, and monopole/dipoles are indicated by the solid/dashed lines. This monthly time series indicates the magnitude of the monopole and dipole structure within cyclones and anticyclones. The shaded red and blue areas indicate the 95% confidence interval for the monopole structures, using a standard t distribution, where N* degrees of freedom are taken as the number of individual eddies used in each composite (see Figure 4.3).

In the western portion of the STCC, a very different pattern is observed. From January to June, cyclones (anticyclones) have weakly negative (positive) anomalies, whereas from July to December, cyclones (anticyclones) have positive (negative) anomalies. During the austral spring (August to October), the greatest magnitude anomalies occur, as seen in Figures 4.5 and 4.6. The chlorophyll anomaly averaged within one eddy radius ranges for cyclones is -0.0053 mg m^{-3} in March to 0.0053 mg m^{-3} in August. The range for anticyclones is 0.0055 mg m^{-3} in February to -0.0038 mg m^{-3} in September. As the background chlorophyll levels vary seasonally from 0.0780 mg m^{-3} in December to 0.1630 mg m^{-3} in August, this results in a normalized chlorophyll anomaly of -6.17% $\pm$ 1.67 to 3.34% $\pm$ 1.50% for cyclones and 6.10% $\pm$ 2.66% to -3.14% $\pm$ 1.30% for anticyclones. Note that the seasonal variability in the chlorophyll anomalies is out of phase with the seasonal variability of the background chlorophyll. The magnitude of the dipole structure ranges between 2.0-3.0% throughout the year, and is typically of the same magnitude as the monopole structure during the austral spring reversal when the dipole magnitude is greater than the monopole magnitude.

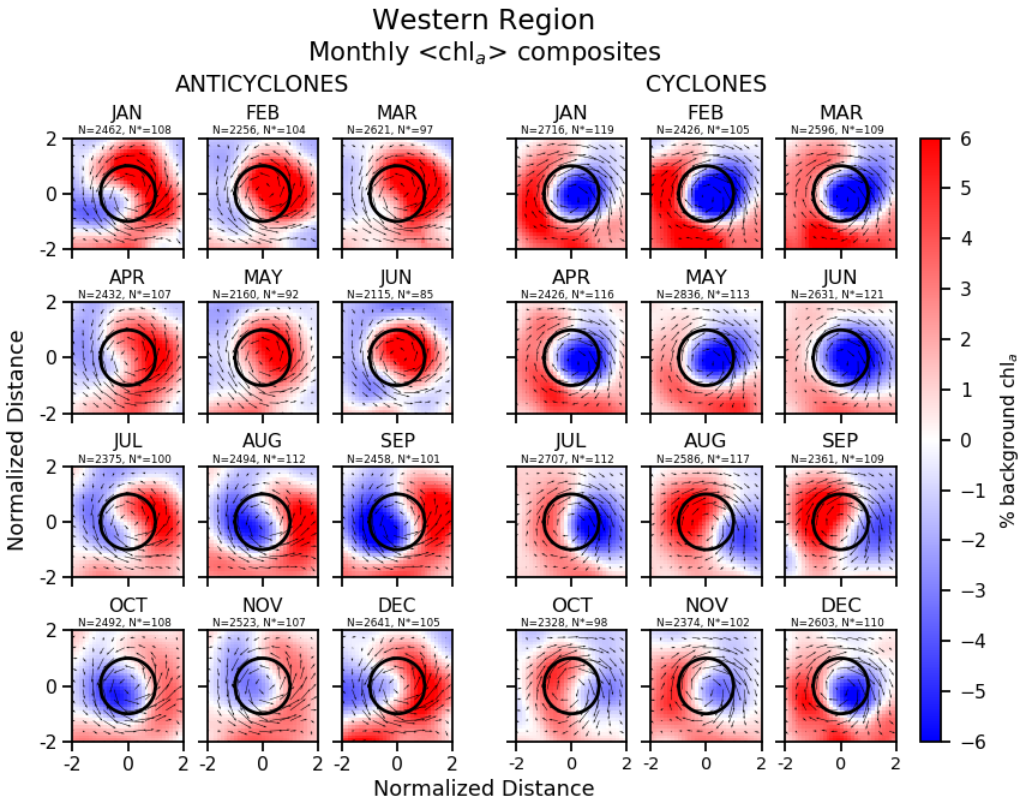

Figure 4.5: Composites of normalized chlorophyll anomalies in eddies in the western South Pacific STCC (165°E-170°W) by month, as a percent of the background chlorophyll level. Anticyclones are shown by month in the left half of the figure, while cyclones are shown in the right half of the figure. The black circle indicates one eddy radius from the center. The arrows are calculated geostrophic velocity vectors, as calculated from sea surface height anomalies. The colorbar indicates the normalized chlorophyll anomaly, given as a percent of the background, large scale chlorophyll signal. Above each composite, the number of daily eddy composites used for each monthly average is given as N, while the number of individual eddies, which persist throughout the month, is given as N*. For the purposes of conservative efforts in estimating confidence intervals, seen in Figure 4.4, N* is used in an estimate of the number of degrees of freedom. For statistical characteristics of the eddies used in composites, refer to Table 4.1.

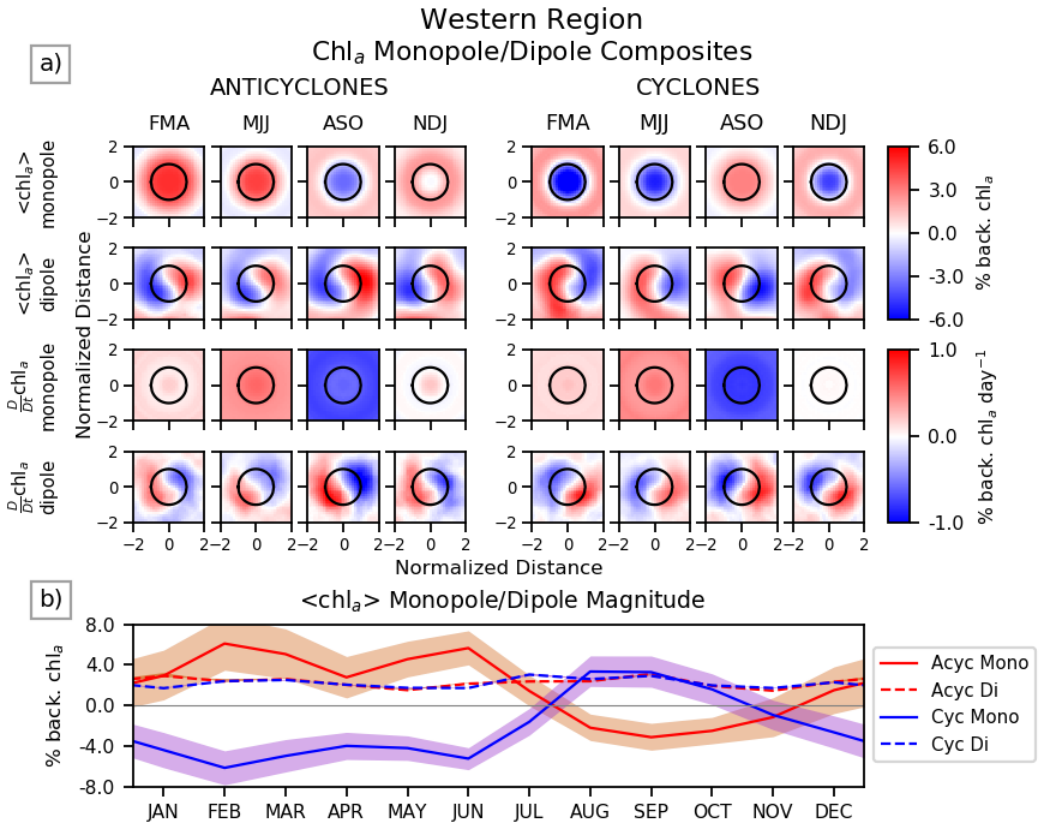

Figure 4.6: a) Composites by quarterly period for the western South Pacific STCC (165°E-170°W). Anticyclones/cyclones are shown in the left/right halves of the figure, respectively. Quarterly periods are as follow: FMA = February - April, MJJ = May - July, ASO = August - October, NDJ = November - January. The top row is the monopole structure of the normalized chlorophyll anomaly, with the dipole structure shown on the second row. The colorbar for these composites is the normalized chlorophyll anomaly, given as a percent of the large scale, background chlorophyll signal. The third and fourth row show the monopole and dipole structure, respectively, for the Lagrangian derivative $\frac{D}{Dt}(\text{chl}_a)$ of normalized chlorophyll anomalies. The colorbar for these composites is a normalized chlorophyll rate of change, given as a percent of the large scale, background chlorophyll signal per day. The black circle indicates one eddy radius from the center. b) The bottom figure shows the relative magnitude of the monopole/dipole structure, by month, by eddy type. Anticyclones/cyclones are indicated by the red/blue lines, and monopole/dipoles are indicated by the solid/dashed lines. The monthly time series indicates the magnitude of the monopole and dipole structure within cyclones and anticyclones. The shaded red and blue areas indicate the 95% confidence interval for the monopole structures, using a standard t distribution, where N* degrees of freedom are taken as the number of individual eddies used in each composite (see Figure 4.3).

Using the same quartile periods as for chlorophyll anomalies, composites of the quarterly averaged eddy-Ekman pumping within eddies are constructed (Figure 4.7a). The magnitude of the eddy-Ekman pumping ranges between 1-4 cm day^{-1} for both cyclones and anticyclones, and is consistent with expectations for surface current-induced pumping. The averaged eddy-Ekman pumping is typically stronger in the western region as compared to the eastern region, particularly during the austral summer months. This weaker observed eddy-Ekman pumping in the eastern region could be caused by weaker eddy currents, as the eastern STCC typically has lower average eddy energy (Qiu et al. 2008; Travis and Qiu 2017). This can also be seen in the average axial speed of the eddies (Table 4.1). There is no distinct seasonality to the pumping (Figure 4.7b), as well as no seasonal reversal which by itself could cause the observed seasonal reversal of the character of the chlorophyll anomalies within eddies. However, it can be conjectured that the downwelling(upwelling) in cyclones(anticyclones) generated by the eddy-Ekman pumping can be an important contributor to the nutrient supply in the eddies, and can complement the effect of the mixed layer depth anomalies. Indeed, an estimate of the relative importance can be made using a mixed layer nitrate flux budget equation.

$$\frac{\partial N}{\partial t} = -\frac{1}{H_{MLD}}\Big(\overline{N}_{MLD} - N_B\Big)\Big(\frac{\partial H_{MLD}}{\partial t} + w_{Ek}\Big) \tag{4.7}$$

In this equation, ∂N/∂t = the change of nitrate in the mixed layer, H_{MLD} = the mixed layer depth, $\overline{N}_{MLD}$ = the average nitrate concentration in the mixed layer, N_B = the nitrate concentration 2 m below the base of the mixed layer, $\partial H_{MLD}/\partial$t = the change in mixed layer depth, and w_{Ek} = the eddy-Ekman pumping velocity. From this equation, we provide an estimation of the magnitude of $\partial H_{MLD}/\partial$t to w_{Ek} to assess their relative importance. In Figure 4.8, we can see that the mixed layer deepens at a maximum rate of roughly 30-50 cm day^{-1}. When compared to the average Ekman pumping magnitude of 1-4 cm day^{-1}, the entrainment of deeper nutrients from a deepening mixed layer overwhelms the Ekman pumping for most of the year.

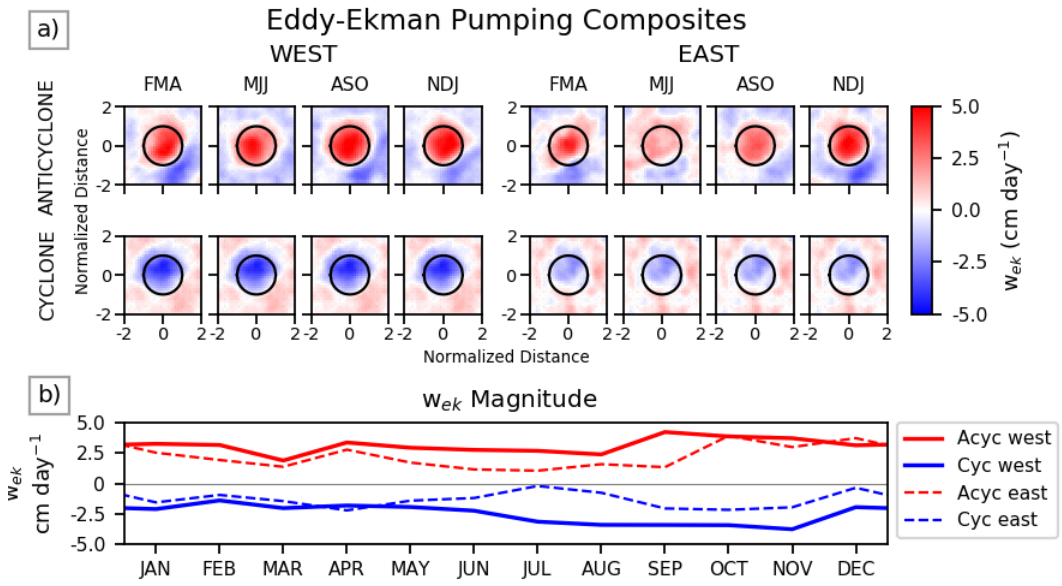

Figure 4.7: a) Ekman pumping anomalies within eddies in the South Pacific STCC. Wind stress data are taken from QuikSCAT data covering the time range from January 2000 to December 2008. Composites by quarterly period are taken to match that of the chlorophyll anomalies. The left(right) side shows the composites for the western(eastern) STCC, while anticyclones(cyclones) are shown in the top(bottom) row of composites. The black circle indicates one eddy radius from the center. The colorbar indicated the strength of the eddy-Ekman pumping in cm day^{-1}. b) The monthly time series shows the magnitude of the eddy-Ekman pumping. Cyclones(anticyclones) are indicated by the blue(red) lines, while the western(eastern) composites are indicated by the solid(dotted) lines.

Subsurface information relevant to the eddies in the region and the availability of light and nutrients necessary to stimulate primary production are shown in Figure 4.8. Throughout the STCC, the mixed layer depth of cyclones is shallower than anticyclones, with maximum mixed layer depths (MLDs) occurring in July. In the western STCC, anticyclones reach a maximum depth of approximately 80 m, while cyclones have a maximum depth around 60 m. In the eastern STCC, anticyclones reach a maximum depth of 95 m and cyclones reach a maximum depth of 70 m. Between the western and eastern portions of the STCC, there are significant differences in the euphotic layer depth (z_{eu}) and in the nitracline depth. The average western euphotic layer depth is approximately 100 m, while the eastern

euphotic layer depth is approximately 130 m. Lastly, the western nitracline changes from approximately 100 m in the summer to 125 m in the winter, while the eastern nitracline remains relatively constant at approximately 150 m. Note that while the choice of nitracline definition determines the observed depth, the pattern remains even with a different choice of nitracline definition. For example, at a lower definition of nitracline of 0.2 μmol kg^{-1} instead of 1 μmol kg^{-1}, the eastern nitracline is approximately 50-75 m deeper than the western nitracline. The averaged mixed layer nitrate concentration is shown in Figures 4.8c and 4.8d, while mixed layer nitrate concentration anomalies located within eddies as a percentage of the background mixed layer nitrate concentrations are shown in Figures 4.8e and 4.8f. It should be noted that there are some unexpected fluctuations in the eastern STCC average mixed layer nitrate concentration, with a nitrate peak occurring during the summer months. This unexpected fluctuations peaks around 0.25 μmol kg^{-1}, which is a relatively low concentration compared to our nitracline definition, but highlights the need for direct seasonal measurements. Current mixed layer nitrate concentrations are inferred from observed mixed layer depths with climatological nitrate levels, but more direct observations would help to quantify observed nitrate levels and nitrate fluxes. It can be seen that the deeper mixed layers of the anticyclones in the western STCC lead to a largest monthly nitrate anomaly across the entire STCC region, in both cyclones and anticyclones, with peak nitrate anomalies in cyclones(anticyclones) of approximately -5%(10%) during the austral spring. In the eastern STCC, the low nitrate levels mean that there is minimal nitrate concentration anomalies throughout the year, with concentration anomaly magnitudes of 1-2%. The combination of changing light and nutrient availability are the most likely drivers of the changing near-surface chlorophyll response to eddies observed (Figure 4.2).

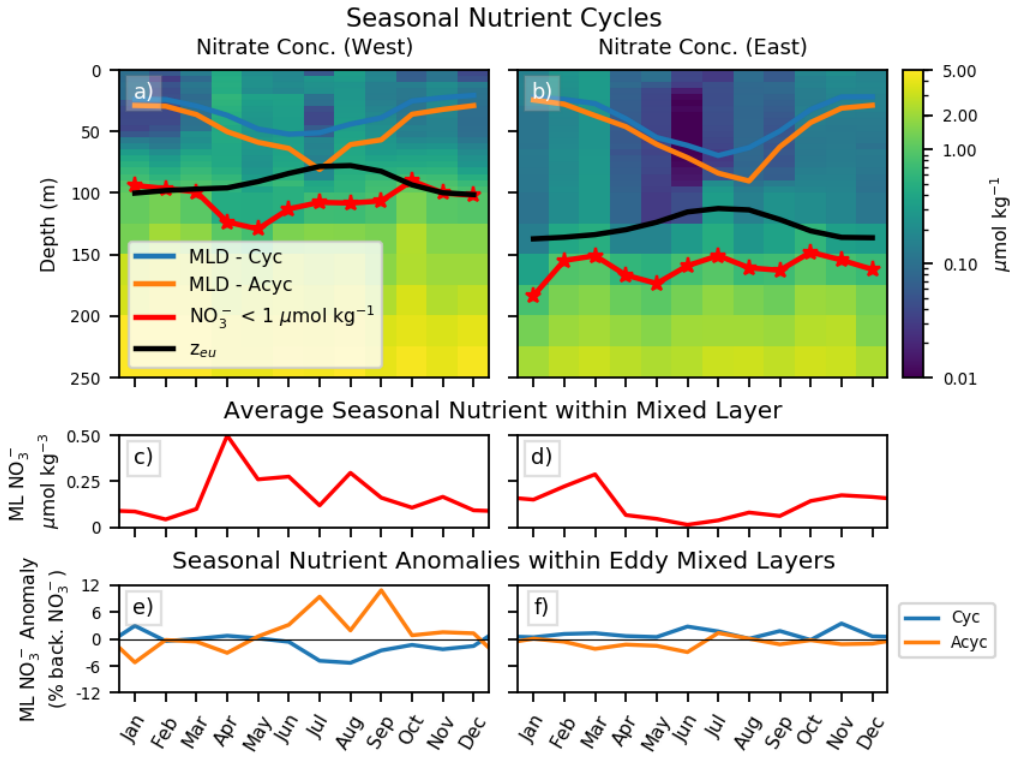

Figure 4.8: Figures a) and c) correspond to the western STCC (165°E - 170°W, 22°S-28°S), while b) and d) correspond to the eastern STCC (160°W-130°W, 22°S-28°S). Nitrate levels (NO_3^-) in the STCC region are divided into a) western STCC and b) eastern STCC, and averaged by month. The colorbar indicates nitrate concentrations throughout the water column, given as μmol kg^{-1}, and as taken from World Ocean Atlas 2018 climatologies (WOA18). The mixed layer depth for anticyclonic and cyclonic eddies are given as the orange and blue lines, respectively. The nitracline, defined as where NO_3^- exceeds 1 μmol kg^{-1} is shown by the red line. The euphotic layer depth (z_{eu}) is shown by the black line. A monthly time series of nitrate concentration calculated within the mixed layer (c and d) and nitrate concentration anomalies within eddies (e and f) is shown
. Nutrient anomalies are calculated as the percent difference of nitrate concentrations in the mixed layers within eddies from the nitrate concentrations in the mixed layers outside of eddies.

Figure 4.9 illustrates the comparative changes in background chl$_a$ on a seasonal cycle (Figures 4.9a, 4.9b), the relative changes of anomalous chl$_a$ on a seasonal cycle (Figures 4.9c, 4.9d), and changes in the photosynthetically available radiation within the mixed layer (PAR_{ML}) (Figures 4.9e, 4.9f). The parameters for the western STCC are shown in the left

column (Figures 4.9a, 4.9c, 4.9e), while the eastern STCC is shown in the right column (Figures 4.9b, 4.9d, 4.9f).

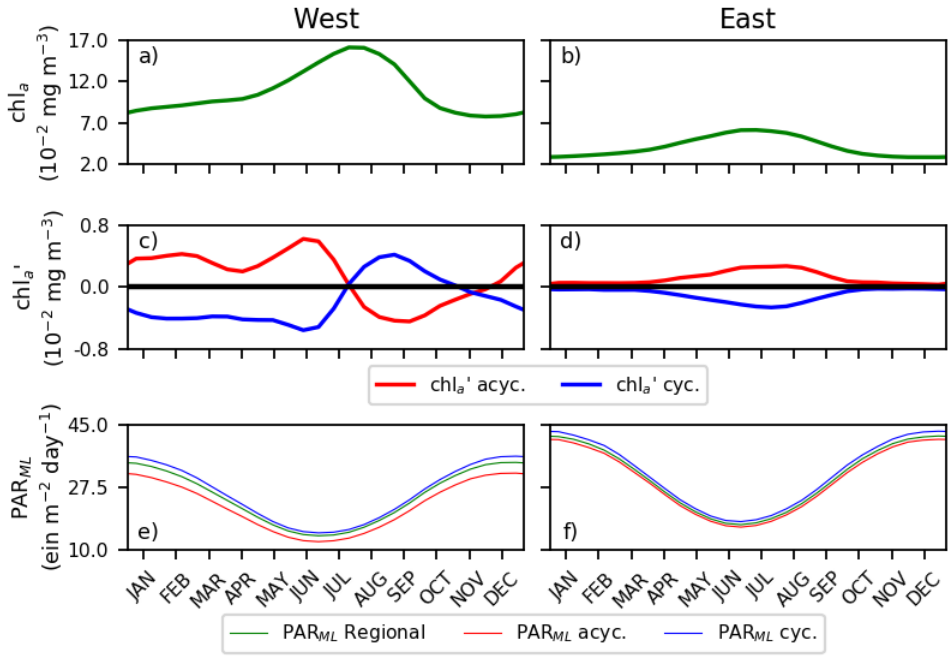

Figure 4.9: Figures a), c), and e) correspond to the western STCC (165°E - 170°W, 22°S-28°S), while b), d), and f) correspond to the eastern STCC (160°W-130°W, 22°S-28°S). a) and b): Seasonal cycle of the averaged cycle of near-surface chlorophyll (chl$_a$). c) and d): The chl$_a$ anomalies in cyclones and anticyclones. e) and f): Photosynthetically available radiation within the mixed layer (PAR$_{ML}$). The regionally averaged PAR$_{ML}$ is given by the green line, while the PAR$_{ML}$ within cyclones(anticyclones) is given by the blue(red) lines, respectively.

For the western STCC, the background chlorophyll concentration ($\overline{\text{chl}_a}$) ranges from 0.078 mg m^{-3} in December to 0.163 mg m^{-3} in August, amounting to a 109% increase from the seasonal minimum to the seasonal maximum. PAR$_{ML}$ in the region ranges from 13.8 to 34.5 ein m^{-2} day^{-1}. For the eastern STCC, $\overline{\text{chl}_a}$ ranges from 0.029 mg m^{-3} in December to 0.062 mg m^{-3}, creating a 114% increase. PAR$_{ML}$ in the eastern STCC ranges from 17.0 to 42.0 ein m^{-2} day^{-1}. In both the western and eastern STCC, the seasonal changes in $\overline{\text{chl}_a}$ are inversely correlated with PAR$_{ML}$ (western correlation = -0.77, eastern correlation = -0.93).

4.4 Discussion

The spatially and temporally complicated near-surface chlorophyll signal in the presence of mesoscale eddies in the South Pacific Subtropical Counter-Current highlights the difficulty in characterizing an expected physical-biological response. Within any region, there can be significant variability throughout the year in the characterization of the environment in which eddies are found. As seen in the South Pacific STCC, even moving across a region in which eddy activity is largely the result of a single driver, namely baroclinic instabilities (Travis and Qiu 2017), there can be a shift in the character of the response to the same eddies. Globally, this creates the possibility that there are areas in which this seasonally-reversing biological response have been overlooked.

To identify regions which could exhibit a seasonal reversal of the type of chlorophyll response to the presence of eddies, a $<\text{chl}_a>$-ssh anomaly correlation is calculated for each month (σ(month)). From these correlations, the maximum and minimum correlation among each of the 12 months found at a grid point are multiplied together.

$$\sigma_{max,min} = max\big(\sigma(\text{month})\big) * min\big(\sigma(\text{month})\big) \tag{4.8}$$

This combined correlation will always be positive if the maximum and minimum correlations among the months are the same sign (i.e., always a positive or always a negative correlation). The combined correlation will only be negative if the maximum and minimum correlations among the months are of opposite sign. In this case, SSH and chl_a anomalies are positively correlated for part of the year and negatively correlated for part of the year. In Figure 4.10, $\sigma_{max*min}$ is binned into 3-degree x 3-degree grids.

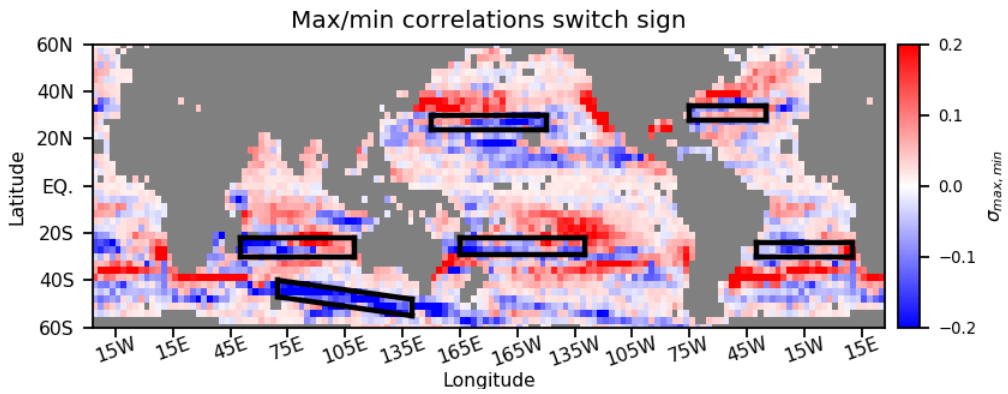

Figure 4.10: The multiplied max-min correlations by month ($\sigma_{max,min}$) are gridded into 3deg x 3 deg boxes. The colorbar is the multiplied correlation coefficent ($\sigma_{max,min} = \sigma_{max} * \sigma_{min}$), where σ is the correlation coefficient for any given month. Regions with a seasonally consistent <chl$_a$>-ssh anomaly correlation are shown in red. Regions with a seasonal switch of the sign of the correlation (positive and negative correlations throughout the year) are shown in blue, and are areas of a possible reversal of the sign of the chlorophyll anomaly response to eddies. Possible regions of interest are highlighted by the black boxes.

A number of regions with negative combined correlations are identified, as seen in Figure 4.10, and are indicative of seasonal reversal of the chlorophyll response to eddies. Some of the identified regions are the South Pacific STCC, the South Indian STCC, the ACC, the North Pacific STCC, the North Atlantic STCC, and the South Atlantic STCC, and are highlighted by the black boxes in Figure 4.10. A common feature among these currents, with the exception of the ACC, is that they lie near the boundary between typically highly oligotrophic regions and relatively more productive waters. Recent work in the ACC (Song et al. 2018; Dawson et al. 2018) also observed a seasonal variation in the type of chlorophyll anomaly response to eddies, emphasizing the importance of changing mixed layer depths and nutrient availability in determining the expected physical-biological response to eddies.

Seasonal cycles of chlorophyll anomalies within mesoscale eddies for a number of the above listed regions are shown in Figure 4.11. From the figure, it can be seen that magnitude of the anomalies and the timing and duration of the seasonal reversal is highly variable among the regions. This is indicative of the large number of factors that could be affecting the physical-biological responses, and driving the seasonal reversal. For instance, we see the seasonal

reversal of the anomalous chlorophyll signal in the winter/spring in the South Pacific STCC (Figure 4.2), whereas in the South Indian STCC (Figure 4.11a, 4.11b), the reversal occurs during the summer. In the South Indian STCC, it has been observed that an anomalous summer bloom to the east of Madagascar is associated with a change in phytoplankton community structure, moving to nitrogen-fixing phytoplankton (Poulton et al. 2009), and it has been explored as to whether the bloom is fertilized by iron from Madagascar (Srokosz et al. 2015). It is unknown how this shift in community structure would manifest within the eddying flows, and warrants further investigation. This region is also demonstrative of the need to look more deeply into each of the regions highlighted in Figures 4.10 and 4.11.

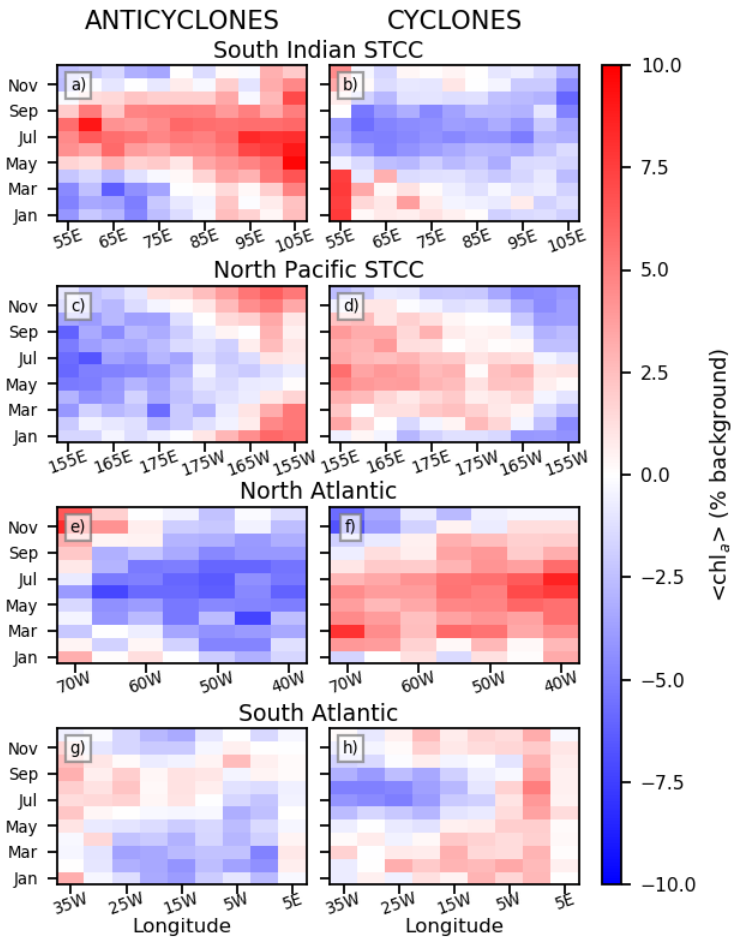

Figure 4.11: Hovmueller x-t diagrams of normalized chlorophyll anomalies (<chl$_a$>) by month for the regions highlighted in Figure 4.10 by the black boxes. Hovmueller diagrams for the South Pacific STCC can be found in Figure 4.2, while the ACC diagrams are not included. The left column shows the anomalies for anticyclones and the right column shows the anomalies for cyclones. The colorbar is the normalized chlorophyll anomaly, given as a percent of the large scale, background chlorophyll signal. a) and b): South Indian STCC (50°E - 110°E, 22°S-30°S). c) and d): North Pacific STCC (150°E - 150°W, 24°N-30°S). e) and f): North Atlantic STCC (75°W - 35°W, 28°N - 34°N). g) and h): South Atlantic STCC (40°W - 10°E, 24°S - 30°S).

4.5 Summary

By isolating near-surface chlorophyll at the mesoscale length scales, the physical-biological effect of eddies can be seen from satellite data. In the South Pacific STCC, this signal is found to be highly spatially and temporally complicated. In the east, chl_a' in mesoscale eddies exhibit a response consistent with a nutrient-limited regime throughout the year. In the west, the chlorophyll signal indicates a seasonally inconsistent response, with alternating positive/negative anomalies with the changing seasons. Cyclones (anticyclones) exhibit a negative (positive) response signal during the summer months and a positive(negative) signal during the winter months. This pattern is consistent with a nutrient-limited regime during the summer months and a light-limited regime during the winter months.

Examining seasonal trends in climatological nutrient availability across the STCC gives evidence to support these observed patterns. In the eastern STCC, the deep nitracline exceeds 150 meters throughout the whole year, with the euphotic zone extending down to 120-130 meters throughout the year. As the seasonally-varying mixed layer ranges from roughly 30 meters for all eddies in the summer to 100 meters for anticyclones and 80 meters for cyclones, it is observed that the mixed layer depth is consistently shallower than the euphotic zone and the nitracline. In this area, the chlorophyll anomaly patterns are consistent with the expected response for a region where nutrient availability within the mixed layer is the limiting factor.

A very different pattern emerges in the western STCC. The nitracline is shallower, with typical depths between 90-120 meters and a maximum(minimum) during the winter(summer). This is also approximately the range of the euphotic zone, which has a maximum during the summer and a minimum during the winter. During the summer months, the mixed layer depth is at a minimum, and typically 20-40 meters deep. During this time, there is low nitrate concentration within the mixed layer for both eddy types. In the winter, the deeper mixed layers are able to reach down below the euphotic zone and access the deeper nutrient pool. In this case, higher nutrient availability and deeper mixing below the euphotic zone provide the conditions to shift the character of the environment to one consistent with

a light-limited regime for chlorophyll anomalies. This is also supported by the lower overall PAR_{ML} found throughout the western STCC as compared to the eastern STCC, as well as lower PAR_{ML} within anticyclones as compared to cyclones.

Taking into account all of these patterns, the changing near-surface chlorophyll response in the presence of eddies in the western STCC can be explained. If the character of the environment of the western STCC were the same as that of the eastern STCC, we would expect to see chlorophyll anomaly patterns consistent with nutrient limitation in the mixed layer, i.e., positive anomalies in anticyclones and negative anomalies in cyclones. Light-limitation would produce a reversed pattern, i.e., negative anomalies in anticyclones and positive anomalies in cyclones. The deeper mixed layers of anticyclones would decrease average light levels, leading to decreased productivity, and subsequently, lower chlorophyll levels, while the opposite would happen in cyclones. In the western STCC, the observed chlorophyll anomaly patterns in the region are consistent with nutrient-limitation throughout the summer, when shallow mixed layers keep the deep nutrient supply isolated from the surface. During the winter, however, the mixed layer deepens, increasing the nitrate concentrations throughout the mixed layer. The mixed layer deepens beneath the euphotic layer, and it is inferred that the regime switches to being light-limited. This switch from a nutrient-limited regime to a light-limited regime causes the reversal in the anomalous chlorophyll response found within eddies in the region. This is contrasted with the eastern STCC, where the region is inferred to be nutrient-limited throughout the whole year. The nitracline in the eastern STCC is about 25-50 meters deeper than the western STCC, and remains isolated from the surface for the whole year. Because the region remains in a nutrient-limited regime, the character of the anomalous response is consistent throughout the year.

There are a number of effects and mechanisms that have not been accounted for in this work, such as the changes in the deep chlorophyll maximum which may not be observable by satellites (McGillicuddy et al. 2007), submesoscale dynamics (Zhang et al. 2019), and predation mechanisms, to name a few. For instance, top-down dynamics, such as predator grazing,

would not be distinguishable in the chlorophyll anomaly signals, and would complicate efforts to assess the potential for new production. Despite these limitations, this work highlights the need for taking into account all dynamics, including regionally and seasonally changing dynamics, when characterizing the physical-biological response to the presence of mesoscale eddies. Observational studies utilizing subsurface data, including data for Bio-Argo floats, such as those done by Dufois et al. (2017) and by Mignot et al. (2014), will be increasingly important in characterizing the dynamics within eddies in a region. The characterization of the mesoscale physical-biological response will require a careful understanding of the state of the ocean and all of the limiting factors involved, and increasing observational capabilities will improve our understanding of these factors and the dynamical processes which effect them.

CHAPTER 5
CONCLUSIONS

5.1 Summary

Mesoscale eddy activity within the South Pacific Subtropical Counter-current has been examined on decadal timescales, and seasonal patterns of the near-surface signatures of a chlorophyll response to the presence of these eddies has been identified. Eddy variability was investigated through the use of satellite altimetry data, while subsurface characteristics were described by using a combination of observational data from Argo buoys and ocean reanalysis (ECMWF ORAS4 and ORAS5) and ocean state products (ECCO2). Investigation into the near-surface chlorophyll response used the Glob-Colour merged satellite data product to optimize temporal and spatial coverage.

Decadal variability has been shown to be connected to low-frequency ($< 1\ \mathrm{yr}^{-1}$) changes in the strength of the baroclinic growth rate in the region. By idealizing the region using a 2-1/2 layer model, changes in the strength of the baroclinic growth rate can be understood through changes in the vertical shear and stratification in the system. A Taylor series expansion about the mean state allows for a quantification of the relative influence of the two terms, with approximately 66% of the baroclinic growth rate variability being caused by shear changes and 34% of the variability being caused by stratification changes. Additional decomposition was made to find the contributions of the changing temperature and salinity fields to the changes in shear and stratification. For both shear and stratification, the salinity-induced variability has peak magnitudes of roughly 50-75% that of the temperature-induced variability.

The decadal variability of the baroclinic growth rate, and subsequently, the eddy activity, can be further explored by understanding the dynamical processes leading to the observed changes. This is done through the use of the ECCO2 ocean state model, which is dynamically and thermodynamically consistent, allowing for temperature and salinity budgets to be

created. In this set-up, changes in net surface heat flux, net surface moisture flux, and advective flux convergence are calculated to identify the contributions of each of these forcing terms to total variability in the baroclinic growth rate. From this analysis, it was found that advective flux convergence is the most significant contributor to total variability, with advective flux convergence of salinity gradients being slightly more impactful than that of temperature gradients. The contribution of net surface heat and moisture flux to variability in the baroclinic growth rate are roughly equal, with moisture flux having a higher correlation. Total salinity-induced variability, through salinity-induced changes to shear and stratification, is found to be much more correlated with baroclinic growth rate changes (correlation = 0.828) than that due to temperature-induced variability. It is noted that baroclinic growth rate variations caused by salinity-induced shear and salinity-induced stratification changes are more broad, general patterns, and tend to work constructively. Conversely, those caused by temperature changes are much more localized, and can alternatively enhance or counteract each other, depending on time and location.

The variability in the surface forcings is found to be strongly correlated to the Interdecadal Pacific Oscillation (IPO). An EOF analysis on the region surrounding the STCC band reveals that the first mode of variability, which contains the largest amount of variance, is highly correlated with the IPO for net heat flux, net moisture flux, and wind stress curl. The manifestation of the IPO signal in the region can be understood through the movement of the South Pacific Convergence Zone, which previous studies have shown moves north or south during positive or negative IPO periods (Folland 2002; Kidwell et al. 2016). During a negative IPO period, the South Pacific Convergence Zone moves south and takes on a more diagonal, northwest-southeast tilt. In this orientation, the SPCZ crosses through the STCC band study region, and significantly alters patterns of heat flux and evaporation and precipitation, as well as altering wind patterns. When the spatial patterns of heat flux, moisture flux, and wind stress curl are examined for anomalies during a positive IPO versus a negative IPO period, it is found that they largely have the same patterns as wind convergence anomalies during the same comparison.

Lastly, it is found that the near-surface chlorophyll response to the presence of eddies in the region is seasonally and spatially highly variable. The eastern reach of the STCC band, which lies in the highly oligotrophic South Pacific Gyre, exhibits patterns with are consistent with the response expected from mixed layer depth anomaly induced changes for a nutrient-limited region. In this region, nutrient availability is very low, and the deeper mixed layers of anticyclones are able to mix nutrients at depth higher into the euphotic zone, leading to enhanced production, with the opposite occurring in cyclones. This pattern occurs throughout the entire year in the eastern STCC. In the western STCC, nutrient levels are still low, but the nitracline is shallower than in the eastern STCC. In this region, the chlorophyll anomalies are consistent with mixed layer anomalies in a nutrient-limited regime during the summer, just as in the eastern STCC. However, the patterns reverse during the winter. Anticyclones are found to have negative chlorophyll anomalies during the winter, which would be consistent with the expected response from mixed layer depth anomalies in a light-limited regime. In this pattern, deeper mixed layers in anticyclones can mix phytoplankton below the euphotic layer, leading to lower averaged light availability for photosynthesis for individual phytoplankton, decreasing productivity. These patterns are consistent with estimated nutrient concentrations and light availability within the mixed layer within eddies, as estimated from Argo buoy derived mixed layer depths, climatological nutrient levels, and satellite color derived light availability. Additionally, a metric is developed to find additional regions globally in which this observed reversal pattern could occur. There are a number of regions found across all ocean basins, indicating that areas of eddy-induced chlorophyll variability could be an overlooked phenomenon.

5.2 Future Directions

This work has provided the basis and context for an important circulation feature in the western South Pacific. Studies of low-frequency changes in the eddy activity and the related forcings on the state of the ocean which lead to the observed variability are important towards understanding eddies role in total ocean circulation in the region. This context can inform

studies which would explore related impacts of the eddies themselves on setting the ocean state.

For instance, it would be of interest to understand what impacts the eddy patterns themselves play in setting the circulation patterns which are observed. Qiu et al. (2015) found that sea surface height variability can itself be driven by eddy fluxes, and such effects have not yet been investigated in this region. The additional eddy-induced mass transport (Zhang et al. 2014) could itself help to modulate the ocean state patterns observed, and future understanding would benefit from quantifying this mechanism. Similarly, an investigation into eddy-mean flow interactions and the related energy cascades between different length scales could inform the energy pathways which set total circulation.

Additional investigations of eddy activity in the South Pacific Subtropical Countercurrent would benefit from an understanding of how the significant topographic features, such as the Kermadec Ridge, would influence large-scale circulation patterns and the eddies themselves. It is noted that the regions of the most intense eddy activity as observed from satellite altimetry lie just to the east of some of the more significant ridges in the area. It is very likely that topographically-induced forcings, such as steering of ocean currents or topographically-trapped Rossby wave propagation (Lou et al. 2019) can have significant impacts on eddy variability. Such a study could combine observational data, such as satellite altimetry and Argo float profiles, to investigate differences in eddy characterstics in the vicinity of the topographic features and further afield. A modeling study would complement such an investigation, providing the capability to explore fully three-dimensional evolution of flow characteristics. These studies would focus on local generation and dissipation mechanisms, as well as the evolution of eddies as they propagate closer to these features.

The observation of a seasonally-reversing near-surface chlorophyll response is an important first step towards the characterization of eddies role in the ecosystem of the western South Pacific. This observation highlights the need to account for multiple controlling mechanisms which can impact phytoplankton, which can form the base trophic level in ecosystem analysis. Additionally, unlike the low-frequency studies in eddy activity (Chapters

2 and 3), which use the assumption of low-frequency baroclinic instability strength variability to describe changes in eddy activity, this seasonally-reversing mechanism would complicate any interannual studies of near-surface chlorophyll in eddies. This study (Chapter 4) can provide the basis for constructing future studies, which can focus on low-frequency signals in each of the controlling mechanisms, and relate them back to observations.

The impacts of the eddies on biomass in the region would benefit greatly from increased sub-surface measurements. Studies by others, such as Dufois et al. (2017), are able to take great benefit from the additional information gained from Bio-Argo floats which are able to take sub-surface measurements of nutrients, as well as optical parameters which can be used to estimate phytoplankton abundance. Additionally, a biogeochemical modeling study of the region could explore the sensitivity of these results to different driving forces. Studies such as these would be crucial to expanding our understanding of the biological-physical mechanisms at play in eddies across all regions. These biological-physical studies can also have important consequences for higher-level ecosystem studies, in which eddies have been shown to be important habitats for higher trophic levels (Lavelle and Mohn 2010; Morato et al. 2009; Godø et al. 2012). As we are better able to characterize the physical environments which phytoplankton reside, studies of these higher trophic levels in the region can be better informed.

The wide range of complexity across the STCC band provide for a rich region of study of many different mechanisms. Eddy variability has been shown to be impacted by long-term changes in the temperature and salinity fields of the ocean, and the forcings of these parameters is strongly connected to shifts in IPO and large atmospheric patterns, such as the South Pacific Convergence Zone. The region also has very interesting patterns of biological-physical interactions, which could have significant impact on ecological patterns in the region. Because of all of this, eddy variability in the STCC provides ample opportunity for the study of many different phenomenon, and can be a source of many scientific gains in the future.

APPENDIX A

Following Pedlosky and Polvani (1987), the linearized equations for potential vorticity perturbations, q_n, are given as:

$$\Big(\frac{\delta}{\delta t} + U_n\frac{\delta}{\delta x}\Big)q_n + \frac{\delta\Pi_n}{\delta y}\frac{\delta\psi_n}{\delta x} = 0 \tag{A.1}$$

where ψ_n = the perturbation streamfunction, U_n = the zonal mean velocity, and Π_n = the mean potential vorticity, for each layer n (n = 1,2 for a $2^1/_2$ layer system). For a meridionally constant mean zonal flow, U_n, the following relationships are defined:

$$q_n = \nabla^2\psi_n + (-1)^n\Big(\frac{g'_nH_n}{f_0^2}\Big)\Big(\psi_1 - \psi_2 - \frac{\rho_n - \rho_1}{\rho_3 - \rho_2}\psi_2\Big) \tag{A.2}$$

$$\frac{\delta\Pi_n}{\delta y} = \beta - (-1)^n\Big(\frac{g'_nH_n}{f_0^2}\Big)\Big(U_1 - U_2 - \frac{\rho_n - \rho_1}{\rho_3 - \rho_2}U_2\Big) \tag{A.3}$$

In these equations, $g' = \frac{\rho_2-\rho_1}{\rho_0}g$, the reduced gravity for the system, ∇^2 = the horizontal Laplacian operator, ρ_n = the density of layer n, f_0 = the Coriolis parameter at a reference latitude, β = the meridional gradient of the Coriolis parameter at the same reference latitude.

By seeking normal mode solutions, $\psi_n = Re[\hat{\psi}_n exp[i(kx + ly - \omega t)]$, instabilities can be found when the wave frequency is complex. In this case, the real component of the wave frequency would be the wave propagation frequency, and the imaginary component would be the instability growth rate.

References

Adcock, Susan T. and Marshall, David P. Interactions between Geostrophic Eddies and the Mean Circulation over Large-Scale Bottom Topography. *J. Phys. Oceanogr.*, 30(12):3223–3238, 2000. ISSN 0022-3670. doi: 10.1175/1520-0485(2000)030<3223:IBGEAT>2.0.CO;2.

Anderson, David L.T. and Killworth, Peter D. Spin-up of a stratified ocean, with topography. *Deep. Res.*, 24(8):709–732, 1977. ISSN 01466291. doi: 10.1016/0146-6291(77)90495-7.

Bailleul, Frédéric; Cotté, Cédric, and Guinet, Christophe. Mesoscale eddies as foraging area of a deep-diving predator, the southern elephant seal. *Mar. Ecol. Prog. Ser.*, 408:251–264, jun 2010. ISSN 0171-8630. doi: 10.3354/meps08560.

Balmaseda, Magdalena Alonso; Mogensen, Kristian, and Weaver, Anthony T. Evaluation of the ECMWF ocean reanalysis system ORAS4. *Q. J. R. Meteorol. Soc.*, 139(674):1132–1161, 2013. ISSN 00359009. doi: 10.1002/qj.2063.

Behrenfeld, Michael J.; Boss, Emmanuel; Siegel, David A., and Shea, Donald M. Carbon-based ocean productivity and phytoplankton physiology from space. *Global Biogeochem. Cycles*, 19(1):1–14, 2005. ISSN 08866236. doi: 10.1029/2004GB002299.

Bender, Michael L. and Jonsson, Bror. Is seasonal net community production in the South Pacific Subtropical Gyre anomalously low? *Geophys. Res. Lett.*, pages 1–7, 2016. ISSN 00948276. doi: 10.1002/2016GL070220.

Borlace, Simon; Santoso, Agus; Cai, Wenju, and Collins, Matt. Extreme swings of the South Pacific Convergence Zone and the different types of El Ni??o events. *Geophys. Res. Lett.*, 41(13):4695–4703, 2014. ISSN 19448007. doi: 10.1002/2014GL060551.

Bowen, Melissa M.; Wilkin, John L., and Emery, William J. Variability and forcing of the East Australian Current. *J. Geophys. Res. C Ocean.*, 110(3):1–10, 2005. ISSN 01480227. doi: 10.1029/2004JC002533.

Bowen, Melissa M.; Sutton, Philip J H, and Roemmich, Dean. Wind-driven and steric fluctuations of sea surface height in the southwest Pacific. *Geophys. Res. Lett.*, 33(14): 2–5, 2006. ISSN 00948276. doi: 10.1029/2006GL026160.

Cai, Wenju. Antarctic ozone depletion causes an intensification of the Southern Ocean super-gyre circulation. *Geophys. Res. Lett.*, 33(3):1–4, 2006. ISSN 00948276. doi: 10.1029/2005GL024911.

Campbell, Janet W. The lognormal distribution as a model for bio-optical variability in the sea. *J. Geophys. Res.*, 100(C7):13237, 1995. ISSN 0148-0227. doi: 10.1029/95JC00458.

Chaigneau, Alexis; Le Texier, Marie; Eldin, Gérard; Grados, Carmen, and Pizarro, Oscar. Vertical structure of mesoscale eddies in the eastern South Pacific Ocean: A composite analysis from altimetry and Argo profiling floats. *J. Geophys. Res. Ocean.*, 116(11):1–16, 2011. ISSN 21699291. doi: 10.1029/2011JC007134.

Chelton, Dudley B and Schlax, Michael G. Global Observations of Oceanic Rossby Waves. *Science (80-.).*, 272(5259):234–238, apr 1996. ISSN 0036-8075. doi: 10.1126/science.272.5259.234.

Chelton, Dudley B.; Gaube, Peter; Schlax, Michael G.; Early, Jeffrey J., and Samelson, Roger M. The influence of nonlinear mesoscale eddies on near-surface oceanic chlorophyll. *Science (80-.).*, 334(6054):328–332, 2011. ISSN 10959203. doi: 10.1126/science.1208897.

Chen, Ru; Flierl, Glenn R., and Wunsch, Carl. A description of local and nonlocal eddy-mean flow interaction in a global eddy-permitting state estimate. *J. Phys. Oceanogr.*, 44 (9):2336–2352, 2014. ISSN 15200485. doi: 10.1175/JPO-D-14-0009.1.

Condie, Scott and Condie, Ryan. Retention of plankton within ocean eddies. *Glob. Ecol. Biogeogr.*, 25(10):1264–1277, 2016. ISSN 14668238. doi: 10.1111/geb.12485.

Dawson, H. R. S.; Strutton, P. G., and Gaube, P. The Unusual Surface Chlorophyll Signatures of Southern Ocean Eddies. *J. Geophys. Res. Ocean.*, 123(9):6053–6069, sep 2018. ISSN 21699275. doi: 10.1029/2017JC013628.

De Szoeke R. A., . On the Wind-Driven Circulation of South PAcific Ocean. *J. Phys. Oceanogr.*, 17:613–630, 1987. ISSN 0022-3670. doi: 10.1175/1520-0485.

Dewar, William K. Baroclinic Eddy Interaction with Isolated Topography. *J. Phys. Oceanogr.*, 32(10):2789–2805, 2002. ISSN 0022-3670. doi: 10.1175/1520-0485(2002)032<2789:BEIWIT>2.0.CO;2.

Dong, Changming; McWilliams, James C; Liu, Yu, and Chen, Dake. Global heat and salt transports by eddy movement. *Nat. Commun.*, 5:3294, 2014. ISSN 2041-1723. doi: 10.1038/ncomms4294.

Ducet, N.; Le Traon, P. Y., and Reverdin, G. Global high-resolution mapping of ocean circulation from TOPEX/Poseidon and ERS-1 and -2. *J. Geophys. Res. Ocean.*, 105(C8): 19477–19498, 2000. ISSN 2169-9291. doi: 10.1029/2000jc900063.

Dufois, François; Hardman-Mountford, Nick J.; Greenwood, Jim; Richardson, Anthony J; Feng, Ming; Herbette, Steven, and Matear, Richard. Impact of eddies on surface chlorophyll in the South Indian Ocean. *J. Geophys. Res. Ocean.*, 119(11):8061–8077, nov 2014. ISSN 21699275. doi: 10.1002/2014JC010164.

Dufois, François; Hardman-mountford, Nick J; Greenwood, Jim; Richardson, Anthony J; Feng, Ming, and Matear, Richard J. Anticyclonic eddies are more productive than cyclonic eddies in subtropical gyres because of winter mixing. *Science (80-.).*, (May):1–7, 2016. doi: 10.1126/sciadv.1600282.

Dufois, François; Hardman-Mountford, Nick J.; Fernandes, Michelle; Wojtasiewicz, Bozena; Shenoy, Damodar; Slawinski, Dirk; Gauns, Mangesh; Greenwood, Jim, and Toresen, Reidar. Observational insights into chlorophyll distributions of subtropical South Indian Ocean eddies. *Geophys. Res. Lett.*, 44(7):3255–3264, 2017. ISSN 19448007. doi: 10.1002/2016GL072371.

Dufour, Carolina O.; Griffies, Stephen M.; de Souza, Gregory F.; Frenger, Ivy; Morrison, Adele K.; Palter, Jaime B.; Sarmiento, Jorge L.; Galbraith, Eric D.; Dunne, John P.;

Anderson, Whit G., and Slater, Richard D. Role of Mesoscale Eddies in Cross-Frontal Transport of Heat and Biogeochemical Tracers in the Southern Ocean. *J. Phys. Oceanogr.*, 45(12):3057–3081, dec 2015. ISSN 0022-3670. doi: 10.1175/JPO-D-14-0240.1.

Folland, C. K. Relative influences of the Interdecadal Pacific Oscillation and ENSO on the South Pacific Convergence Zone. *Geophys. Res. Lett.*, 29(13):2–5, 2002. ISSN 0094-8276. doi: 10.1029/2001GL014201.

Frenger, Ivy; Münnich, Matthias, and Gruber, Nicolas. Imprint of Southern Ocean mesoscale eddies on chlorophyll. *Biogeosciences*, 15(15):4781–4798, aug 2018. ISSN 1726-4189. doi: 10.5194/bg-15-4781-2018.

Fu, Lee Lueng. Pattern and velocity of propagation of the global ocean eddy variability. *J. Geophys. Res. Ocean.*, 114(11):1–14, 2009. ISSN 21699291. doi: 10.1029/2009JC005349.

Ganachaud, Alexandre; Cravatte, S.; Melet, A.; Schiller, A.; Holbrook, N. J.; Sloyan, B. M.; Widlansky, M. J.; Bowen, M.; Verron, J.; Wiles, P.; Ridgway, K.; Sutton, P.; Sprintall, J.; Steinberg, C.; Brassington, G.; Cai, W.; Davis, R.; Gasparin, F.; Gourdeau, L.; Hasegawa, T.; Kessler, W.; Maes, C.; Takahashi, K.; Richards, K. J., and Send, U. The Southwest Pacific Ocean circulation and climate experiment (SPICE). *J. Geophys. Res. Ocean.*, 119 (11):7660–7686, nov 2014. ISSN 21699275. doi: 10.1002/2013JC009678.

Garcia, H.E.; Weathers, K.W.; Paver, C.R.; Smolyar, I.; Boyer, T.P.; Locarnini, R.A.; Zweng, M.M.; Mishonov, A.V.; Baranova, O.K.; Seidov, D., and Reagan, J.R. World Ocean Atlas 2018. Vol. 4: Dissolved Inorganic Nutrients (phosphate, nitrate and nitrate+nitrite, silicate. *NOAA Atlas NESDIS 84*, 4:35 pp, 2019.

Gaube, P.; Chelton, D. B.; Strutton, P. G., and Behrenfeld, M. J. Satellite observations of chlorophyll, phytoplankton biomass, and Ekman pumping in nonlinear mesoscale eddies. *J. Geophys. Res. Ocean.*, 118(12):6349–6370, 2013. ISSN 21699291. doi: 10.1002/2013JC009027.

Gaube, Peter; McGillicuddy, Dennis J.; Chelton, Dudley B.; Behrenfeld, Michael J., and Strutton, Peter G. Regional variations in the influence of mesoscale eddies on near-surface chlorophyll. *J. Geophys. Res. Ocean.*, 119(12):8195–8220, dec 2014. ISSN 21699275. doi: 10.1002/2014JC010111.

Gaube, Peter; Chelton, Dudley B.; Samelson, Roger M.; Schlax, Michael G., and O'Neill, Larry W. Satellite Observations of Mesoscale Eddy-Induced Ekman Pumping. *J. Phys. Oceanogr.*, 45(1):104–132, 2015. ISSN 0022-3670. doi: 10.1175/JPO-D-14-0032.1.

Gaube, Peter; J. McGillicuddy, Dennis, and Moulin, Aurélie J. Mesoscale Eddies Modulate Mixed Layer Depth Globally. *Geophys. Res. Lett.*, 46(3):1505–1512, feb 2019. ISSN 00948276. doi: 10.1029/2018GL080006.

Godø, Olav R; Samuelsen, Annette; Macaulay, Gavin J; Patel, Ruben; Hjøllo, Solfrid Sætre; Kaartvedt, Stein, and Johannessen, Johnny A. Mesoscale Eddies Are Oases for Higher Trophic Marine Life. *PLoS One*, 7(1):1–9, 2012. doi: 10.1371/journal.pone.0030161.

Gouriou, Yves and Delcroix, Thierry. Seasonal and ENSO variations of sea surface salinity and temperature in the South Pacific Convergence Zone during 1976-2000. *J. Geophys. Res. Ocean.*, 107(C12):SRF 12–1–SRF 12–14, 2002. ISSN 01480227. doi: 10.1029/2001JC000830.

Greatbatch, R. J.; Zhai, X.; Claus, M.; Czeschel, L., and Rath, W. Transport driven by eddy momentum fluxes in the Gulf Stream Extension region. *Geophys. Res. Lett.*, 37(24): 1–6, 2010. ISSN 00948276. doi: 10.1029/2010GL045473.

Griffiths, G M; Salinger, M J, and Leleu, I. Trends in extreme daily rainfall across the South Pacific and relationship to the South Pacific Convergence Zone. *Int. J. Climatol.*, 23(8): 847–869, jun 2003. ISSN 0899-8418. doi: 10.1002/joc.923.

Guidi, Lionel; Calil, Paulo H R; Duhamel, Solange; Björkman, Karin M; Doney, Scott C; Jackson, George A; Li, Binglin; Church, Matthew J; Tozzi, Sasha; Kolber, Zbigniew S; Richards, Kelvin J; Fong, Allison A; Letelier, Ricardo M; Gorsky, Gabriel; Stemmann,

Lars, and Karl, David M. Does eddy-eddy interaction control surface phytoplankton distribution and carbon export in the North Pacific Subtropical Gyre? *J. Geophys. Res. Biogeosciences*, 117(G2):n/a–n/a, 2012. ISSN 01480227. doi: 10.1029/2012JG001984.

Haffke, Colene and Magnusdottir, Gudrun. The South Pacific Convergence Zone in three decades of satellite images. *J. Geophys. Res. Atmos.*, 118(19):10839–10849, 2013. ISSN 21698996. doi: 10.1002/jgrd.50838.

Hasson, Audrey; Delcroix, Thierry, and Boutin, Jacqueline. Formation and variability of the South Pacific Sea Surface Salinity maximum in recent decades. *J. Geophys. Res. Ocean.*, 118(10):5109–5116, 2013. ISSN 21699291. doi: 10.1002/jgrc.20367.

He, Qingyou; Zhan, Haigang; Cai, Shuqun, and Li, Zimu. Eddy effects on surface chlorophyll in the northern South China Sea: Mechanism investigation and temporal variability analysis. *Deep. Res. Part I Oceanogr. Res. Pap.*, 112:25–36, 2016a. ISSN 09670637. doi: 10.1016/j.dsr.2016.03.004.

He, Qingyou; Zhan, Haigang; Cai, Shuqun, and Zha, Guozhen. On the asymmetry of eddy-induced surface chlorophyll anomalies in the southeastern Pacific: The role of eddy-Ekman pumping. *Prog. Oceanogr.*, 141:202–211, 2016b. ISSN 00796611. doi: 10.1016/j.pocean.2015.12.012.

Henley, Benjamin J.; Gergis, Joelle; Karoly, David J.; Power, Scott; Kennedy, John, and Folland, Chris K. A Tripole Index for the Interdecadal Pacific Oscillation. *Clim. Dyn.*, 45 (11-12):3077–3090, 2015. ISSN 14320894. doi: 10.1007/s00382-015-2525-1.

Hill, K. L.; Rintoul, S. R.; Ridgway, K. R., and Oke, P. R. Decadal changes in the South Pacific western boundary current system revealed in observations and ocean state estimates. *J. Geophys. Res. Ocean.*, 116(1):1–12, 2011. ISSN 21699291. doi: 10.1029/2009JC005926.

Holte, James; Talley, Lynne D; Gilson, John, and Roemmich, Dean. An Argo mixed layer

climatology and database. *Geophys. Res. Lett.*, 44(11):5618–5626, 2017. ISSN 19448007. doi: 10.1002/2017GL073426.

Hosoda, Shigeki; Ohira, Tsuyoshi, and Nakamura, Tomoaki. A monthly mean dataset of global oceanic temperature. *JAMSTEC Rep. Res. Dev.*, 8(November):47–59, 2008.

Huang, Jie and Xu, Fanghua. Observational Evidence of Subsurface Chlorophyll Response to Mesoscale Eddies in the North Pacific. *Geophys. Res. Lett.*, 45(16):8462–8470, 2018. ISSN 19448007. doi: 10.1029/2018GL078408.

IPCC, . Climate Change 2013: The Physical Science Basis. Technical report, Cambridge University Press, 2013.

Kessler, William S. and Gourdeau, Lionel. Wind-driven zonal jets in the South Pacific Ocean. *Geophys. Res. Lett.*, 33(3):4–7, 2006. ISSN 00948276. doi: 10.1029/2005GL025084.

Kessler, William S. and Gourdeau, Lionel. The Annual Cycle of Circulation of the Southwest Subtropical Pacific, Analyzed in an Ocean GCM*. *J. Phys. Oceanogr.*, 37(6):1610–1627, 2007. ISSN 0022-3670. doi: 10.1175/JPO3046.1.

Kidwell, Autumn; Lee, Tong; Jo, Young-Heon, and Yan, Xiao-Hai. Characterization of the Variability of the South Pacific Convergence Zone Using Satellite and Reanalysis Wind Products. *J. Clim.*, 29(5):1717–1732, mar 2016. ISSN 0894-8755. doi: 10.1175/JCLI-D-15-0536.1.

Klein, Patrice and Lapeyre, Guillaume. The Oceanic Vertical Pump Induced by Mesoscale and Submesoscale Turbulence. *Ann. Rev. Mar. Sci.*, 1(1):351–375, 2009. ISSN 1941-1405. doi: 10.1146/annurev.marine.010908.163704.

Lavelle, J. William and Mohn, Christian. Motion, Commotion, and Biophysical Connections at Deep Ocean Seamounts. *Oceanography*, 23(01):90–103, 2010. ISSN 10428275. doi: 10.5670/oceanog.2010.64.

Lou, Jiale; Holbrook, Neil J., and O'Kane, Terence J. South Pacific decadal climate variability and potential predictability. *J. Clim.*, 32(18):6051–6069, 2019. ISSN 08948755. doi: 10.1175/JCLI-D-18-0249.1.

Luyten, J.; Pedlosky, J., and Stommel, H. Climatic inferences from the ventilated thermocline, 1983. ISSN 15731480.

Maritorena, Stéphane; Siegel, David A., and Peterson, Alan R. Optimization of a semianalytical ocean color model for global-scale applications. *Appl. Opt.*, 41(15):2705, 2002. ISSN 0003-6935. doi: 10.1364/AO.41.002705.

Marshall, John; Adcroft, Alistair; Hill, Chris; Perelman, Lev, and Heisey, Curt. A finite-volume, incompressible navier stokes model for, studies of the ocean on parallel computers. *J. Geophys. Res. C Ocean.*, 102(C3):5753–5766, 1997. ISSN 01480227. doi: 10.1029/96JC02775.

Martin, Adrian P and Richards, Kelvin J. Mechanisms for vertical nutrient transport within a North Atlantic mesoscale eddy. *Deep. Res. Part II Top. Stud. Oceanogr.*, 48(4-5):757–773, 2001. ISSN 09670645. doi: 10.1016/S0967-0645(00)00096-5.

Martinez, Elodie; Ganachaud, Alexandre; Lefevre, Jerome, and Maamaatuaiahutapu, Keitapu. Central south pacific thermocline water circulation from a high-resolution ocean model validated against satellite data: seasonal variability and el ni??o 1997-1998 influence. *J. Geophys. Res. Ocean.*, 114(5):1–16, 2009. ISSN 21699291. doi: 10.1029/2008JC004824.

McClain, Charles R; Signorini, Sergio R, and Christian, James R. Subtropical gyre variability observed by ocean-color satellites. *Deep Sea Res. Part II Top. Stud. Oceanogr.*, 51(1-3):281–301, Jan 2004. ISSN 09670645. doi: 10.1016/j.dsr2.2003.08.002.

McGillicuddy, D. J.; Anderson, L. A.; Bates, N. R.; Bibby, T.; Buesseler, K. O.; Carlson, C. A.; Davis, C. S.; Ewart, C.; Falkowski, P. G.; Goldthwait, S. A.; Hansell, D. A.; Jenkins, W. J.; Johnson, R.; Kosnyrev, V. K.; Ledwell, J. R.; Li, Q. P.; Siegel, D. A., and

Steinberg, D. K. Eddy/Wind Interactions Stimulate Extraordinary Mid-Ocean Plankton Blooms. *Science (80-.).*, 316(5827):1021–1026, may 2007. ISSN 0036-8075. doi: 10.1126/science.1136256.

McGillicuddy, Dennis J. Mechanisms of Physical-Biological-Biogeochemical Interaction at the Oceanic Mesoscale. *Ann. Rev. Mar. Sci.*, 8(1):125–159, Jan 2016. ISSN 1941-1405. doi: 10.1146/annurev-marine-010814-015606.

McGregor, Shayne; Timmermann, Axel; Schneider, Niklas; Stuecker, Malte F., and England, Matthew H. The effect of the south pacific convergence zone on the termination of el niño events and the meridional asymmetry of ENSO. *J. Clim.*, 25(16):5566–5586, 2012. ISSN 08948755. doi: 10.1175/JCLI-D-11-00332.1.

Melnichenko, Oleg; Amores, Angel; Maximenko, Nikolai; Hacker, Peter, and Potemra, James. Signature of mesoscale eddies in satellite sea surface salinity data. *J. Geophys. Res. Ocean.*, 122(2):1416–1424, feb 2017. ISSN 21699275. doi: 10.1002/2016JC012420.

Menemenlis, Dimitris; Campin, Jean-Michel; Heimbach, Patrick; Hill, Christopher N.; Lee, Tong; Nguyen, An T.; Schodlok, Michael P., and Zhang, Hong. ECCO2: High resolution global ocean and sea ice data synthesis. *Mercat. Ocean Q. Newsl.*, 31(October):13–21, 2008.

Merle, Jacques; Rotschi, Henri, and Voituriez, Bruno. Zonal Circulation in the Tropical Western South Pacific at 170E. *Bull. Japanese Soc. Fish. Oceanogr.*, 1969.

Mignot, Alexandre; Claustre, Hervé; Uitz, Julia; Poteau, Antoine; D'Ortenzio, Fabrizio, and Xing, Xiaogang. Understanding the seasonal dynamics of phytoplankton biomass and the deep chlorophyll maximum in oligotrophic environments: A Bio-Argo float investigation. *Global Biogeochem. Cycles*, 28(8):856–876, 2014. ISSN 19449224. doi: 10.1002/2013GB004781.

Montecinos, Aldo and Pizarro, Oscar. Interdecadal sea surface temperature-sea level pressure

coupled variability in the South Pacific Ocean. *J. Geophys. Res. C Ocean.*, 110(8):1–11, 2005. ISSN 01480227. doi: 10.1029/2004JC002743.

Morato, Telmo; Bulman, Cathy, and Pitcher, Tony J. Modelled effects of primary and secondary production enhancement by seamounts on local fish stocks. *Deep. Res. Part II Top. Stud. Oceanogr.*, 56(25):2713–2719, 2009. ISSN 09670645. doi: 10.1016/j.dsr2.2008.12.029.

Morel, A.; Claustre, H., and Gentili, B. The most oligotrophic subtropical zones of the global ocean: Similarities and differences in terms of chlorophyll and yellow substance. *Biogeosciences*, 7(10):3139–3151, 2010. ISSN 17264170. doi: 10.5194/bg-7-3139-2010.

Morel, André; Huot, Yannick; Gentili, Bernard; Werdell, P. Jeremy; Hooker, Stanford B., and Franz, Bryan A. Examining the consistency of products derived from various ocean color sensors in open ocean (Case 1) waters in the perspective of a multi-sensor approach. *Remote Sens. Environ.*, 111(1):69–88, 2007. ISSN 00344257. doi: 10.1016/j.rse.2007.03.012.

Morris, M; Roemmich, D, and Cornuelle, B. Observations of Variability in the South Pacific, 1996.

Pedlosky, Joseph and Polvani, Lorenzo M. Wave-wave interaction of unstable baroclinic waves, 1987. ISSN 0022-4928.

Poulton, Alex J.; Stinchcombe, Mark C., and Quartly, Graham D. High numbers of Trichodesmium and diazotrophic diatoms in the southwest Indian Ocean. *Geophys. Res. Lett.*, 36(15):1–4, 2009. ISSN 00948276. doi: 10.1029/2009GL039719.

Qiu, Bo. Seasonal eddy field modulation of the North Pacific Subtropical Countercurrent: TOPEX/Poseidon observations and theory. *J. Phys. Oceanogr.*, 29(10):2471–2486, 1999. ISSN 00223670. doi: 10.1175/1520-0485(1999)029<2471:SEFMOT>2.0.CO;2.

Qiu, Bo and Chen, Shuiming. Seasonal Modulations in the Eddy Field of the South Pacific Ocean. *J. Phys. Oceanogr.*, 34:1515–1527, 2004. ISSN 0022-3670. doi: 10.1175/1520-0485(2004)034<1515:SMITEF>2.0.CO;2.

Qiu, Bo and Chen, Shuiming. Eddy-Induced Heat Transport in the Subtropical North Pacific from Argo, TMI, and Altimetry Measurements. *J. Phys. Oceanogr.*, 35(4):458–473, 2005. ISSN 0022-3670. doi: 10.1175/JPO2696.1.

Qiu, Bo and Chen, Shuiming. Decadal Variability in the Large-Scale Sea Surface Height Field of the South Pacific Ocean: Observations and Causes. *J. Phys. Oceanogr.*, 36:1751–1762, 2006. ISSN 0022-3670. doi: 10.1175/JPO2943.1.

Qiu, Bo; Scott, Robert B, and Chen, Shuiming. Length Scales of Eddy Generation and Nonlinear Evolution of the Seasonally Modulated South Pacific Subtropical Countercurrent. *J. Phys. Oceanogr.*, 38(7):1515–1528, jul 2008. ISSN 0022-3670. doi: 10.1175/2007JPO3856.1.

Qiu, Bo; Chen, Shuiming; Wu, Lixin, and Kida, Shinichiro. Wind-versus eddy-forced regional sea level trends and variability in the North Pacific ocean. *J. Clim.*, 28(4):1561–1577, 2015. ISSN 08948755. doi: 10.1175/JCLI-D-14-00479.1.

Qiu, Bo; Chen, Shuiming, and Schneider, Niklas. Dynamical links between the decadal variability of the Oyashio and Kuroshio Extensions. *J. Clim.*, 30(23):9591–9605, 2017. ISSN 08948755. doi: 10.1175/JCLI-D-17-0397.1.

Qu, Tangdong and Lindstrom, Eric J. A Climatological Interpretation of the Circulation in the Western South Pacific. *J. Phys. Oceanogr.*, 32(9):2492–2508, 2002. ISSN 0022-3670. doi: 10.1175/1520-0485-32.9.2492.

Reid, Joseph L. On the total geostrophic circulation of the South Pacific Ocean: Flow patterns, tracers and transports. *Prog. Oceanogr.*, 16(1):1–61, Jan 1986. ISSN 00796611. doi: 10.1016/0079-6611(86)90036-4.

Rieck, Jan K.; Böning, Claus W., and Greatbatch, Richard J. Decadal Variability of Eddy Kinetic Energy in the South Pacific Subtropical Countercurrent in an Ocean General Circulation Model. *J. Phys. Oceanogr.*, In press(4):757–771, apr 2018. ISSN 0022-3670. doi: 10.1175/JPO-D-17-0173.1.

Roemmich, D.; Gilson, J.; Davis, R.; Sutton, P.; Wijffels, S., and Riser, S. Decadal Spinup of the South Pacific Subtropical Gyre. *J. Phys. Oceanogr.*, 37(2):162–173, 2007. ISSN 0022-3670. doi: 10.1175/JPO3004.1.

Roemmich, Dean; Gilson, John; Sutton, Philip, and Zilberman, Nathalie. Multidecadal Change of the South Pacific Gyre Circulation. *J. Phys. Oceanogr.*, 46(6):1871–1883, jun 2016. ISSN 0022-3670. doi: 10.1175/JPO-D-15-0237.1.

Sasaki, Yoshi N.; Minobe, Shoshiro; Schneider, Niklas; Kagimoto, Takashi; Nonaka, Masami, and Sasaki, Hideharu. Decadal Sea Level Variability in the South Pacific in a Global Eddy-Resolving Ocean Model Hindcast. *J. Phys. Oceanogr.*, 38(8):1731–1747, 2008. ISSN 0022-3670. doi: 10.1175/2007JPO3915.1.

Schlax, Michael G and Chelton, Dudley B. The "Growing Method" of Eddy Identification and Tracking in Two and Three Dimensions. Technical report.

Schneider, Wolfgang; Fukasawa, Masao; Garcés-Vargas, José; Bravo, Luis; Uchida, Hiroshi; Kawano, Takeshi, and Fuenzalida, Rosalino. Spin-up of South Pacific subtropical gyre freshens and cools the upper layer of the eastern South Pacific Ocean. *Geophys. Res. Lett.*, 34(24):1–5, 2007. ISSN 00948276. doi: 10.1029/2007GL031933.

Shulzitski, Kathryn; Sponaugle, Su; Hauff, Martha; Walter, Kristen D., and Cowen, Robert K. Encounter with mesoscale eddies enhances survival to settlement in larval coral reef fishes. *Proc. Natl. Acad. Sci.*, 113(25):6928–6933, jun 2016. ISSN 0027-8424. doi: 10.1073/pnas.1601606113.

Song, Hajoon; Long, Matthew C; Gaube, Peter; Frenger, Ivy; Marshall, John, and McGillicuddy, Dennis J. Seasonal Variation in the Correlation Between Anomalies of

Sea Level and Chlorophyll in the Antarctic Circumpolar Current. *Geophys. Res. Lett.*, 45 (10):5011–5019, may 2018. ISSN 00948276. doi: 10.1029/2017GL076246.

Srokosz, M. A.; Robinson, J.; McGrain, H.; Popova, E. E., and Yool, A. Could the Madagascar bloom be fertilized by Madagascan iron? *J. Geophys. Res. Ocean.*, 120 (8):5790–5803, aug 2015. ISSN 21699275. doi: 10.1002/2015JC011075.

Travis, Seth and Qiu, Bo. Decadal Variability in the South Pacific Subtropical Countercurrent and Regional Mesoscale Eddy Activity. *J. Phys. Oceanogr.*, 47(3):499–512, mar 2017. ISSN 0022-3670. doi: 10.1175/JPO-D-16-0217.1.

Tsuchiya, Mizuki. On the Pacific upper-water circulation. *J. Mar. Res.*, 40:777–799, 1982.

Vincent, Dayton G. The South Pacific convergence zone (SPCZ): A review. *Mon. Weather Rev.*, 122:1949–1970, 1994. ISSN 0027-0644. doi: 10.1175/1520-0493(1994)122<1949:TSPCZA>2.0.CO;2.

Volkov, Denis L.; Lee, Sang Ki; Landerer, Felix W., and Lumpkin, Rick. Decade-long deep-ocean warming detected in the subtropical South Pacific. *Geophys. Res. Lett.*, 44(2): 927–936, 2017. ISSN 19448007. doi: 10.1002/2016GL071661.

von Storch, Hans and Zwiers, Francis W. *Statistical Analysis in Climate Research*. Cambridge University Press, Cambridge, 1999. ISBN 9780511612336. doi: 10.1017/CBO9780511612336.

Wang, L; Koblinsky, C; Howden, S, and BekleyB., . Large scale Rossby wave in the mid latitude South Pacific from altimetry data. *Geophys. Res. Lett.*, 25(2):179–182, 1998. doi: 10.1029/97GL03567.

Widlansky, Matthew J; Webster, Peter J, and Hoyos, Carlos D. On the location and orientation of the South Pacific Convergence Zone. *Clim. Dyn.*, 36(3-4):561–578, feb 2011. ISSN 0930-7575. doi: 10.1007/s00382-010-0871-6.

Wunsch, Carl; Heimbach, Patrick; Ponte, Rui M., and Fukumori, Ichiro. The global general circulation of the ocean estimated by the ECCO-Consortium. *Oceanography*, 22(SPL.ISS. 2):88–103, 2009. ISSN 10428275. doi: 10.5670/oceanog.2009.41.

Wyrtki, Klaus. Fluctuations of the Dynamic Topography in the Pacific Ocean, 1975. ISSN 0022-3670.

Yang, Yang; Liang, X. San; Qiu, Bo, and Chen, Shuiming. On the decadal variability of the eddy kinetic energy in the Kuroshio extension. *J. Phys. Oceanogr.*, 47(5):1169–1187, 2017. ISSN 15200485. doi: 10.1175/JPO-D-16-0201.1.

Zemskova, Varvara E.; White, Brian L., and Scotti, Alberto. Available Potential Energy and the General Circulation: Partitioning Wind, Buoyancy Forcing, and Diapycnal Mixing. *J. Phys. Oceanogr.*, 45(6):1510–1531, jun 2015. ISSN 0022-3670. doi: 10.1175/JPO-D-14-0043.1.

Zhang, Linlin and Qu, Tangdong. Low-frequency variability of South Pacific Tropical Water from Argo. *Geophys. Res. Lett.*, 41(7):2441–2446, 2014. ISSN 19448007. doi: 10.1002/2014GL059490.

Zhang, Linlin and Qu, Tangdong. Low frequency variability of the South Pacific Subtropical Gyre as seen from satellite altimetry and Argo. *J. Phys. Oceanogr.*, (January): 151001105438005, 2015. ISSN 0022-3670. doi: 10.1175/JPO-D-15-0026.1.

Zhang, Zhengguang; Wang, Wei, and Qiu, B. Bo. Oceanic mass transport by mesoscale eddies. *Science (80-.).*, 345(6194):322–324, 2014. ISSN 0036-8075. doi: 10.1126/science.1252418.

Zhang, Zhengguang; Qiu, Bo; Klein, Patrice, and Travis, Seth. The influence of geostrophic strain on oceanic ageostrophic motion and surface chlorophyll. *Nat. Commun.*, 10(2838): 1–11, 2019. ISSN 2041-1723. doi: 10.1038/s41467-019-10883-w.

Zilberman, N. V.; Roemmich, D. H., and Gille, S. T. Meridional volume transport in the South Pacific: Mean and SAM-related variability. *J. Geophys. Res. Ocean.*, 119(4):2658–2678, 2014. ISSN 21699291. doi: 10.1002/2013JC009688.

Zuo, H.; Balmaseda, M. A.; Tietsche, S.; Mogensen, K., and Mayer, M. The ecmwf operational ensemble reanalysis–analysis system for ocean and sea ice: a description of the system and assessment. *Ocean Science*, 15(3):779–808, 2019. doi: 10.5194/os-15-779-2019.